ISSN 2187-2260

Proceedings of the 18th Meeting of Japan CF Research Society

JCF18

November 24-25, 2017

Research Center for Electron Photon Science,

Tohoku University

Japan CF-Research Society

Edited by Yasuhiro Iwamura

Copyright © 2017 by Japan CF Research Society

All rights reserved. No part of this publication may be reproduced, stored in a retrieval system, or transmitted, in any form or by any means, electronic, mechanical, photocopying, recording or otherwise, without the prior permission of the copyright owner.

PREFACE

This is the proceedings of the 18th Meeting of Japan CF-Research Society (JCF18), which was held on November 24-25, 2017 at Mikamine Hall, Research Center for Electron Photon Science, Tohoku University, Sendai, Japan. In this meeting, 12 presentations were given and 6 papers were submitted to the editorial board. They have been peer reviewed by the referees, and revised for the publication as the proceedings.

For all meetings, JCF1 through JCF17, we published the Proceedings. For the meetings after JCF4, we published electronic versions of the proceedings on our web-site http://jcfrs.org/proc_jcf.html in addition to their printed versions. In view of low efficiency and low effectiveness in distributing information, we decided to discontinue the printed version for the meetings, JCF12. Only the electronic versions have been published thereafter. Any questions and comments are welcomed for the proceedings.

Finally, we would like to thank all the participants and the people who have collaborated in organizing this meeting.

Editor-in-Chief
Yasuhiro Iwamura, Tohoku University
November 2018

CONTENTS

Preface: Y. Iwamura ---------- i

Deuterium desorption experiments using Pd–Zr and Pd–Ni–Zr multi-layered samples
Y.Sato, K.Ota, K.Negishi, S.Narita ---------- 1

Comparison of excess heat evolution from zirconia-supported Pd-Ni nanocomposite samples with different Pd/Ni ratio under exposure to hydrogen isotope gases
A. Kitamura, A. Takahashi, K. Takahashi, R. Seto, T. Hatano, Y. Iwamura, T. Itoh, J. Kasagi, M. Nakamura, M. Uchimura, H. Takahashi, S. Sumitomo, T Hioki, T. Motohiro, Y. Furuyama, M. Kishida, H. Matsune ---------- 14

Reproducibility on Anomalous Heat Generation by Metal Nanocomposites and Hydrogen Isotope Gas
Y. Iwamura, T. Itoh, J. Kasagi, A. Kitamura, A. Takahashi, K. Takahashi, R. Seto, T. Hatano, T. Hioki, T. Motohiro, M. Nakamura, M. Uchimura, H. Takahashi, S. Sumitomo, Y. Furuyama, M. Kishida, H. Matsune ---------- 32

In-situ XRD and XAFS Analyses for Metal Nanocomposites Used in Anomalous Heat Generation Experiments
T. Hioki, K.Nakazawa, A. Ichiki, T. Motohiro, A. Kitamura, A. Takahashi, K. Takahashi, R. Seto, T. Hatano, Y. Iwamura, T. Itoh, J. Kasagi, M. Nakamura, M. Uchimura, H. Takahashi, S. Sumitomo, T Hioki, T. Motohiro, Y. Furuyama, M. Kishida, H. Matsune ---------- 45

Nuclear Fusion Mechanism in Metal Crystals
K. Ooyama ---------- 55

Water Clusters Related to OHMASA-GAS
H. Miura ---------- 93

Deuterium desorption experiments using Pd–Zr and Pd–Ni–Zr multi-layered samples

Y.Sato*, K.Ota, K.Negishi, S.Narita

Faculty of Science and Engineering, Iwate University
Morioka, Iwate, 020-8551, Japan
*g0317076@iwate-u.ac.jp

ABSTRACT

We performed deuterium desorption experiments using multi-layered Pd complex samples and investigated their deuterium diffusion and thermal behavior. In our recent study, we have tested Pd–Zr and Pd–Ni–Zr complex samples. We also tested multi-layered complex samples with a fine-structured interface. We frequently observed heat evolution in the deuterium desorption process simultaneously with a change in the electric resistance of the sample. This phenomenon is believed to be the result of a specific property of the Pd coated with Zr membrane in deuterium diffusion. In addition, we observed a short-period temperature fluctuation in the desorption process for the Pd–Ni–Zr with a fine-structured interface. A similar behavior was observed for a Pd–Ni sample with a fine-structured interface. This indicates a unique property of the Pd-coated Ni membrane sample, that is, deuterium diffusion from the Pd to the Ni membrane and from the membrane to the Pd is likely to occur frequently and periodically.

1. Introduction

In a previous study, we performed deuterium desorption experiments using various types of multi-layered complex samples, such as Pd–Ni, Pd–Ag, and Pd–Ti, and we observed anomalous heat evolution [1–3]. In addition, anomalous heat evolution was observed in a deuterium desorption experiment with Ni-based nano-composites supported by zirconia [4]. In these experiments, the phenomenon could be attributed to a specific property in deuterium diffusion with metal complexes, as well as the nano-scale fine structure of the sample. Furthermore, considering that Zr probably has a specific property in deuterium diffusion and in catalytic support as well, we performed a deuterium desorption experiment using multi-layered Pd–Zr and Pd–Ni–Zr complex samples and investigated the thermal behavior in the deuterium diffusion process. In the experiment, we also tested the multi-layered complex samples with a fine-structured interface to investigate whether such a structure can induce or enhance the anomalous phenomena.

2. Heat of the Deuterium Solution

The thermal diffusion behavior of deuterium depends on the heat of deuterium dissolution. Metals are generally classified as exothermic or endothermic absorbers of hydrogen. Ni and Ag are classified as endothermic absorbers, while Pd, Ti, and Zr are classified as exothermic absorbers. Considering the heat of dissolution, we can understand the deuterium diffusion behavior at the interface of the metal from the thermal behavior. The dissolution heats of Pd, Zr, Ti, Ni, and Ag for deuterium are shown in Table 1 [5].

Table 1 Heat of solution for deuterium.

Metal	Heat of solution (kJ/molH)
Pd	−10
Zr	−63
Ti	−53
Ni	16
Ag	68

3. Experiment

Sample preparation

Multi-layered samples were fabricated by depositing a thin metal membrane by Ar+ ion beam sputtering onto the surface of a Pd foil substrate. The size of the Pd foil used in this study was 10 mm × 10 mm × 0.1 mm. For the Pd–Zr, the thickness of the membrane was ~200 nm, while for the Pd–Ni-–Zr, the thickness of each membrane was ~50 nm. We also fabricated samples with a fine structure at the interface between the Pd foil and the membrane. These fine structures were obtained by etching the Pd membrane using an Ar ion beam. Figure 1 shows the surface morphology before and after etching, as analyzed by atomic force microscopy (AFM). The etched surface has a projected shape with a width of about 2 μm and a height of 200 nm.

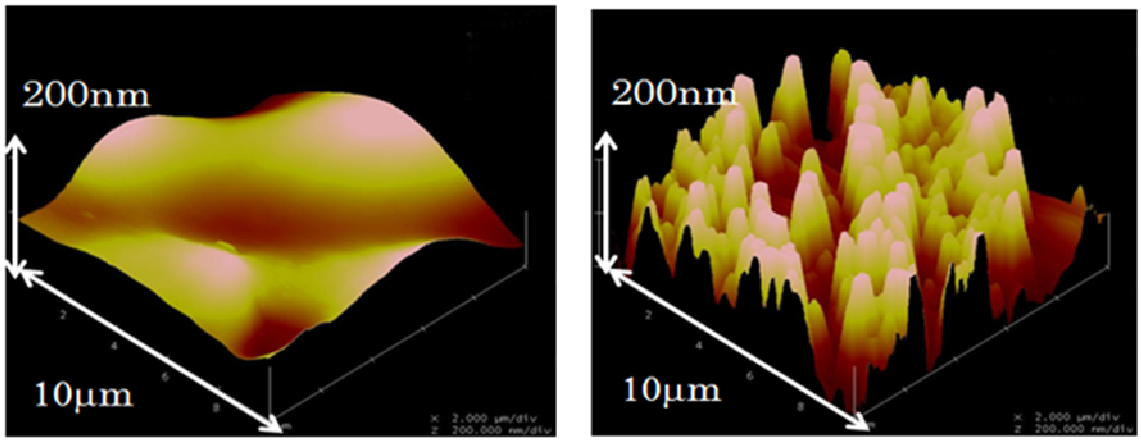

Fig. 1 Surface morphology before (left) and after (right) etching, observed by AFM.

The number of trials for each condition is shown in Table 2.

Table 2 Sample conditions and number of runs in the present study.

Sample type	Membrane material	Fine-structured interface	Number of runs
i	Zr	No	13
ii		Yes	10
iii	Ni, Zr	No	18
iv		Yes	11

Deuterium loading

The samples were exposed to D_2 gas at 5 atm for ~24 h. The weight of the samples was measured before and after loading, and the loading ratio (D/Pd) was calculated from the weight difference. Figure 2 shows the loading ratio D/Pd and its average for each sample. The D/Pd values for other types of samples we have tested until now are also shown in the plot.

The average loading ratio was found to be 0.65–0.70 for most samples, and no significant difference in the D/Pd values of each sample was observed, although the D/Pd ratios for the Pd–Zr and Pd–Ni–Zr are somewhat widely distributed. Thus, the D/Pd is apparently not affected by the interface structure or by the type of deposited metal film.

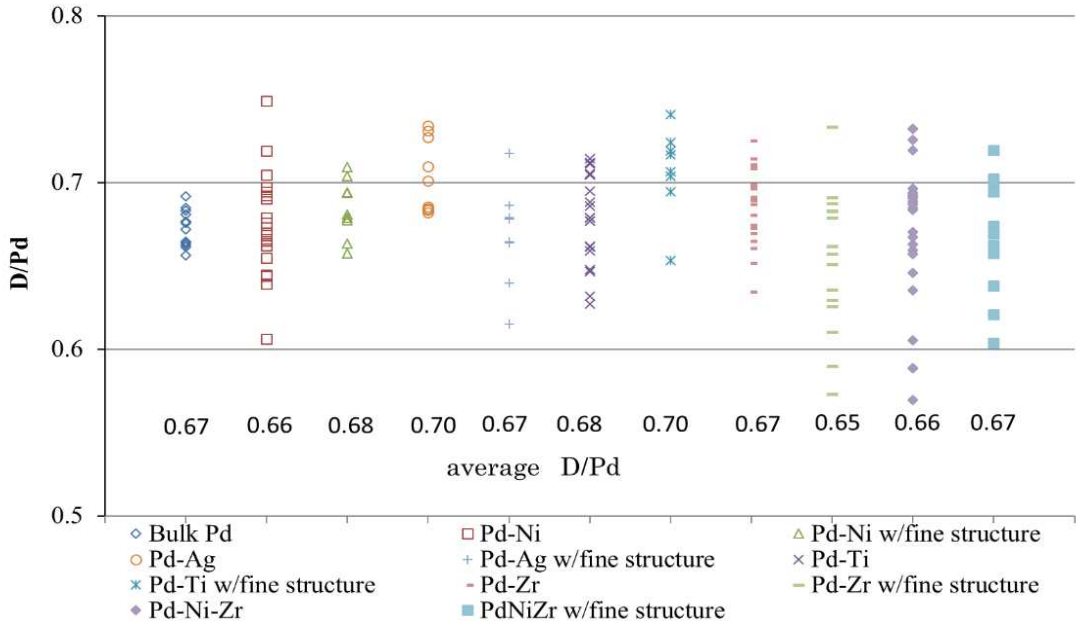

Fig. 2 Average D/Pd ratio of each sample structure.

Deuterium desorption

After the sample was weighed to measure the D/Pd ratio, it was placed in a chamber, which was evacuated by a turbomolecular pump (~10^{-4} Pa). In the chamber, the sample was heated by supplying constant direct current (DC) power to stimulate deuterium out-diffusion from the sample. In the desorption test, the sample temperature and the pressure in the chamber were monitored continuously for ~24 h. A thermocouple and an ionization gauge were used for these measurements. The current and bias applied to the sample were also monitored during the experiment.

4. Results and Discussions

We observed the different thermal behaviors in deuterium diffusion for each of the samples, which has already been reported for the Pd–Zr sample at the JCF17 meeting. In addition to these results, we show the results of samples with Pd–Zr with a fine-structured interface, Pd–Ni–Zr, and Pd–Ni-–Zr with a fine-structured interface.

Pd–Zr samples

Figure 3 shows the time-dependences of the sample temperature, the pressure in the chamber, and the applied voltage for the Pd–Zr sample. After the DC current was applied to the sample, we observed a sudden temperature increase with the increase of the voltage. This

temperature behavior was observed in 11 out of the 13 runs for the Pd–Zr sample. This temperature increase is regarded as the result of Joule heating due to the increase in the voltage. As the DC current is constant for the Zr membrane side of the sample, the applied voltage depends on the resistance of the Zr membrane, that is, the deuterium content of the Zr membrane. Moreover, the correlation between the change in voltage and the change in pressure was observed simultaneously, as shown in Fig. 3. The following scenario is a possible explanation for this behavior. After a DC current was applied to the sample, the sample temperature increased and deuterium diffused in the sample. Subsequently, the deuterium was stored in the Zr membrane, and the electric resistance of the Zr membrane increased according to the increase of the applied voltage. Once the deuterium density in the membrane reached a certain level, the deuterium was desorbed, resulting in an increase in pressure and decrease in voltage. A schematic view for this scenario of deuterium diffusion is shown in Fig. 4.

A similar behavior to that of the Pd–Zr sample was observed for the Pd–Zr with a fine-structured interface in 8 out of 10 runs. Among them, an increase of temperature and voltage was observed several times in 4 out of 10 runs as shown in Fig. 5. This phenomenon is regarded as the result of deuterium diffusion occurring from Pd to Zr where deuterium is desorbed intermittently.

Figure 6 shows an SEM image of the Zr membrane surface after the desorption experiment. The surface of the sample in which we observed a sudden temperature and voltage increase is compared with that of the sample without such an increase. We clearly observed the change in the surface of the samples in which a sudden temperature increase occurred. This suggests that a large amount of deuterium was desorbed from the membrane surface. Thus, we believe that the combination of Pd and Zr may set the direction of deuterium diffusion from Pd to Zr.

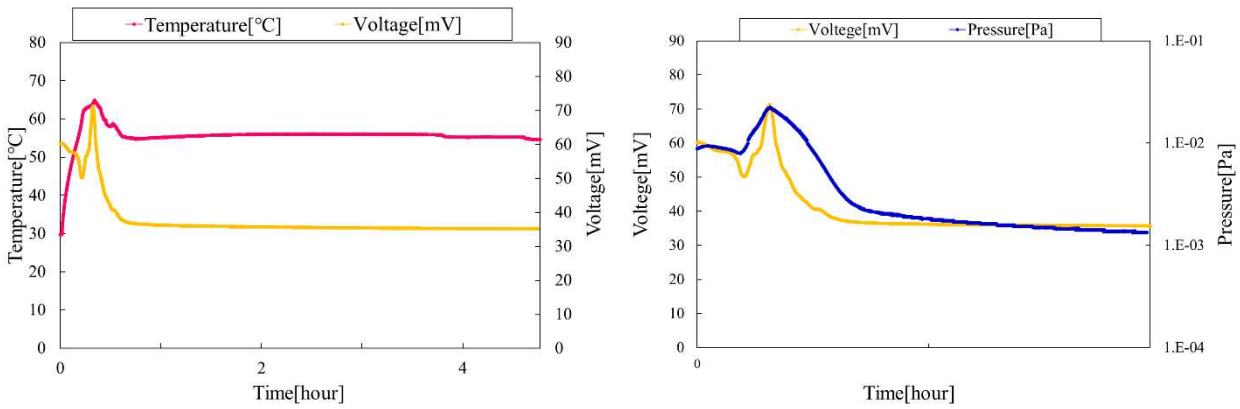

Fig. 3 Temperature and applied voltage vs. time (left) and applied voltage and chamber pressure vs. time (right) for Pd–Zr.

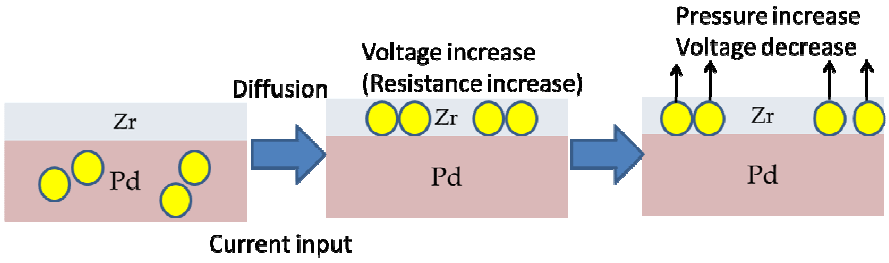

Fig. 4 Schematic view of deuterium diffusion/desorption in the Pd–Zr sample

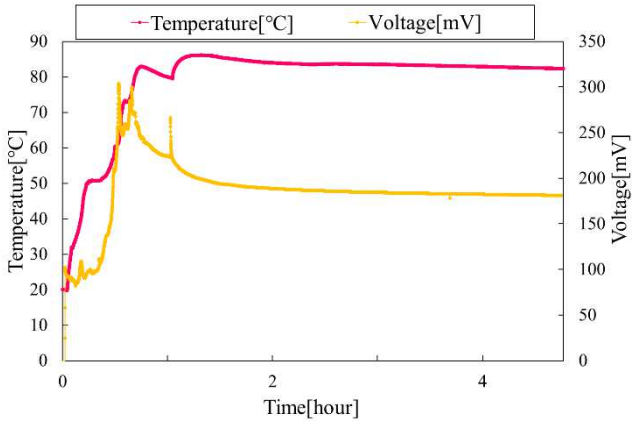

Fig. 5 Temperature and applied voltage vs. time for Pd–Zr with a fine structure.

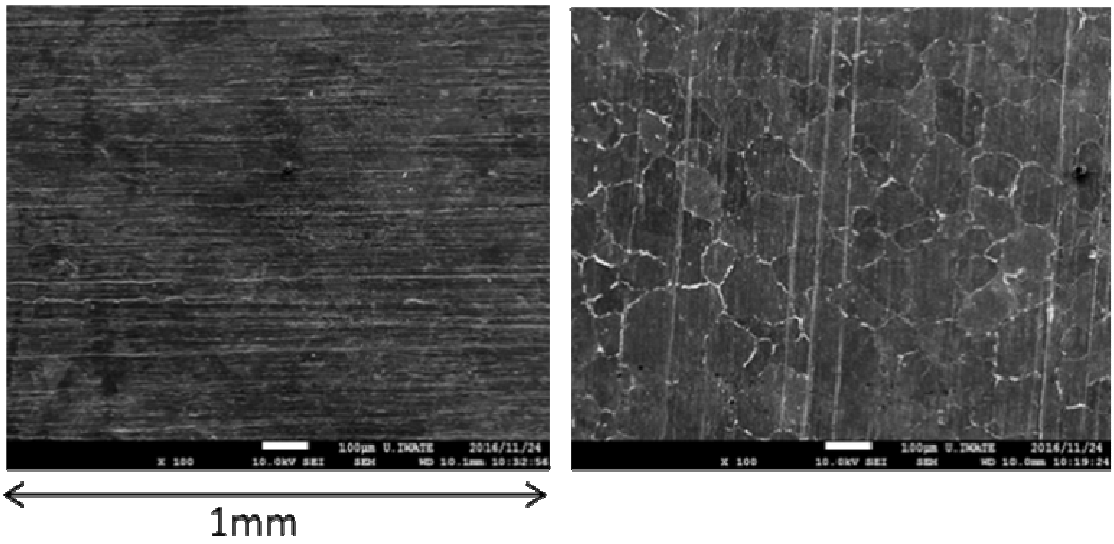

Fig. 6 SEM image of a Zr membrane of Pd–Zr samples in which a sudden temperature increase was not observed (left) and observed (right).

Further specific behaviors were observed as well, as shown in Fig. 7. We observed a short-period fluctuation in temperature. However, we did not observe a significant variation of the pressure inside the chamber during the continuous temperature fluctuation, which suggests that a significant quantity of deuterium atoms was not desorbed from the sample. We observed this phenomenon in 2 out of 13 runs for the Pd–Zr sample and 2 out of 10 runs for the Pd–Zr sample with a fine-structured interface. Thus, it is possible that deuterium diffusion from Pd to Zr and from Zr to Pd occurred frequently in this period and that the endothermic and exothermic phenomena associated with the heat of the solution repeatedly occurred owing to the deuterium transport between the two metals, as shown in Fig. 8.

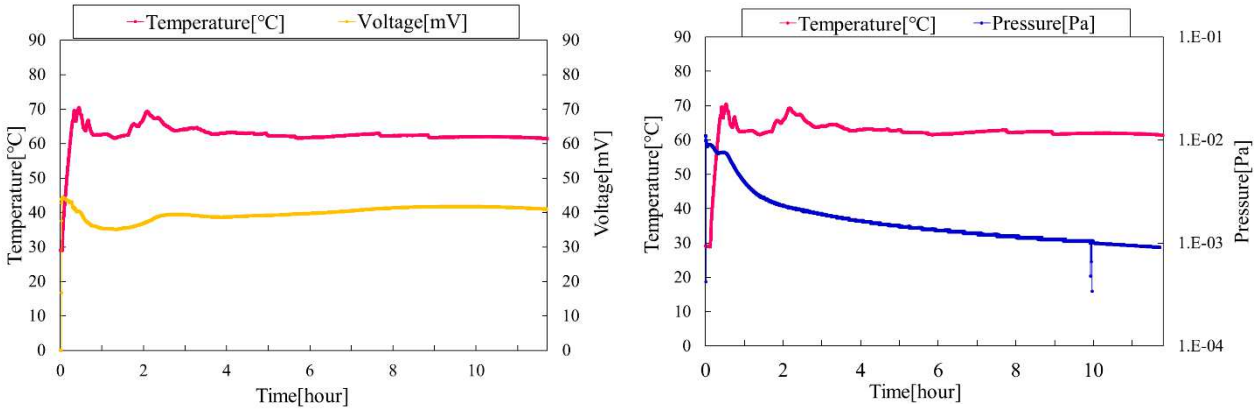

Fig. 7 Temperature and applied voltage vs. time (left) and temperature and chamber pressure vs. time (right) for Pd–Zr.

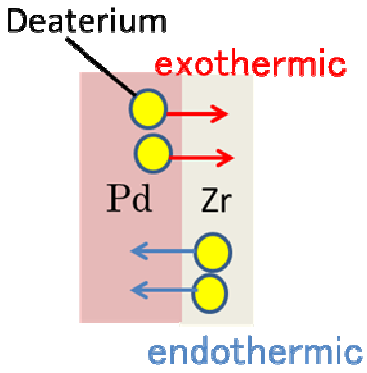

Fig. 8 Schematic view of deuterium diffusion.

Pd–Ni–Zr sample

A simultaneous increase of the temperature and voltage was observed in 16 out of 18 runs for the Pd–Ni–Zr sample, although the variation patterns were different for each run as shown in Figs. 9, 10, and 11. If these phenomena are the result of a specific deuterium diffusion, such that shown in Fig. 4, it indicates that a slight difference in the condition of the membrane structure or the composition of Pd–Ni–Zr complex can affect the behavior of deuterium diffusion, which results in different thermal behaviors.

In addition, no specific temperature behavior was observed in 2 out of 18 runs, as shown in Fig. 12. This phenomenon is considered to be a result of continuous deuterium desorption from the Pd side. After a DC current was applied to the sample, the surface temperature increased owing to Joule heating, and deuterium desorption began. As the sample resistance is decreased by the desorption of deuterium, the applied voltage decreases as well. In addition, deuterium desorption from Pd is an endothermic reaction; thus, the temperature of the sample gradually decreased.

We examined the correlation between the temperature behavior and the sample surface condition using SEM. SEM images of the Zr membrane surfaces after the desorption experiment are shown in Figs. 9–12. Figure 13 shows an SEM image of the sample surface for the deuterium unloading sample. Although the grain boundaries, which can be referred as evidence for hydrogen embrittlement, are clearly seen for certain samples, (e.g. in Figs. 9 and 11), the correlation between the patterns and the temperature and voltage behaviors cannot be established. Thus, the induction mechanism for the complicated temperature behavior has still not been understood.

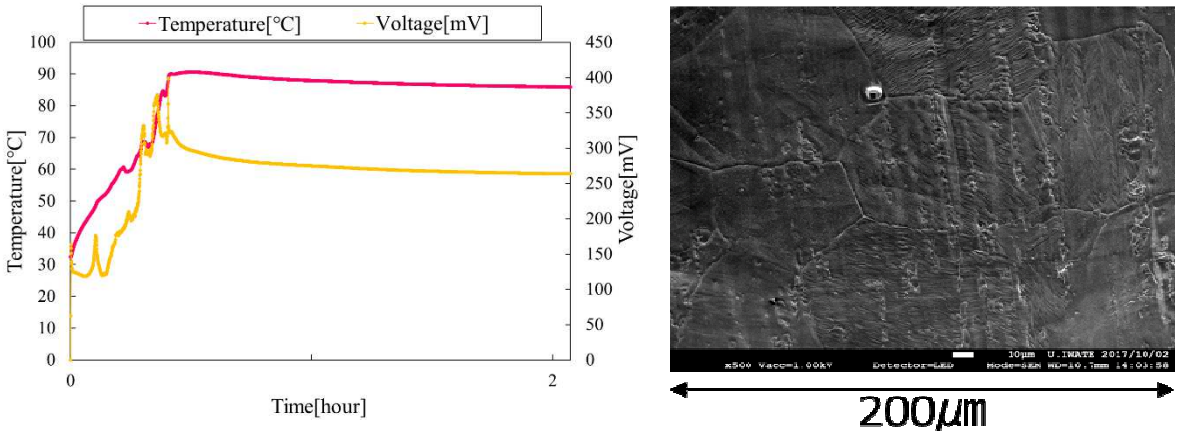

Fig. 9 Temperature and applied voltage vs. time for the Pd–Ni–Zr sample (left) and SEM image of the Zr membrane of the Pd–Ni–Zr sample (right).

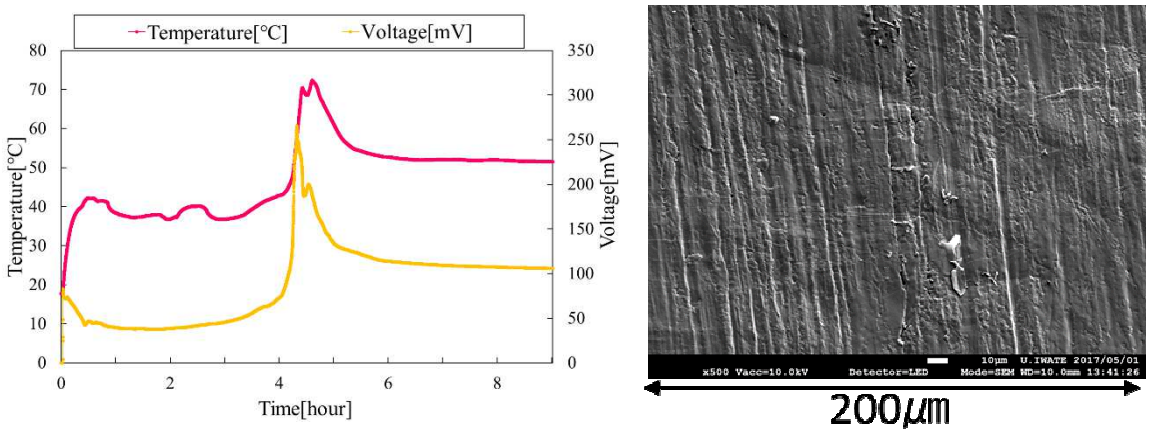

Fig. 10 Temperature and applied voltage vs. time for the Pd–Ni–Zr sample (left) and SEM image of the Zr membrane of the Pd–Ni–Zr sample (right).

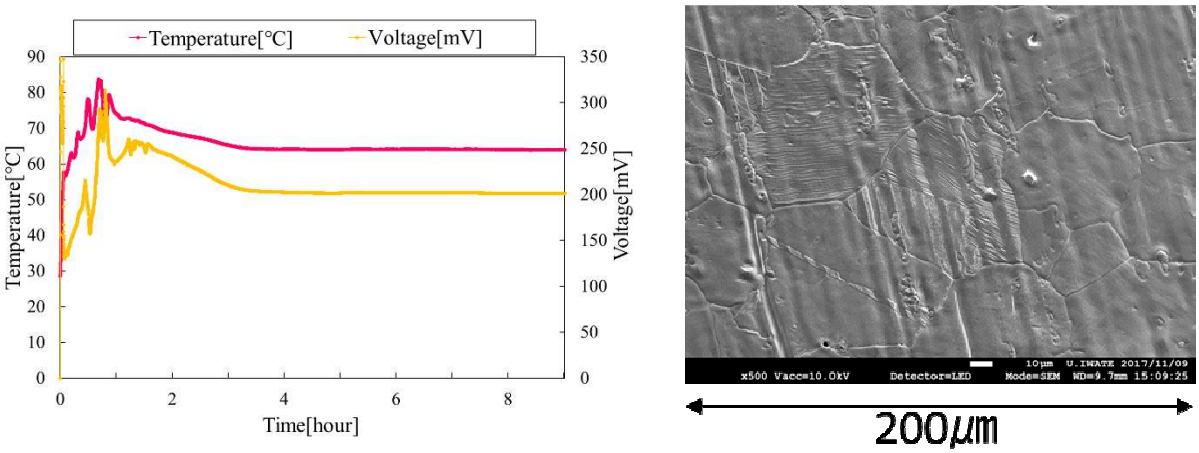

Fig.11 Temperature and applied voltage vs. time for the Pd–Ni–Zr sample (left) and SEM image of the Zr membrane of the Pd–Ni–Zr sample (right).

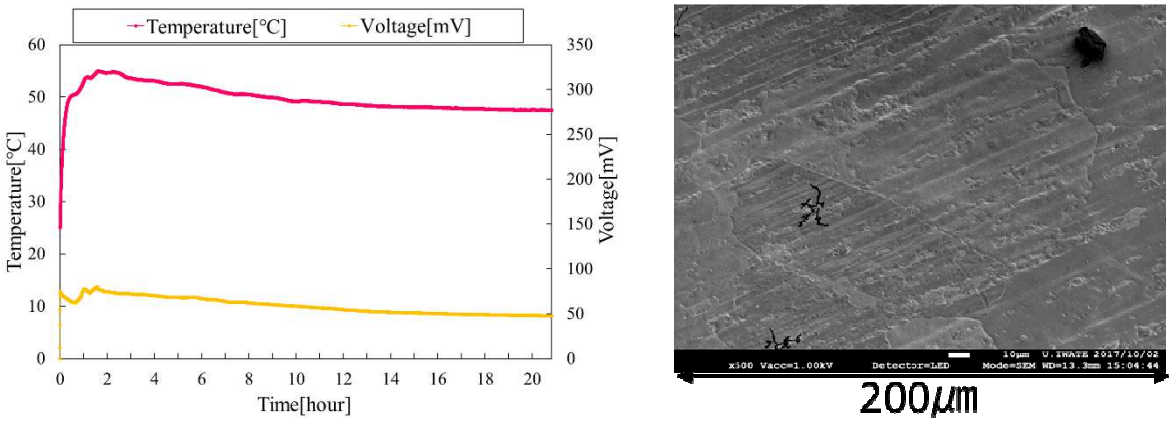

Fig. 12 Temperature and applied voltage vs. time for the Pd–Ni–Zr sample (left) and SEM image of the Zr membrane of the Pd–Ni–Zr sample (right)

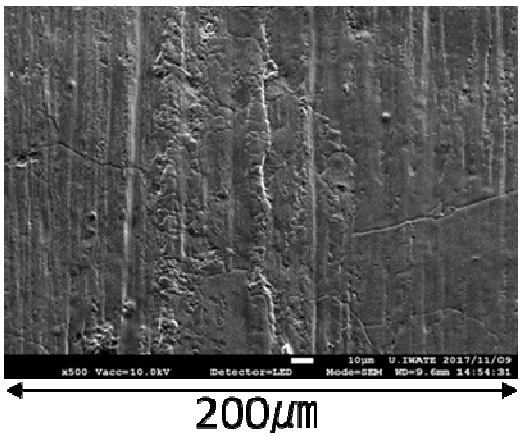

Fig. 13 SEM image of the Zr membrane of the Pd–Ni–Zr sample
(Deuterium unloading sample)

Pd–Ni–Zr with a fine structure interface sample

For Pd–Ni–Zr with a fine structure interface, we observed a short-period fluctuation in temperature, as shown in Fig. 14. This behavior was observed in 6 out of 11 runs. In this phenomenon, we did not observe a significant variation in the pressure inside the chamber during the continuous temperature fluctuation. Similar temperature behavior was observed for the Pd–Ni sample with a fine-structured interface [2]. This phenomenon is considered to induce deuterium diffusion, similar to that shown in Fig. 8. As this temperature behavior was observed frequently in the sample with a fine structure between Pd and Ni, such an interface structure may promote deuterium diffusion in the region.

Moreover, a temperature increase with the increase of voltage was observed in 2 out of 11 runs. Typical behavior is shown in Fig. 15. This phenomenon indicates that deuterium diffusion from Pd to Zr occurs, and deuterium was desorbed intermittently as shown in Fig. 5. In addition, no specific temperature behavior was observed in 3 out of 11 runs. This phenomenon indicates continuous deuterium desorption from the Pd side.

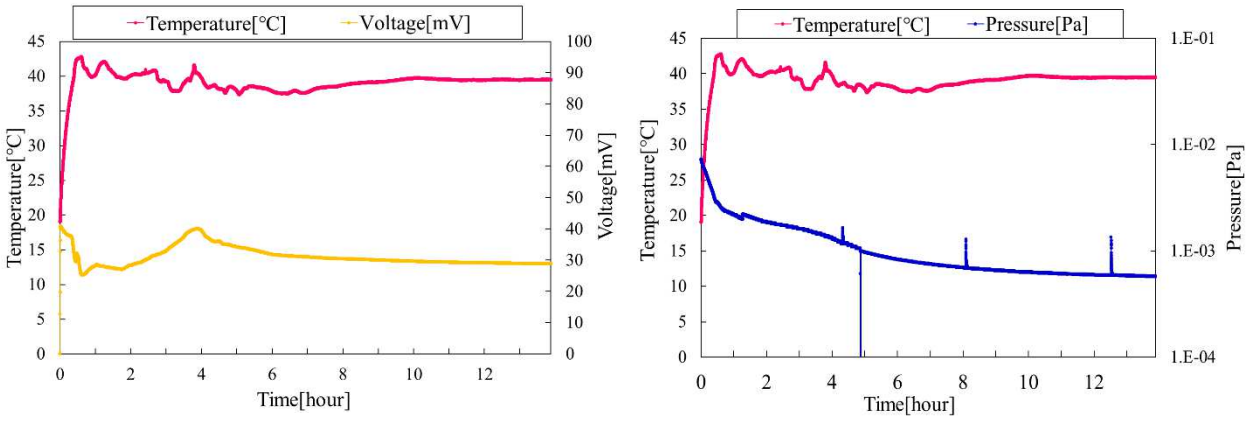

Fig. 14 Temperature and applied voltage vs. time (left) and temperature and chamber pressure vs. time (right) for Pd–Ni–Zr with fine structure.

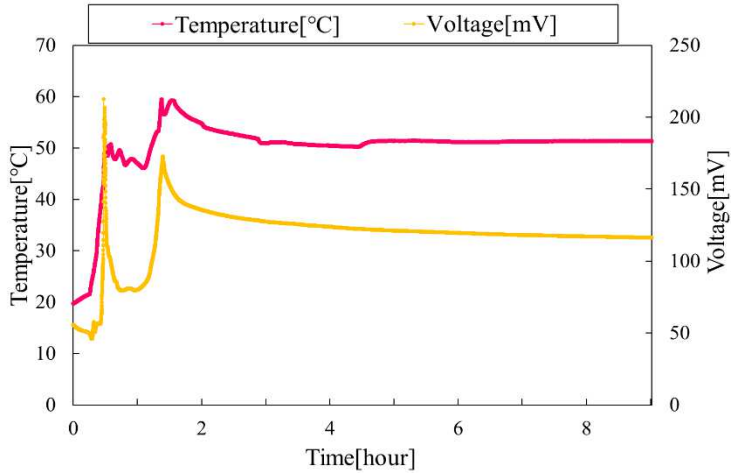

Fig. 15 Temperature and applied voltage vs. time for Pd–Ni–Zr with fine structure.

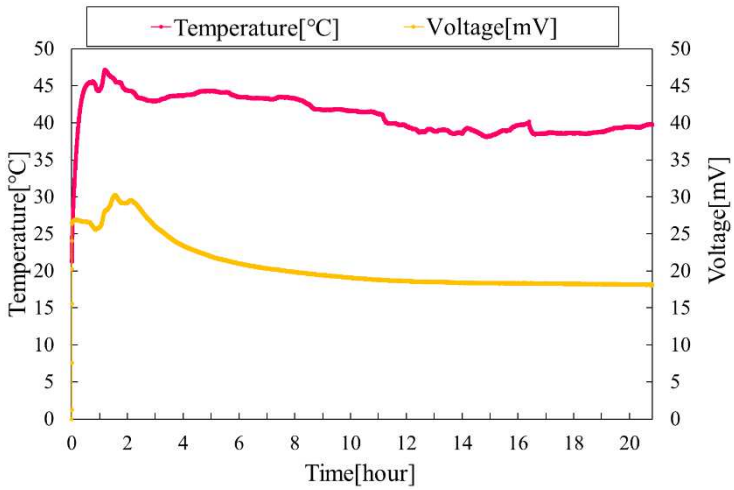

Fig. 16 Temperature and applied voltage vs. time for Pd–Ni–Zr with fine structure.

We classified the temperature behaviors into three patterns: Pattern I = no specific temperature variation, Pattern II = short-period fluctuation in temperature, and Pattern III = temperature increase with voltage increase. Table 3 shows the number of runs classified into each pattern for the sample we have tested thus far. Pattern I behavior was observed most frequently for the Pd–Ni, Pd–Ag, and Pd–Ti samples, but never for Pd–Zr. Although this pattern itself can be explained reasonably well by well-known processes, it is not clear why it was not observed for Pd–Zr. Pattern II was observed frequently in the sample with a fine structure between Pd and Ni. Pattern III was observed frequently in samples combining Pd and Zr, and was not observed in samples using endothermic absorbers (Ni, Ag).

Table 3 The number of runs classified into each pattern.

Sample / Pattern	Pd–Ni		Pd–Ag		Pd–Ti		Pd–Zr		Pd–Ni–Zr	
	i	ii	iii	iv	v	vi	vii	viii	ix	x
I	18	11	11	5	11	7	0	0	2	3
II	0	6	0	1	2	2	2	2	0	6
III	0	0	0	0	4	0	11	8	16	2

4. Summary

We performed deuterium desorption experiments using multi-layered Pd–Zr and Pd–Ni–Zr complex samples and investigated the thermal behavior in the deuterium diffusion process. We also studied multi-layered complex samples with a fine-structured interface. For the Pd–Zr and Pd–Ni–Zr samples, we frequently observed a temperature increase with the increase of the voltage, which was not observed for samples using endothermic absorber membranes, such as Ni or Ag. Thus, the combination of Pd and Zr may promote deuterium diffusion from Pd to Zr and the deuterium may be densified in Zr and desorbed. Furthermore, for the Pd–Ni–Zr sample with a fine-structured interface, we observed a short-period temperature fluctuation. A similar temperature behavior was observed for the Pd–Ni sample with a fine-structured interface. Thus, a fine structure between the Pd and Ni may promote deuterium diffusion between them.

References

[1] H. Kudo, S. Kataoka, K. Ota, S. Narita, “Deuterium adsorption test using Pd-Ni and Pd-Ag multi-layered samples”, Proc of JCF15 (2015) 20.

[2] S. Kataoka, H. Kudou, K. Ota, and S. Narita, “Deuterium desorption experiments using multi-layered metal samples with fine-structured surface”, Proc of JCF16 (2016) 29.

[3] S. Narita, S. Kataoka, Y. Sato, K. Negishi, K. Ota, “Characterization of deuterium diffusion in multi-layered metal samples”, Proc of JCF17 (2017) 28.

[4] A. Kitamura, E. F. Marano, A. Takahashi, R. Seto, T. Yokose, A. Taniike, and Y. Furuyama, “Heat evolution from zirconia-supported Ni-based nanocomposite samples under exposure to hydrogen isotope gas”, Proc of JCF16(2016) 1.

[5] Y. Fukai, K. Nakata, Y. Utida, “Suiso-to-Kinzoku” (1998) (in Japanese), “Utidaroukakuho”, 29.

Comparison of excess heat evolution from zirconia-supported Pd-Ni nanocomposite samples with different Pd/Ni ratio under exposure to hydrogen isotope gases

Akira Kitamura[1,5], Akito Takahashi[1], Koh Takahashi[1], Reiko Seto[1], Takeshi Hatano[1],
Yasuhiro Iwamura[2], Takehiko Itoh[2], Jirohta Kasagi[2],
Masanori Nakamura[3], Masanobu Uchimura[3], Hidekazu Takahashi[3], Shunsuke Sumitomo[3],
Tatsumi Hioki[4], Tomoyoshi Motohiro[4], Yuichi Furuyama[5],
Masahiro Kishida[6], Hideki Matsune[6]

[1] Technova Inc., 100-0011 Japan,
[2] Research Center for Electron Photon Science, Tohoku University, 982-0826 Japan,
[3] Research Division, Nissan Motor Co., Ltd., 237-8523 Japan,
[4] Green Mobility Research Institute, Institutes of Innovation for Future Society,
Nagoya University, 464-8603 Japan,
[5] Graduate School of Maritime Sciences, Kobe University, 658-0022 Japan,
[6] Graduate School of Engineering, Kyushu University, 819-0395 Japan

E-mail: kitamuraakira3@gmail.com

Abstract Anomalous heat effect by interaction of hydrogen isotope gas and nanoparticles supported by zirconia, $PdNi_{10}/ZrO_2$ ("PNZ6" and "PNZ6r") and $PdNi_7/ZrO_2$ ("PNZ7k"), has been examined. Excess power of 3 ~ 24 W from PNZ6 at elevated temperature of 200 ~ 300 °C continued for several weeks. The PNZ6 and PNZ6r samples with Pd/Ni=1/10 generated much higher excess power than PNZ7k with Pd/Ni=1/7. The Pd/Ni ratio is one of the key factors to increase the excess power. The maximum phase-averaged sorption energy, $\eta_{av,j}$, exceeded 270 keV/D, and the integrated excess energy, E_a, reached 1 keV/Pd·Ni. It is impossible to attribute the excess energy to any chemical reaction; it is possibly due to some unidentified radiation-free nuclear process.

Index Terms – Zirconia supported nanoparticles, $Pd{\cdot}Ni/ZrO_2$, hydrogen isotope gas, absorption and desorption, excess power, sorption energy of 270 keV/D.

I. INTRODUCTION

There have been increasing interests in experiments of hydrogen-gas charged nickel-based nano-composite samples for excess power generation, owing to higher availability of nickel than palladium. A Ni·Cu·Mn alloy thin wire, for example, has been examined extensively by Celani et al. [1]. In addition, a number of entrepreneurs are publicizing their own "products" of nano-fabricated samples on web sites with undisclosed details, and therefore with little scientific corroboration [e.g., 2 – 3]. Among them, replication experiments of the Rossi-type

reactors have been performed by several researchers [4 – 7], which seemingly appears to show unignorable reproducibility of the Rossi method. However, little is known about the accuracy of the calorimetry and the mechanism of the claimed anomalously large energy production.

On the basis of the 8 year-long (2008-2015) series of study on anomalous heat effects by interaction of metal nanoparticles and D(H)-gas under the collaboration of Technova Inc. and Kobe University, a collaborative research project has begun aiming at a new CO_2-free, distributed energy source [8]. This new project on MHE (Metal-Hydrogen Energy) was started on October 2015 under the collaboration of six Japanese organizations, one of which the individual author of the present paper belongs to. The results of the early-stage research program were reported in 20th International Conference on Condensed Matter Nuclear Science (ICCF20) [9, 10], 17th Meeting of Japan CF-research Society (JCF17) [11, 12] and 12th International Workshop on Anomalies in Hydrogen Loaded Metals [13, 14].

In the present work, we report results of observation of anomalous heat effect (AHE) by interaction of hydrogen isotope gas and zirconia-supported Pd-Ni nanocomposite samples done as the collaborative work using the experimental apparatus installed at Kobe University [15 - 18]. The system has a reaction chamber containing the sample with a capacity of 500 cc, and an oil-flow-calorimetry system capable of working at elevated temperatures up to 300 °C with use of a liquid hydrocarbon coolant, Barreltherm-400. The samples tested so far as the collaborative work include zirconia-supported $PdNi_x$ nanoparticles ("PNZ"), where x is 7 or 10. In the present paper, heat-generation characteristics of PNZ samples with different x, under rather constant pressure condition after D(H)-absorption (or during effectively net desorption) process are discussed.

II. EXPERIMENTAL PROCEDURE AND SAMPLES

The PNZ samples, PNZ6 and PNZ7k, were prepared by the melt-spinning method similar to that used in ref. [19]. The alloy-compounds of $Pd_{0.044}Ni_{0.306}Zr_{0.65}$ were prepared by arc-melting of the component metal blocks. The alloys were melted again by RF heating, and rapidly solidified with a melt-spinning machine to make ribbon-like thin sheets of amorphous $Pd_{0.044}Ni_{0.306}Zr_{0.65}$ compounds. The thin sheets were calcined in air at a temperature of 450 °C for 60 hours, during which the preferential formation of ZrO_2 supporter zone with isolated distribution of nano-structure zones of $PdNi_x$ is expected. They were then pounded in a mortar to make the sample particles with diameter of several to tens of μm.

The specifications of the samples are tabulated in Table 1. Those of the PNZ6r sample, which is the reused PNZ6 after re-oxidation (re-calcinated PNZ6), are also shown in the figure for comparison. Atomic ratio of Pd/Ni was 1/7 for PNZ7k as for other PNZ samples tested so far [8, 15, 17, 18], while that for PNZ6 (and therefore for PNZ6r) was chosen to be 1/10

to see the effect of the Pd/Ni ratio variation on the excess heat magnitude. The oxygen content was evaluated from the weight difference before and after the calcination/re-calcination. The ZrO_2 filler powder is of 1-mm diameter zirconia particles. About 95% of 500 cc volume of the reaction chamber was filled with the zirconia filler, and only about 5% was occupied by the mixed PNZ test sample for AHE measurement.

Table 1. Atomic composition of PNZ6, PNZ6r and PNZ7k sample

Sample	Mass (g)	Molar ratio				ZrO_2 filler mass (g)
		Ni	Pd	Zr	O	
PNZ6	124.2	**0.318**	**0.032**	**0.650**	0.240	1377
calcined at 450°C for 60h		10 : 1				
PNZ6r	131.9	**0.318**	**0.032**	**0.650**	1.03	1378
recalcined at 450°C for 60h		10 : 1				
PNZ7k	99.8	**0.306**	**0.044**	**0.650**	0.274	1531
calcined at 450°C for 60h		7 : 1				

ICP-AES and XRD analyses for some other PNZ samples, PNZ3, PNZ3r and PNZ4, other than those used in the present work were done at Nissan Motor Co. Ltd., Kyushu Univ., and Nagoya Univ. independently. Many interesting features including crystalline phases of $NiZr_2$, ZrO_2, etc. have been revealed, which will be published independently elsewhere.

STEM/EDS analyses for PNZ3, PNZ3r and PNZ4 samples (Pd/Ni = 1/7 for these samples) done at Kobe Univ. showed interesting features of nano-structure of the PNZ samples: (1) Most Pd and Ni atoms occupy the same position. (2) After absorption runs, $NiZr_2$ decreased, and ZrO_2 increased. (3) After re-calcination, the apparent majority became ZrO_2 + NiO + PdO [8, 18].

For the present samples, PNZ6, PNZ6r and PNZ7k, neither ERD, ICP-AES nor STEM/EDS were performed. However, there is no reason to assume characteristics different from PNZ3, PNZ3r and PNZ4 samples for formation of nano-structure.

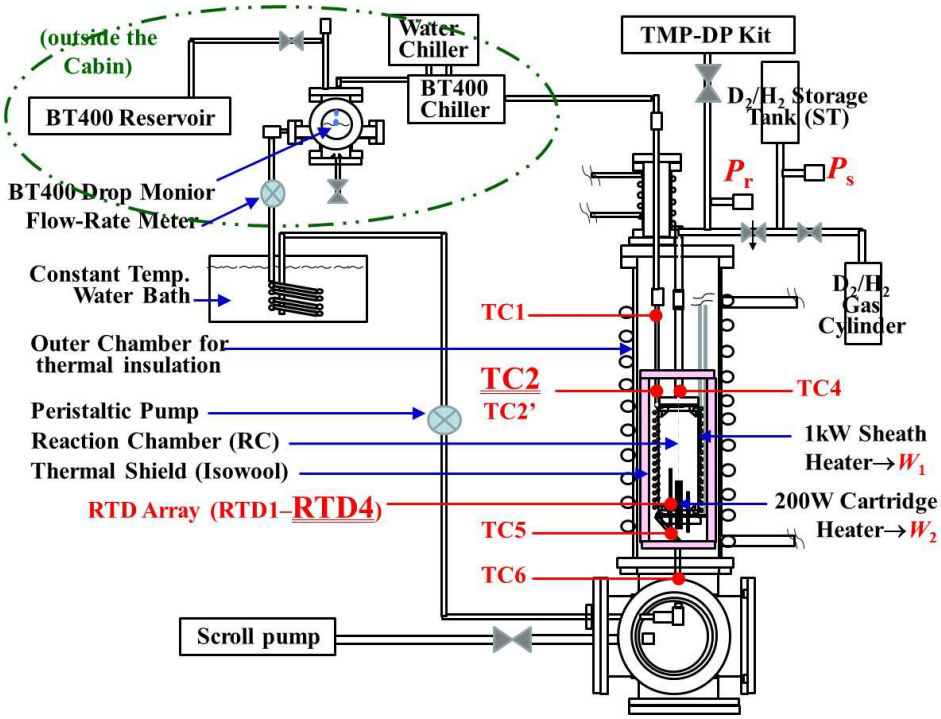

Fig. 1. Schematic of C_1 MHE-experimental system equipped with oil-flow-calorimetry system with flow-rate-monitors and dual heaters mounted on the reaction chamber (RC).

A schematic of the D(H)-gas-charging-calorimetry system C_1 is shown in Fig. 1. Refer to the references [9, 11] for detailed description of the system. Calibration of the flow calorimetry with a flow rate of 20 cc/min was performed using the 1500-g pure ZrO_2 filler. The heat conversion coefficient from the power to the oil-outlet temperature T_{C2} at TC2, dT_{C2}/dW = 1.57 °C/W or 1.0 °C/W, was obtained at room temperature (RT) or at 300 °C, respectively. The heat recovery rate, 0.88 – 0.83 in the temperature range from RT to 300 °C, was calculated by

$$R_h = F^{\alpha}\cdot\rho\cdot C\cdot(T_{C2}-T_{C6})/(W_1+W_2), \quad (1)$$

where F, ρ and C are the flow rate, the mass density and the specific heat capacity, respectively, of the coolant BarrelTherm-400 (BT400), Matsumura Oil Co. Ltd., and W_1 and W_2 the power of the outer sheath heater (#1) and the inner cartridge heater (#2), respectively. The parameter α is determined empirically as follows. A correction factor for the flow rate fluctuation ΔF (= $F - F_0$) to be subtracted from T_{C2} is derived from eq. (1);

$$\Delta T_{C2} = (dT_{C2}/dF)\cdot\Delta F = (-\Delta F/F)\cdot(W_1+W_2)\cdot(dT_{C2}/dW)\cdot\alpha. \quad (2)$$

The correction is applied to T_{C2} for some samples or gas species to determine α, so that the corrected temperature is not unreasonable, not giving negative excess temperature, or giving null excess for the Ar filling run, in the flow rate range of $0.825 \le F/F_0 \le 1$ for F_0 = 20 cc/min;

$$\alpha = 1.9\times10^{-2}\cdot\exp[4.0\cdot(F/F_0)]. \quad (3)$$

The calibration run serves also as a control run giving reference values of the temperatures, the flow rate of BT400 and the heater power for foreground runs using the zirconia-supported samples with the pure ZrO_2 filler. Comparing the temperatures in the foreground and background runs, the excess power will be calculated using the heat conversion coefficient mentioned above.

III. RESULTS AND DISCUSSION

(3-1) D(H)-Absorption

Deuterium (D) absorption runs, PNZ6#1, #2, #3 and #4, were performed after vacuum baking (#0) for more than 30 hours at RTD and TC2 temperatures of 200 - 300 °C with the heater power of (W_1+W_2) = (69+20) ~ (124+30) W and with the BT400 flow rate of 20 cc/min. The temperature history in the D-PNZ6#0 through #4 is shown in Fig. 2. Each time the heater power was varied, the phase number is advanced; #1-1 for D_2 introduction with the heater power of (0+0) W, #1-2 for (20+10) W, #1-3 for (30+20) W, and so on. At the end of each run, the heated sample was outgassed ("OG" phase) by evacuating the reaction chamber (RC), and the run number is advanced for the succeeding run started with filling of the fresh D_2 gas.

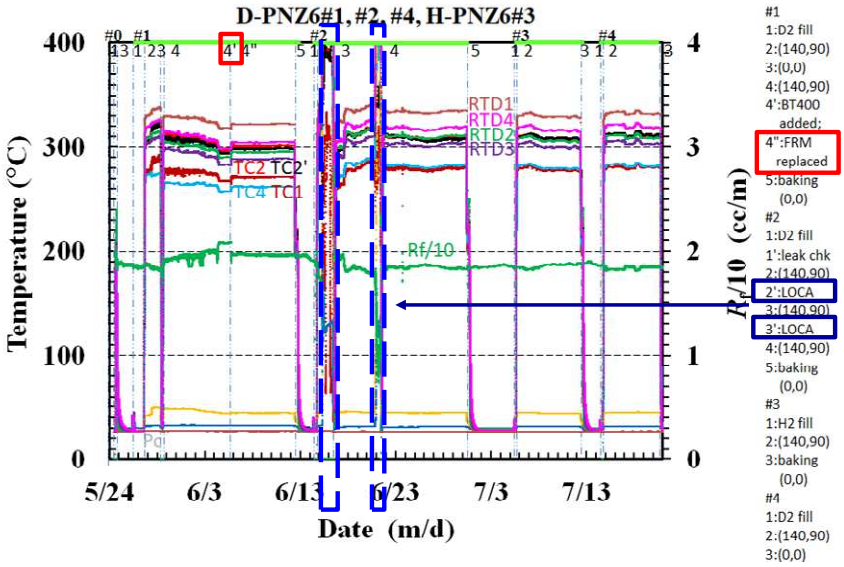

Fig. 2. Evolution of temperature and oil flow rate R_f in PNZ6#0 through #4 runs.

In the figure also shown is the variation of the flow rate R_f of BT400. Although R_f has rather large fluctuation of ~10%, the temperature variation due to the fluctuation of R_f is properly corrected for by eq. (2). In the #1 run, there was a trip of the flow-rate-meter (FRM). Then it was replaced with new one. Another trouble we encountered twice was the loss-of-coolant accident (LOCA) at #2-2' and #2-3' phases. In spite of these troubles, we observed rather stable temperature evolution giving large excess power.

In fig. 3 are shown the pressures at the RC and at the storage tube (ST), P_r and P_s, respectively, and the apparent loading ratio $L_M \equiv$ (D/M) or (H/M), *i.e.*, the number of hydrogen isotope atoms lost from the gas phase relative to the number of metal atoms (Pd and Ni in PNZ runs). The loading ratio is calculated from the values of P_r and P_s, and volumes of the RC and the ST with a correction for the temperature based on the Boyle-Charles' law using the averaged temperature of four RTD's.

It should be noted that the apparent loading ratio L_M reaching 3.5 was exceptionally large in the #1-1 RT phase. It decreased to below 3.0 with elevating the temperature in #1-2 due to desorption. Then it increased gradually due to unexpected leakage of D_2 gas from the RT flanges. The large leakage continued until it was partly fixed at the end of the #2-3' phase, after which the leakage became much smaller. However, the leakage has little influence on L_M in the RT phases, #*n*-1 (n = 1 ~ 4).

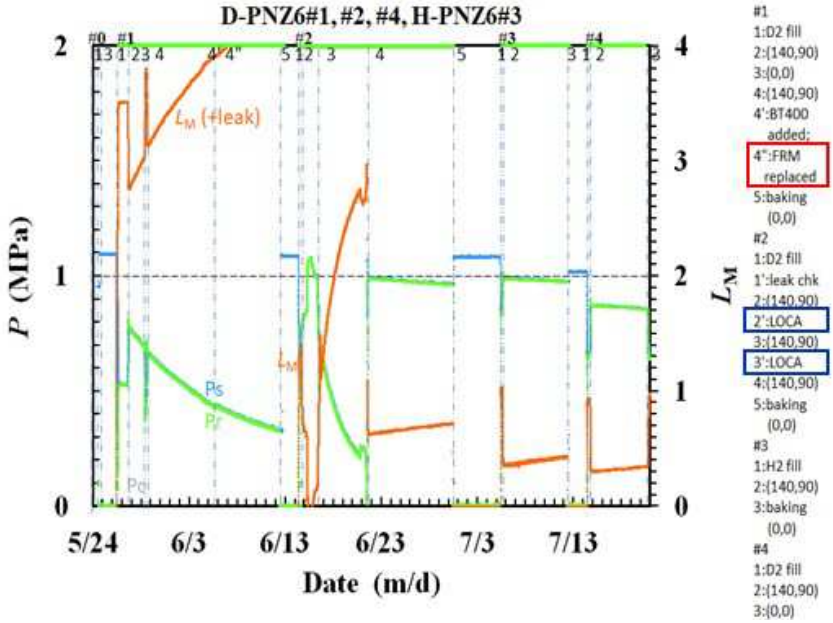

Fig. 3. Evolution of hydrogen loading ratio L_M (=D/M) and D(H)-gas pressure in PNZ6#1~#4 runs.

The variation of L_M with the leakage component subtracted is briefly discussed below. The sample after #0 baking is assumed to be composed of ZrO_2, $NiZr_2$, NiO and PdO based

on the XRD measurements. The possible sources of D consumption are reduction of oxides, (4) and (5) below, absorption by Pd and Ni, (6) and (7), and absorption by $NiZr_2$, (8);

$$PdO + D_2 \rightarrow Pd + D_2O + 1.77 \text{ eV/Pd}, \quad (4)$$

$$NiO + D_2 \rightarrow Ni + D_2O + 0.177 \text{ eV/Ni}, \quad (L_M = 2.0) \quad (5)$$

$$Pd + (a/2)D_2 \rightarrow PdD_a + 0.2 \text{ eV/Pd}, \quad (L_M = a) \quad (6)$$

$$Ni + (b/2)D_2 \rightarrow NiD_b + (0.1 \sim 0.2) \text{ eV/Ni}, \quad (L_M = b) \quad (7)$$

$$NiZr_2 + (c/2)D_2 \rightarrow NiZr_2D_c. + E_{NiZr2} \text{ eV/Ni}. \quad (L_M = c) \quad (8)$$

In elevated temperature phases #1-n ($n \geq 2$), desorption of D (reversed (6), (7) and (8)) would proceed, which makes L_M decrease.

At the end of the #1 run the sample was degassed by evacuating the RC at elevated temperature. By this procedure the gases produced by the reactions, D_2O ((4), (5)) and D_2 ((6), (7), (8)) are removed from the system. Then the sample composition after the #1 baking is thought to be ZrO_2, $NiZr_2$, $NiZr_2D_{c'}$ and reduced metals (Ni + Pd). Here it is assumed that $NiZr_2D_c$ and $PdD_a{\cdot}NiD_b$ lose D partially during desorption under elevated temperatures; only a part of $NiZr_2D_c$ turning back to $NiZr_2$ and/or $NiZr_2D_{c'}$ ($c' < c$), and similarly for $PdD_a{\cdot}NiD_b$. This together with the absence of the oxides would be one of the possible reasons why the D consumption in the #2-1 phase drastically decreased compared with that in the #1-1.

(3-2) Heat evolution at RT

The initial bursts of heat are observed on the RTD and TC traces at the beginning of the #1-1 phase at RT. Figure 4 shows the thermal power calculated from the temperature evolution in the #1-1 phase with the conversion factor mentioned above. The heat evolution has two peaks, simply because the D_2 gas was resupplied to the storage tube at 3.9 h after the initial introduction of D_2 gas. By the resupply the pressure of D_2 in the ST and therefore the flow rate of D_2 was increased to enhance the rate of heat evolution associated with absorption of D_2.

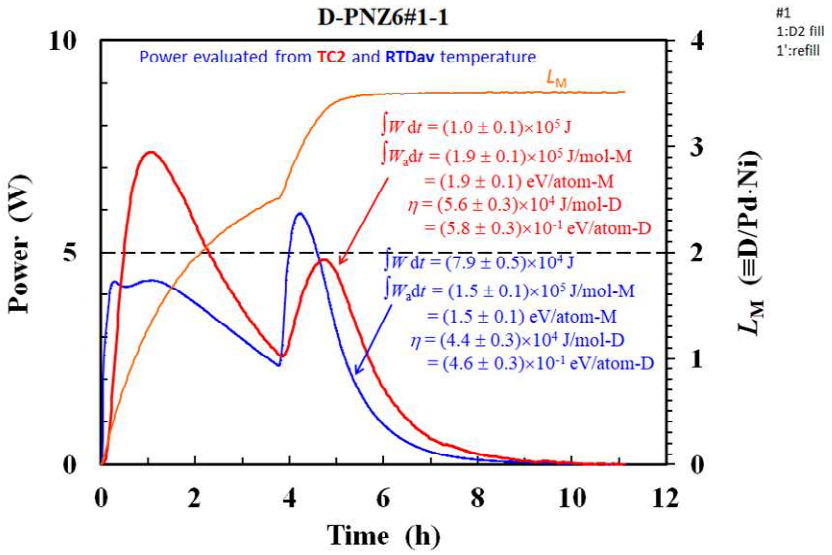

Fig. 4. Thermal power and deuterium loading ratio in the RT phase of the virgin sample run, D-PNZ6#1-1.

The hump at TC2 is time-integrated to calculate an emerging energy per an absorbent atom,

$$E_a = \int_0^t W_a \, dt, \tag{9}$$

where W_a is the power per an adsorbent atom, Pd and Ni in the present case. The energy E_a is calculated to be 1.9 ± 0.1 eV/atom-Pd. This is rather large in view of the hydrogen absorption energy of about 0.2 eV/atom-Pd for bulk crystalline Pd. The energy E_a is divided by L_M to obtain the specific energy per D atom adsorbed/absorbed or lost from the gas phase, $\eta \equiv E_a/L_M$ = (5.8±0.3)×10^{-1} eV/M, averaged over the #1-1 phase. Similarly, E_a and η are calculated for #*n*-1, where *n* is the integer representing the run number. Those together with L_M are summarized in Fig. 5, and compared with those for PNZ6r and PNZ7k samples.

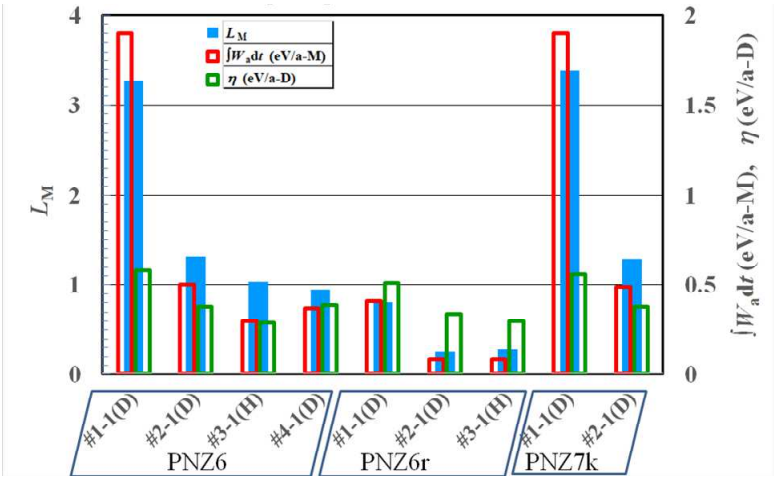

Fig. 5. Comparison of loading ratio and specific absorption energies in room temperature phases of PNZ6#1-1 through PNZ7k#2-1 runs.

Some conclusions are deduced from the figure. First of all, PNZ7k is similar to PNZ6 in regard to these quantities. The reproducibility is rather good.

Secondly, we notice the exceptionally large value of L_M at #1-1, and gradual decrease of L_M in the following phases. The difference between L_M in #1-1 and that in #2-1 is almost 2. As has been partly discussed in the preceding subsection, possible reasons for this large difference are the following. (1) In the elevated temperature phases only a part of $NiZr_2D_c$ liberate D_2 turning back to $NiZr_2$ or $NiZr_2D_{c'}$ ($c' < c$). The liberated D_2 gas is removed by evacuation at the end of the #1 run. (2) Similarly, only a part of $PdD_a{\cdot}NiD_b$ could liberate D_2 turning back to $PdD_{a'}{\cdot}NiD_{b'}$. (3) The oxides PdO·NiO to be deduced to metallic Pd·Ni by consuming D_2 is absent or very few in the #2 run.

Third, the specific absorption energies per D atom, η, have essentially the same value (0.3 ~ 0.4 eV/D) in PNZ6#*n*-1, where $n \geq 2$. This infers that the underlying physics is the same in the PNZ6#*n*-1 phases. In other words, this means that the reduction of PdO·NiO, if any, was almost completed in #1-1, and that the values of η in #*n*-1 ($n \geq 2$) are the intrinsic ones for the sample. Possible processes responsible to this are the deuterium absorption by Pd·Ni, eqs. (6) and (7), and by $NiZr_2$, eq. (8). Gradual decrease of L_M and E_a suggests that decomposition of $NiZr_2$ and/or some structural degradation of the Pd·Ni nanostructure are proceeding. The intrinsic $\eta \sim 0.8$ is much larger than that for the bulk Pd (~ 0.2 eV/a-D). Possible reasons for this are the following; (1) The absorption energy E_{NiZr2} in eq. (8) is rather large. (2) It might be possible that the absorption energies (6)·(7) become larger when Pd and Ni form nanocomposites. (3) It might also be possible that some unknown reactions other than absorption occur in the Pd·Ni nanocomposites. In #1-3 with the filling gas of H_2, η is

decreased by about 25% possibly due to the isotope effect. Anyway, it is difficult to discuss further these points before knowing the composition quantitatively.

Fourth, The PNZ6r runs have similar variation of L_M and E_a but with smaller amplitude. It appears that the numbers of the absorbers, $NiZr_2$ and NiO, are reduced in comparison with the PNZ6. It seems that, by re-calcination, some fraction of $NiZr_2$ are likely to be decomposed to ZiO_2 and Ni/NiO, and some fraction of Pd·Ni nanostructure might be changed to different one relatively inactive in regard to absorption.

(3-3) Heat evolution at ET

Next, we discuss the oil-outlet temperature T_{C2} in the elevated temperature phases in the PNZ6 runs, T_{C2}(PNZ6) (the red line in Fig. 6), in comparison with $T_{C2}(ZrO_2)$ in the calibration/control run using the zirconia powder (the black line in Fig. 6). As is shown, T_{C2}(PNZ6) is higher than $T_{C2}(ZrO_2)$ in most elevated temperature phases. When we take into account the fluctuation of the heater power and the flow rate as seen in Fig. 2, and apply the correction according to eq. (2), we obtain the curve shown as the green line in Fig.6.

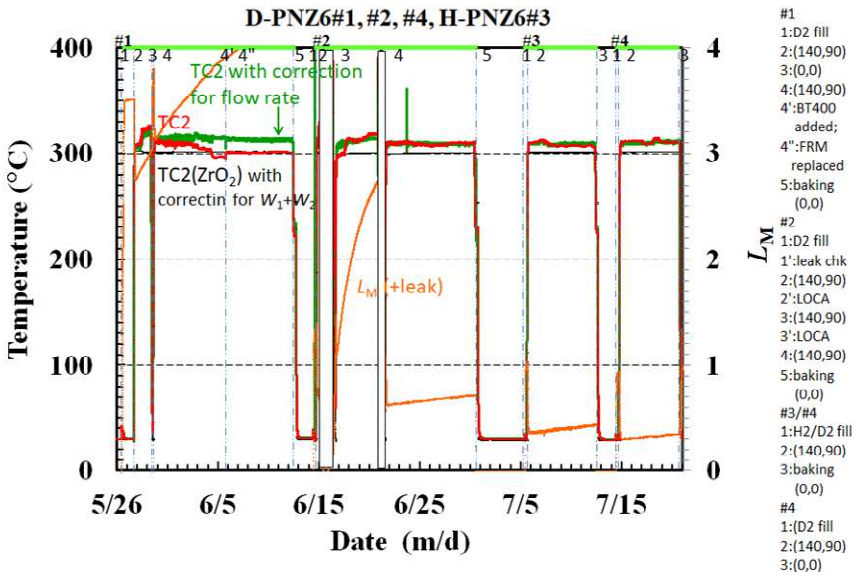

Fig. 6. Difference of TC2 temperature between the foreground (PNZ6) run and the blank (zirconia) run.

The difference is converted to excess power, W_{ex}, by dividing it by dT_{C2}/dW, and shown in Fig. 7. The excess power of 10 ~ 24 W is rather large. When we take into account the systematic error of ±2.3 W determined from fluctuations recorded in PSf1 runs [11], the maximum excess power is more than one order of magnitude higher than the error range. In the PNZ6 sample powder some anomalous effect is induced to generate excess power in all phases with the elevated temperature of 300 ~ 340 °C at RTD1 ~ RTD4.

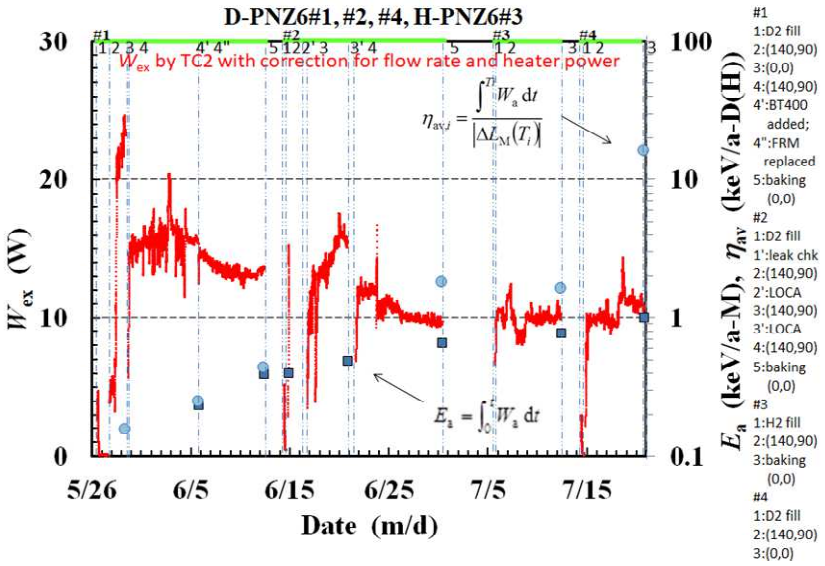

Fig. 7. Excess power, W_{ex}, integrated excess heat per metal atom, E_a (keV/M), and phase-averaged sorption energy per hydrogen isotope atom absorbed/desorbed, $\eta_{av,i}$ (keV/D(H)), in RT and ET phases evaluated by TC2 temperature

The phase-averaged sorption energy, $\eta_{av,i}$ (closed circles), and the integrated excess energy per an adsorbent atom, E_a (integrated W_{ex} per adsorbent atom; closed squares), in the elevated temperature phases are also plotted in Fig. 7. It should be noted that $\eta_{av,i}$ is defined as E_a divided by the absolute value of ΔL_M, the increment of adsorbed/absorbed or desorbed deuterium atoms in the relevant phase;

$$\eta_{av,i} \equiv \frac{\int_0^{T_i} W_a \, dt}{|\Delta L_M(T_i)|}, \tag{10}$$

The absolute value is taken to keep $\eta_{av,i}$ positive under desorption. This is because we assume that the exothermic event could occur along with hydrogen isotope displacement under both absorption and desorption. The maximum value of $\eta_{av,i}$ exceeds 10 keV/D, and the integrated output energy E_a reaches 1 keV/Pd·Ni.

The definition of $\eta_{av,i}$ is rather problematic, since the real number of the hydrogen atoms getting in and out of the surfaces of the nanoparticles is not always represented by $|\Delta L_M|$ in the denominator of eq. (10). However, even if we divide E_a by the total amount of D absorbed in each run, L_M, to evaluate the integrated output energy per an D atom participating in the absorption, the energy is still far beyond the value explainable by any chemical reaction; E_a/L_M = 460 eV/D = 44 MJ/mol-D in the D-PNZ6#4 run. The large values of the excess energy suggest the nuclear origin of the excess heat.

It is important to note that the sudden increase of W_{ex} in the #1-2 phase is really spontaneous. Figure 8 shows the unexpected, unintended evolution of excess power in the #1-2 phase having no correlation with fluctuation of the flow rate nor the input heater power. Figure 9 shows the temperatures at other TCs and RTDs during the same period of time. The unexpected, unintended evolution of excess power appears to originate in the peripheral region of RC. This is because the step-like increases of temperature are observed with much smaller amplitude in RTDs which are relatively insensitive to the temperature at the peripheral region. The excess power in the #1-2 phase reaching 24 W is largest among all sample runs tested so far.

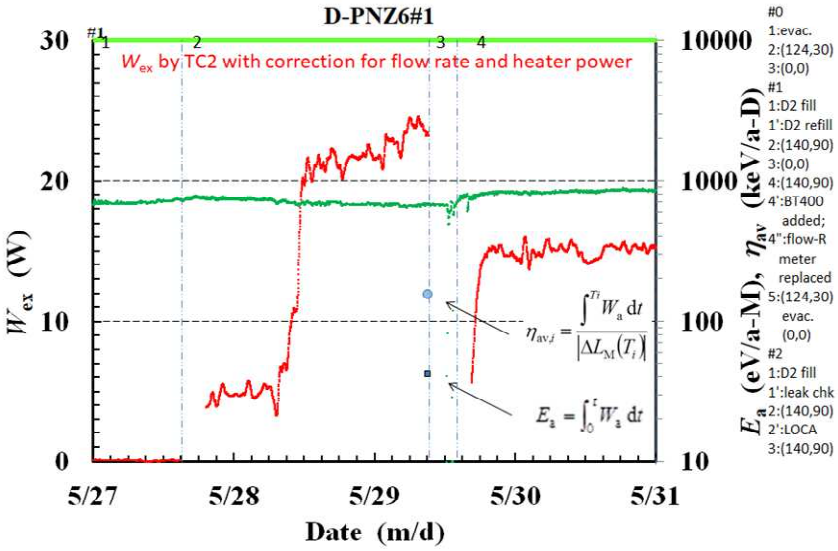

Fig. 8. Unexpected, unintended evolution of excess power with no correlation with the flow rate.

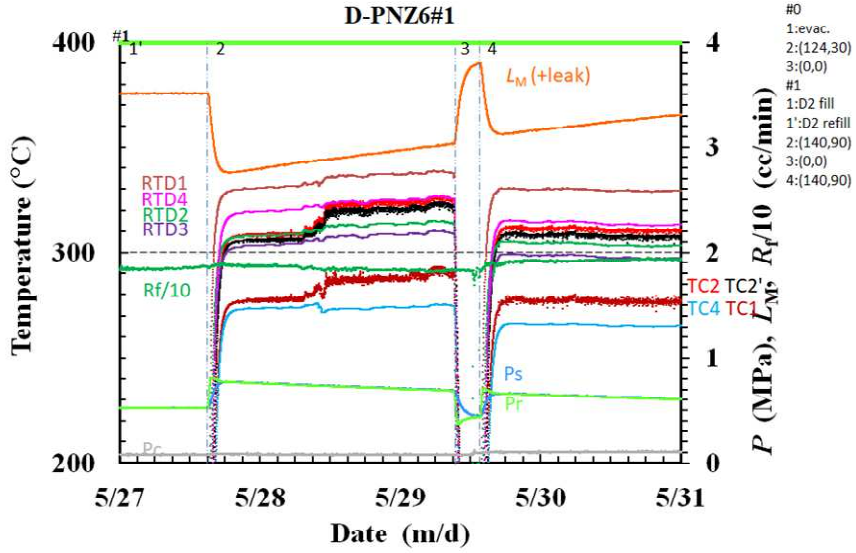

Fig. 9. Temperatures at TCs and RTDs, the loading ratio L_M and flow rate R_f, when the large excess power emerged.

The PNZ6 sample was re-calcined after finishing the PNZ6#4 run. The sample is called PNZ6r, and similar sequence of heater power application was given to the PNZ6r sample. As might be supposed from L_M for RT phases shown in Fig. 5, deuterium absorption is weaker than PNZ6; L_M in the ET phases, #1-2 through #1-5, is about 0.5 and smaller than 0.3 in #2-2 ~ 4 and #3-2 phases. Evolution of the excess power, W_{ex}, the integrated excess energy per metal atom, E_a, and the phase-averaged sorption energy per D atom absorbed/desorbed, $\eta_{av,i}$, in the PNZ6r runs are shown in Fig. 10. We see again rather large value of W_{ex} stably ranging from 5 to 10 W. Very large values of $\eta_{av,i}$ with the maximum value of 270 keV/D, and/or even the conservatively defined integrated excess energy E_a/L_M = 85 MJ/mol-D in the PNZ6r#1 run, make it realistic to assume nuclear origin of the excess heat.

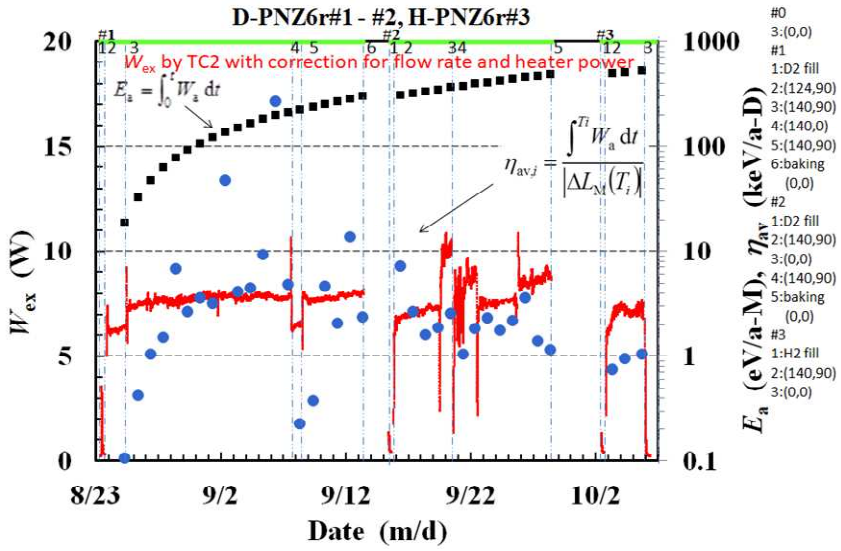

Fig. 10. Excess power, W_{ex}, and excess energies E_a (keV/M) and $\eta_{av,j}$ (keV/D(H)), in PNZ6r runs.

Figure 11 shows peculiar evolution of temperature observed in the PNZ6r#1-2 phase. Relatively large humps are recorded in the RTD1 and RTD2 traces. The figure also shows desorption under elevated temperature in #1-2 similar to other samples, but with exceptionally large time constant. The reason for these phenomena is not known.

However, it is very interesting to see that large positive excess power evolution was generated under the net desorption process as shown in Fig. 10 and Fig. 11. This effect seems to infer that nuclear-like reaction sites exist in the near-surface of $PdNi_x$ nano-composites.

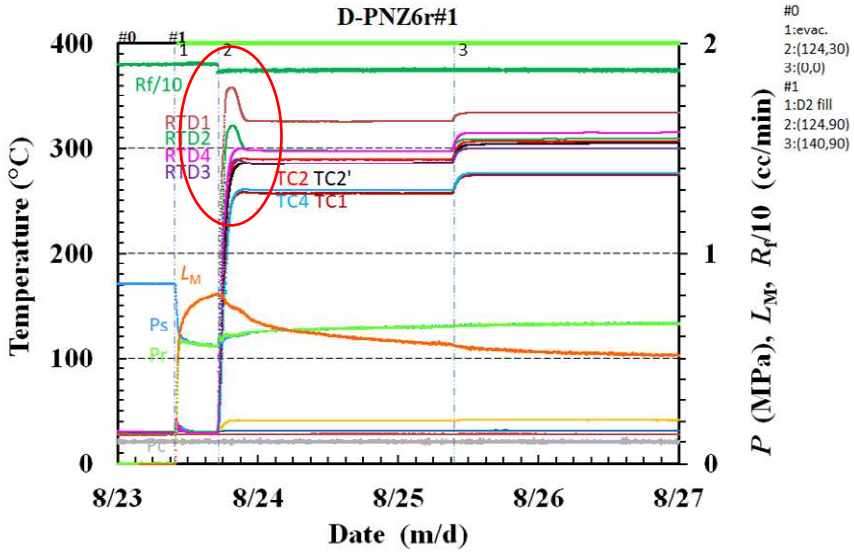

Fig. 11. Peculiar evolution of temperature in the D-PNZ6r#1-2 phase.

Finally, the excess power characteristics of PNZ7k sample with the atomic ratio of Pd/Ni = 1/7. As has been mentioned earlier, this sample in the RT phases shows characteristics very similar to those for the PNZ6 sample. The similarity is also true for L_M in the ET phases but without leakage. However, there is a large difference in excess power and energies. These are shown in Fig. 12. The excess power W_{ex} and accordingly the integrated excess energy E_a are appreciably small compared with that for PNZ6 and PNZ6r. As for the phase-averaged sorption energy, $\eta_{av,i}$, the values are not very small, yet remarkably large values are not observed. From these facts we conclude that the atomic ratio of binary adsorbent metal in the sample is one of the key factors to increase the excess power. The smaller the ratio of the minority species to the majority, the larger the excess power. However, we know that single-element nanoparticle sample never produce excess heat in ET phases [11]. We have to look for the most suitable ratio.

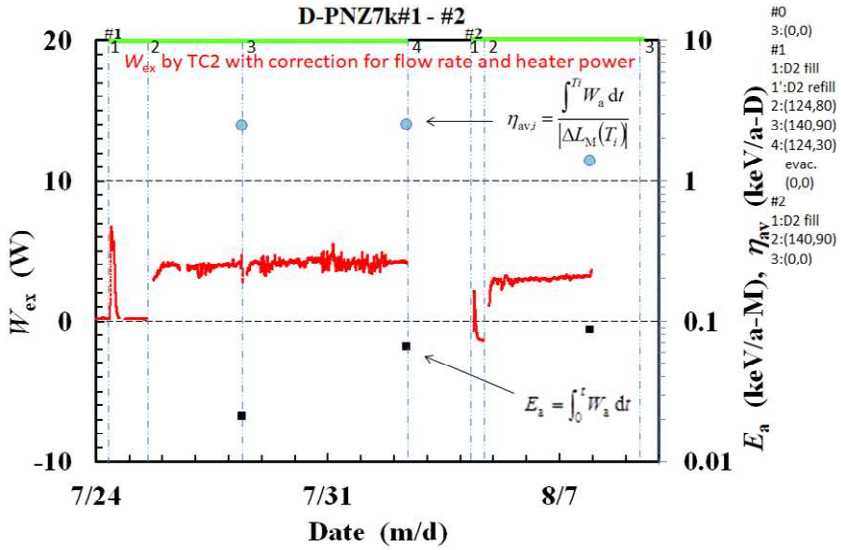

Fig. 12. Excess power, W_{ex}, and excess energies E_a (keV/M) and $\eta_{av,i}$ (keV/D(H)), in PNZ7k runs.

(3-4) Radiations

Finally, radiation measurements are discussed. An example of the result of measurements of γ-ray counting rate and neutron dose rate is shown in Fig. 13. The γ-ray counting rate and the neutron dose rate are steady with rather large fluctuation, except for a period with high neutron dose rate in middle July. However, the period agrees with the period when the accelerator in the next room was operated in the neutron emitting mode. We conclude that no observable level of hard radiation accompanies the excess heat at least up to the power level observed in the present work.

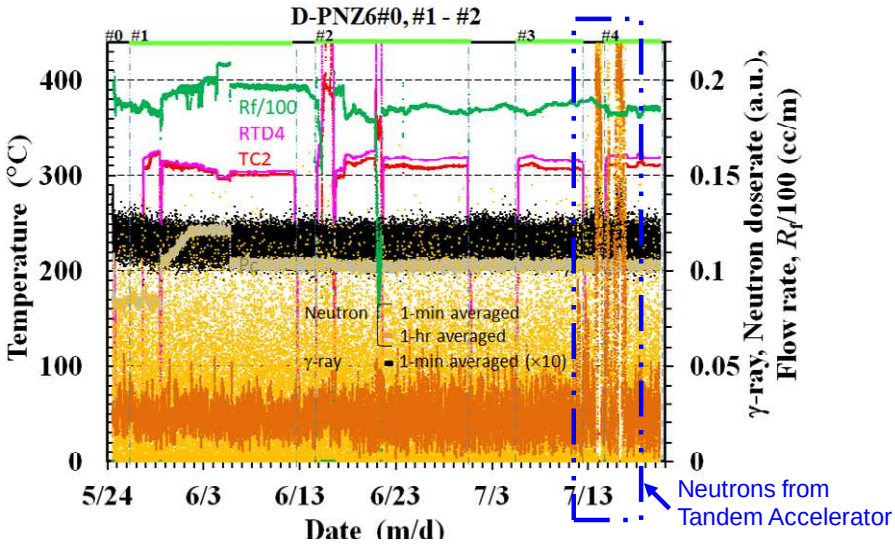

Fig. 13. Radiations and temperatures at TC2 and RTD4 in PNZ6 runs.

IV. SUMMARY AND CONCLUDING REMARKS

Hydrogen isotope absorption and heat evolution have been examined for three kinds of ZrO_2-supported Pd·Ni nanocomposites, PNZ6, PNZ6r, and PNZ7k. The results are summarized as follows;

(1) Excess power of 3~24W at elevated temperature of 200~300°C continued for several weeks.

(2) PNZ6 and PNZ6r samples with Pd/Ni=1/10 generated much higher excess power than PNZ7k with Pd/Ni=1/7. The Pd/Ni ratio is one of the keys to increase the excess power.

(3) The maximum phase-averaged sorption energy, $\eta_{av,i}$, exceeded 270 keV/D (26 GJ/mol-D), and the integrated excess energy, E_a, reached 1 keV/Pd·Ni (100 MJ/mol-M).

(4) It is impossible to attribute the excess energy to any chemical reaction; it is possibly due to radiation-free nuclear process.

(5) The anomalous heat effect was observed with very small amount of D(H) transfer in both direction of net absorption and net desorption. It is conceived that this might be a hint for AHE generation sites and some nuclear mechanism in the binary nano-metal composite samples.

References

[1] F. Celani, E. F. Marano, B. Ortenzi, S. Pella, S. Bartalucci, F. Micciulla, S. Bellucci, A. Spallone, A. Nuvoli, E. Purchi, M. Nakamura, E. Righi, G. Trenta, G. L. Zangari, and A. Ovidi, "Cu-Ni-Mn alloy wires, with improved sub-micrometric surfaces, used as LENR

device by new transparent, dissipation-type, calorimeter", J. Condensed Matter Nucl. Sci. **13** (2014) 56-67.

[2] F. Piantelli / Nichenergy; http://e-catsite.com/2012/06/15/piantelli-moves-closer-to-commercialization/.

[3] A. Rossi / Leonardo Corporation; http://ecat.com/.

[4] G. Levi, E. Foschi, B. Höistad, R. Pettersson, L. Tegner and H. Essen., http://www.sifferkoll.se/sifferkoll/wp-content/uploads/2014/10/LuganoReportSubmit.pdf.

[5] A. G. Parkhomov, International Journal of Unconventinal Science, **6**(2) (2014) 57-61; ibid. **7**(3) (2015) 68-72; ibid. **8**(3) (2015) 34-39.

[6] S. Jiang, http://ja.scribd.com/doc/267085905/New-Result-on-Anomalous-Heat-Production-in-Hydrogen-loaded-Metals-at-High-Temperature, (2015).

[7] J. Cole, http://www.lenr-coldfusion.com/2015/04/16/experiment-generates-apparent-excess-heat/, (2015).

[8] A. Takahashi, A. Kitamura, K. Takahashi, R. Seto, T. Yokose, A. Taniike and Y. Furuyama, "Anomalous Heat Effects by Interaction of Nano-metals and D(H)-gas", published in Proc. ICCF20 (2016), pp. 13-25, Tohoku University) .

[9] Akira Kitamura, Akito Takahashi, Koh Takahashi, Reiko Seto, Yuki Matsuda,Yasuhiro Iwamura, Takehiko Itoh, Jirohta Kasagi,Masanori Nakamura, Masanobu Uchimura, Hidekazu Takahashi,Tatsumi Hioki, Tomoyoshi Motohiro, Yuichi Furuyama, Masahiro Kishida, "Collaborative Examination on Anomalous Heat Effect Using Nickel-Based Binary Nanocomposites Supported by Zirconia", J. Condensed Matter Nucl. Sci. **24** (Proc. ICCF20) (2017) 202 - 213.

[10] Y. Iwamura, T. Itoh, J. Kasagi, A. Kitamura, A. Takahashi and K. Takahashi, "Replication Experiments at Tohoku University on Anomalous Heat Generation Using Nickel-Based Binary Nanocomposites and Hydrogen Isotope Gas", J. Condensed Matter Nucl. Sci. **24** (Proc. ICCF20) (2017) 191 - 202.

[11] A. Kitamura, A. Takahashi, K. Takahashi, R. Seto, T. Hatano, Y. Iwamura, T. Itoh, J. Kasagi, M. Nakamura, M. Uchimura, H. Takahashi, S. Sugitomo, T. Hioki, T. Motohiro, Y. Furuyama, M. Kishida, and H. Matsune, "Heat evolution from silica-supported nano-composite samples under exposure to hydrogen isotope gas", Proc. JCF17 (2017) 1-14.

[12] Y. Iwamura, T. Itoh, J. Kasagi, A. Kitamura, A. Takahashi, K. Takahashi, R. Seto, T. Hatano, T. Hioki, T. Motohiro, M. Nakamura, M. Uchimura, H. Takahashi, S. Sugitomo, Y.

Furuyama, M. Kishida, and H. Matsune, "Anomalous Heat Generation Experiments Using Metal Nanocomposites and Hydrogen Isotope Gas", Proc. JCF17 (2017) 15-27.

[13] Akira Kitamura, Akito Takahashi, Koh Takahashi, Reiko Seto, Takeshi Hatano, Yasuhiro Iwamura, Takehiko Itoh, Jirohta Kasagi, Masanori Nakamura, Masanobu Uchimura, Hidekazu Takahashi, Shunsuke Sumitomo, Tatsumi Hioki, Tomoyoshi Motohiro, Yuichi Furuyama, Masahiro Kishida, and Hideki Matsune, "Effect of Supporter Material on Heat Evolution from Ni-based Nano-Composite Samples under Exposure to Hydrogen Isotope Gas", presented at 12th Int. Workshop on Anomalies in Hydrogen-Loaded Metals, Costigliole d'Asti, Italy, 5-9 June 2017.

[14] Y. Iwamura, T. Itoh, J. Kasagi, A. Kitamura, A. Takahashi, K. Takahashi, R. Seto, T. Hatano, T. Hioki, T. Motohiro, M. Nakamura, M. Uchimura, H. Takahashi, S. Sugitomo, Y. Furuyama, M. Kishida, and H. Matsune, "Anomalous Heat Generation Experiments Using Metal Nanocomposites and Hydrogen Isotope Gas", presented at 12th Int. Workshop on Anomalies in Hydrogen-Loaded Metals, Costigliole d'Asti, Italy, 5-9 June 2017.

[15] A. Kitamura, A. Takahashi, R. Seto, Y. Fujita, A. Taniike and Y. Furuyama, “Brief summary of latest experimental results with a mass-flow calorimetry system for anomalous heat effect of nano-composite metals under D(H)-gas charging”, Current Science, **108**(4) (2015) 589-593.

[16] A. Kitamura, A. Takahashi, R. Seto, Y. Fujita, A. Taniike and Y. Furuyama, “Comparison of some Ni-based nano-composite samples with respect to excess heat evolution under exposure to hydrogen isotope gases”, Proc. JCF15 (2015) 1-19.

[17] A. Kitamura, A. Takahashi, R. Seto, Y. Fujita, A. Taniike, Y. Furuyama, “Effect of Minority Atoms of Binary Ni-Based Nano-Composites on Anomalous Heat Evolution under Hydrogen Absorption”, J. Condensed Matter Nucl. Sci. **19** (2016) 135-144 (Proc. ICCF19 (2015)).

[18] A. Kitamura, E. F. Marano, A. Takahashi, R. Seto, T. Yokose, A. Taniike and Y. Furuyama, “Heat evolution from zirconia-supported Ni-based nano-composite samples under exposure to hydrogen isotope gas”, Proc. JCF16 (2016) 1-16.

[19] Y. Arata and Y. Zhang; The special report on research project for creation of new energy; J. High Temperature Society 34 (2008) 85-93.

Reproducibility on Anomalous Heat Generation by Metal Nanocomposites and Hydrogen Isotope Gas

Yasuhiro Iwamura[1], Takehiko Itoh[1,7], Jirohta Kasagi[1], Akira Kitamura[2,5], Akito Takahashi[2], Koh Takahashi[2], Reiko Seto[2], Takeshi Hatano[2], Tatsumi Hioki[3], Tomoyoshi Motohiro[3], Masanori Nakamura[4], Masanobu Uchimura[4], Hidekazu Takahashi[4], Shunsuke Sumitomo[4], Yuichi Furuyama[5], Masahiro Kishida[6], Hideki Matsune[6]

1 Research Center for Electron Photon Science, Tohoku University, 982-0826 Japan
2 Technova Inc., 100-0011 Japan,
3 Green Mobility Research Institute, Institutes of Innovation for Future Society, Nagoya University, 464-8603 Japan,
4 Research Division, Nissan Motor Co., Ltd., 237-8523 Japan,
5 Graduate School of Maritime Sciences, Kobe University, 658-0022 Japan,
6 Graduate School of Engineering, Kyushu University, 819-0395 Japan
7CLEAN PLANET Inc., 105-0022 Japan

Abstract

Anomalous heat generation experiments using metal nanocomposites and hydrogen isotope gas based on Kitamura and Takahashi's work have been performed at Kobe and Tohoku Universities as a collaborative work to confirm the existence of the anomalous heat effects. As a result, the amount of anomalous heat generation per hydrogen or deuterium exceeded 1MJ/mol-H or D at least. The released energy is supposed to be very difficult to explain by known chemical processes only.

In this paper, we discuss reproducibility on obtained experimental results with PNZ ($Pd_{0.044}Ni_{0.31}Zr_{0.65}$) and CNZ ($Cu_{0.044}Ni_{0.31}Zr_{0.65}$) samples. Two independent excess heat experiments at Kobe and Tohoku Universities using PNZ7k and PNZ7s were conducted, respectively. Qualitative reproducibility between Kobe and Tohoku experiments was good. Generated excess energies for PNZ7k and PNZ7s were 3.4MJ/mol-D and 3.0MJ/mol-D, respectively.

As to CNZ samples, we performed two experiments using CNZ5s and CNZ6s with the same composition at Tohoku University. Anomalous excess heat generations were observed for the samples at elevated temperature (150℃-300℃). Generated excess energies per absorbed H for CNZ5s and CNZ6s were 6.5MJ/mol-H and 5.3MJ/mol-H, respectively. Coincident burst-like increase events of the pressure of reaction chamber and gas temperature, which suggested sudden energy releases in the reaction chamber, were observed for both experiments using CNZ5s and CNZ6s samples.

1. Introduction

Collaborative research between Technova Inc., Nissan Motor Co. Ltd., Kobe Univ., Kyushu Univ., Nagoya Univ. and Tohoku Univ. was performed from Oct. 2015 to Oct. 2017 based on Akira Kitamura and Akito Takahashi team of Technova Inc. and Kobe [1]-[3]. Objective of the collaborative research is to clarify the existence of the anomalous heat generation phenomena and contribute to the setup of a new national project by obtaining guiding principles on how to control it. For the purpose, anomalous heat experiments at Kobe and Tohoku Universities and sample preparations and analyses at Nissan, Kyushu, Nagoya

and Kobe Universities have been performed. Replication experiments were performed at Tohoku University using high quality heat measurement system similar to the apparatus at Kobe University.

The Research Center for Electron Photon Science of Tohoku University and CLEAN PLANET Inc. established collaborative research division - Condensed Matter Nuclear Reaction Division in 2015 [4] and research on anomalous heat generation started. Replication efforts have been made on two types of experiments as a first step at our division in Tohoku University; one is the present collaborative work [1]-[3], and the other is the experiment using nano Pd/Ni fabricated by glow discharge with D_2 gas [5].

2. Experimental

Schematic of our experimental apparatus is shown in Fig.1. It is basically based on the paper [1] and improved in some points. Experimental set-up was already described in [6] and [7]. The reaction chamber (RC) that contains Nickel-based binary nanocomposites and hydrogen isotope gas is shown in the center of the Fig.1. The RC is filled with and 1,300g weight ZrO_2 beads and Nickel-based nano-material shown in Fig.2. Heat generation from the RC is estimated by the Mass-Flow-Calorimetry. The inlet oil temperature (T_{in}) is measured by three independent thermocouples and the outlet oil temperature (T_{out}) is also measured by three thermocouples. A liquid hydrocarbon coolant enables us to use the flow-calorimetry method at elevated temperature. The coolant is driven by a digital liquid tubing pump. A sheath heater (W_1) are spirally wound on the outer surface of the RC and a cartridge heater (W_2) is located at the central axis of the RC to heat up the Nickel-based binary nanocomposites sample. The power to the heater is fed from a finely regulated DC power supply. The input electrical power for every heater is continuously monitored by two independent voltage and ampere meters to avoid mistakes on the input power estimation. H_2 or D_2 gas is fed from a reservoir through a super needle flow regulator to the sample in the RC. Pressures in the RC and the reservoir are continuously monitored. Temperature distribution in the RC is measured by 4 RTDs (Resistant Thermal Detectors) and temperatures along the oil coolant pipe and the stainless-steel pipe for gas introduction are monitored by thermocouples. A lot of temperature measurement points would enable us to judge whether an observed excess anomalous heat is real or not, although heat recovery of this system rate becomes low. All the apparatus is in a thermostatic chamber controlled at 23℃±0.1℃ to avoid the influence by the outside temperature fluctuation as shown un Fig.3.

Sample preparation and experimental procedures were given in [6] and [7]. At first, the RC was evacuated by a turbo molecular pump and then heated up to 200-300℃ to remove H_2O or other impurity gas such as hydrocarbon gas. After the baking, the RC is cooled down to room temperature. About 1.0MPa H_2 or D_2 gas were stored in the reservoir chamber in advance, then H_2 or D_2 gas was introduced into the RC by opening the super needle valve. A 1L reservoir chamber for H_2 gas storage and a 2L chamber for D_2 gas were used.

Even at room temperature, H_2 or D_2 gas absorption and heat generation was observed in the case of using Pd in the nano-material. After that, we applied electric power to the heaters located at inside and outer-surface of the RC to increase sample temperature. Data of

temperatures, pressures, voltages, currents and a flow rates was logged during experiments. Based on the data, we estimated H or D absorption rate and excess heat generation from the samples. Blank runs to obtain the heat recovery rate of the experimental apparatus were performed using 1mm diameter and 1,300g weight ZrO_2 beads in the RC before or/and after foreground runs. Typical weight of PNZ and CNZ samples were 100g.

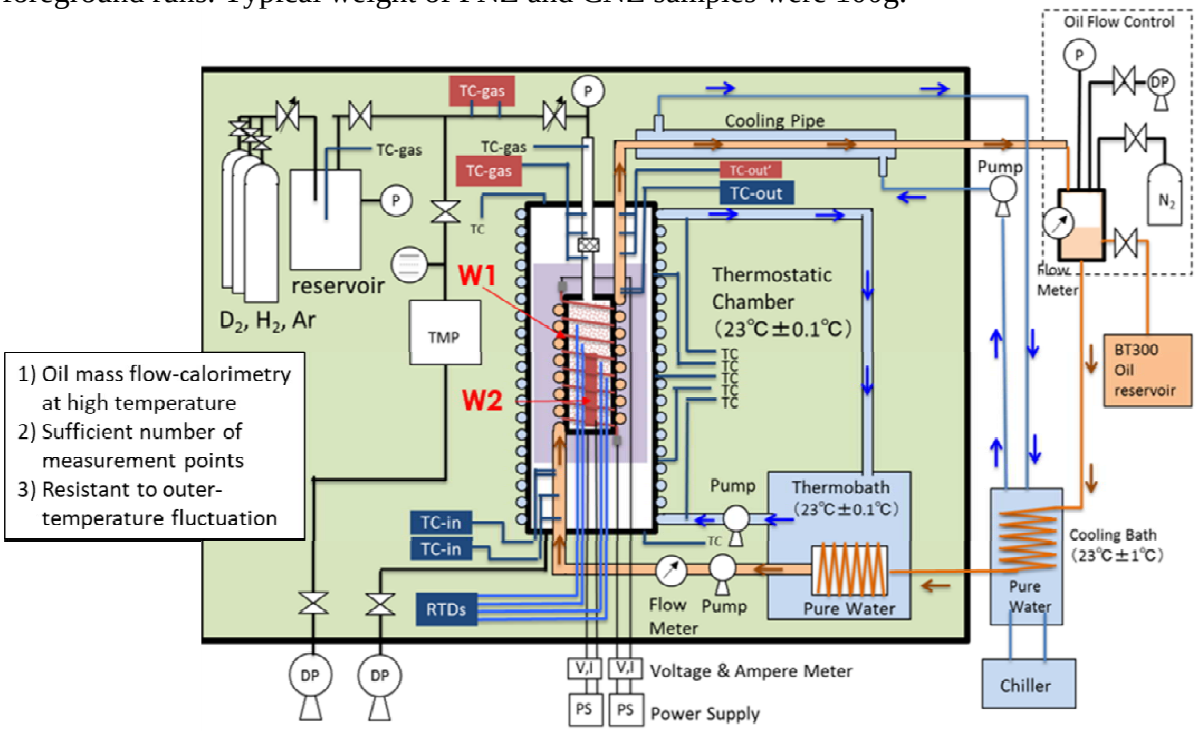

Figure 1. Schematic of Experimental Set-up

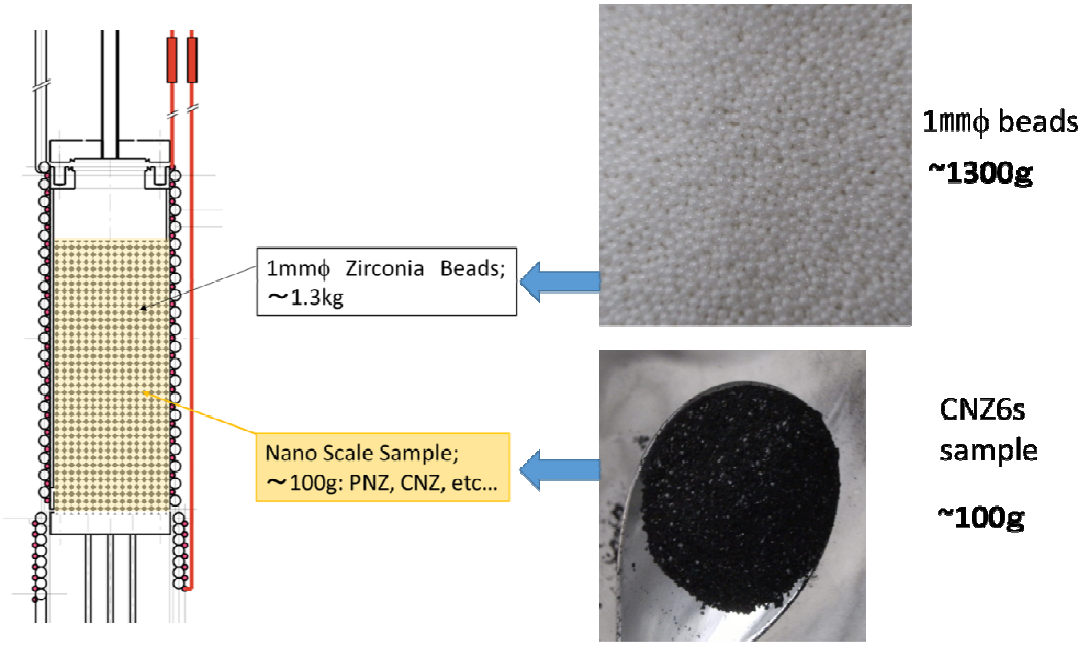

Figure 2. **Load Nano-Scale Material into Reaction Chamber**

Thermostatic chamber

Main experimental setup

Figure 3. Photos of Experimental Set-up

3. Results and Discussion

3.1. Heat Analysis and its Error Estimation

Heat analysis of this system is based on the equation:

$$\eta Q = F_R \cdot \rho(T_{ave}) \cdot C(T_{ave}) \cdot (T_{out} - T_{in}) \quad (1)$$

where η is the heat recover rate, Q is the heat release rate, F_R is oil flow rate, $\rho(T_{ave})$ is the oil density as a function of temperature, $C(T_{ave})$ is heat capacity, T_{out} and T_{in} is the outlet and inlet temperatures of the coolant oil, respectively. Physical data of $\rho(T)$ and $C(T)$ of the coolant oil are already known. As temperature dependence of $\rho(T)$ and $C(T)$ is linear, we can postulate that T_{ave} is equal to $(T_{out}+T_{in})/2$.

Q is expressed as

$$Q = W_1 + W_2 + H_{EX} \quad (2)$$

where W_1, W_2 and H_{EX} are the input power of heater 1, the input power of heater 2 and the excess heat power from the RC.

Based on these equations, η is determined as a function of (W_1+W_2) by a blank run because Q, F_R, $\rho(T_{ave,})$, $C(T_{ave})$ and $(T_{out}-T_{in})$ are obtained by experimental data. H_{EX} is calculated by a foreground run using the determined η.
We simplify equations (1) and (2) for experimental error estimation.

$$H_{EX} = \frac{F_R \cdot \rho \cdot C}{\eta} \Delta T - W \ ;$$
$$\Delta T = T_{out} - T_{in} \ , \ \ W = W_1 + W_2 \ .$$

Considering that experimental variables are F_R, ΔT and W, we can assume that error range of the calculated excess heat is the sum of fluctuations of oil flow rate, temperature difference and input electrical power.

$$\delta(H_{EX}) \approx \left|\delta(F_R)\right| \frac{\rho \cdot C \cdot \Delta T}{\eta} + \left|\delta(\Delta T)\right| \frac{F_R \cdot \rho \cdot C}{\eta} + \left|\delta(W)\right| \quad (3)$$

Actual experimental data shows that largest contribution to the error of H_{EX} is of the F_R term and W is most stable.

3.2. Summary of the Collaborative Research

Summary of the collaborative research is shown in the Table1 and Fig.4. Excess energy experiments were done using metal nanocomposite with H_2 or D_2 gas. Experiments using CNZ with H_2, PNZ with D_2, CNS with H_2 and PSn1(Pd/SiO_2) with D_2 were performed. Anomalous excess heat generations were observed for all the samples at elevated temperature (150℃-350℃), except for the Pd nanoparticles embedded in mesoporous SiO_2 (PSn1 and PSf1). The amount of anomalous heat generation per hydrogen atom ranged from 10eV/H or D to 100eV/H or D, which could not be explained by any known chemical process as shown in the Fig.3. No.15 and 16 experiments were performed to demonstrate reproducibility of this excess heat effect. Experiments in the yellow lines are described in this paper.

3.3. Comparison between Experimental Results at Tohoku University and those at Kobe University

As shown in Table 1, PNZ, CNZ and CNS metal nanocomposite samples showed anomalous energy generations that cannot be explained by known chemical reactions. On the contrary, Pd nano-particles expressed as PSf1 and PSn1 did not show any anomalous phenomena. These experimental results are supposed to indicate rough experimental reproducibility. For showing more confident reproducibility, we performed experiments at Kobe and Tohoku University using same PNZ ($Pd_{0.044}Ni_{0.31}Zr_{0.65}$) samples with D_2 gas.
Figure 5 shows the comparison of released heat between Kobe and Tohoku at room temperature. The released heat powers were calculated based on the difference between inlet and outlet coolant temperatures same as the other experiments at elevated temperature. The heat powers have two peaks, because fresh D_2 gas was resupplied to the RC after the initial absorption of D_2 gas. By the resupply the pressure of D_2 and absorption rate of D_2 into the PNZ ($Pd_{0.044}Ni_{0.31}Zr_{0.65}$) sample increased and enhanced the rate of heat release associated with absorption of D_2. Released excess enthalpies obtained at Kobe and Tohoku Universities are very close to each other as shown in Fig.5.

Table 1. Summary of Collaborative Research

#	Place	Sample Name	Composition	Gas	Temp	Max Power	Released Enthalpy
1	Kobe	PS3	Pd/SiO_2	D	200-300°C	~0	~0
2	Kobe	PNZ3	$PdNi_7Zr_{15}$-O_x	D	200-300°C	10W	7.7MJ/mol-D
3	Kobe	PNZ3r	PNZ3- re oxidized	H	200-300°C	8.0W	2.0MJ/mol-H
4	Kobe	CNZ5	$CuNi_7Zr_{15}$-O_x	H	200-300°C	3.3W	3.6MJ/mol-H
5	Tohoku	PNZ4s	$PdNi_7Zr_{15}$-O_x	D	160-300°C	3.3W	1.4MJ/mol-D
6	Tohoku	CNZ5s	$CuNi_7Zr_{15}$-O_x	H	160-250°C	5.0W	6.5MJ/mol-H
7	Kobe	PSf1	$Pd/SiO_{2\text{-covered}}$	D	200-300°C	~0	~0
8	Tohoku	PSn1	$Pd/meso\text{-}SiO_2$	D	200-300°C	~0	~0
9	Kobe	CNS3	$CuNi_{10}/SiO_2$	H	200-400°C	4.4W	67 MJ/mol-H
10	Tohoku	CNS3s	$CuNi_{10}/SiO_2$	H	150-300°C	4.2W	11MJ/mol-H
11	Kobe	PNZ5	$PdNi_7Zr_{15}$-O_x	D	250-350°C	4.2W	7.6MJ/mol-D
12	Tohoku	CNZ6s	$CuNi_7Zr_{15}$-O_x	H	150-300°C	2.5W	5.3MJ/mol-H
13	Kyushu	PNZ	$PdNi_7Zr_{15}$-O_x	H	RT-450°C	-	-
14	Kobe	PNZ6	$PdNi_{10}Zr_{20}$-O_x	D	250-350°C	25W	200MJ/mol-D
15	Kobe	PNZ7k	$PdNi_7Zr_{15}$-O_x	D	250-350°C	5.0W	3.4MJ/mol-D
16	Tohoku	PNZ7s	$PdNi_7Zr_{15}$-O_x	D	250-350°C	4.0W	3.0MJ/mol-D

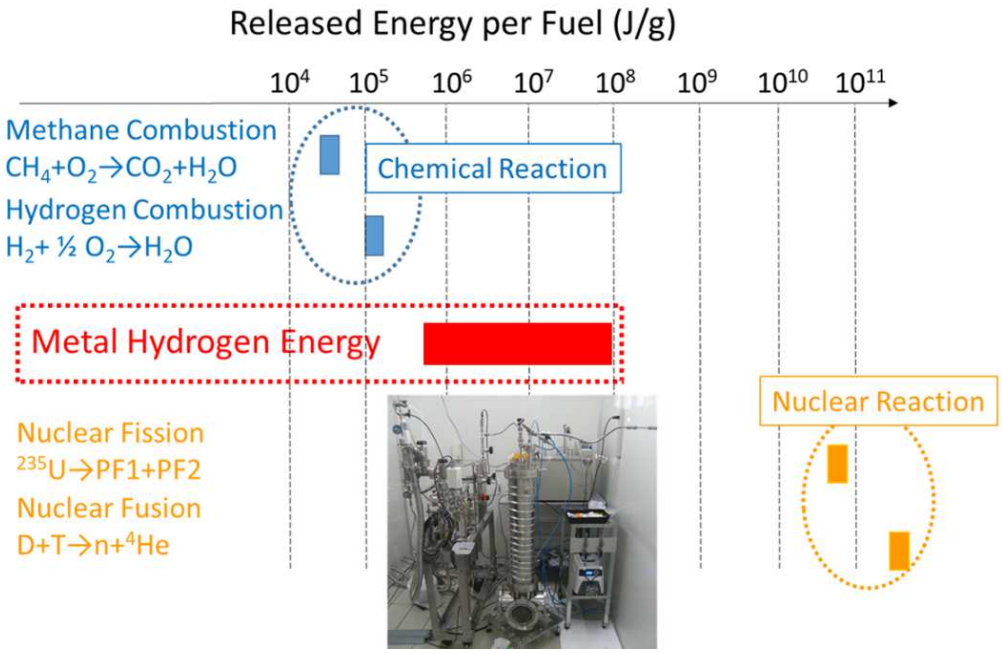

Figure 4. Released Energy per Fuel for the Collaborative Research

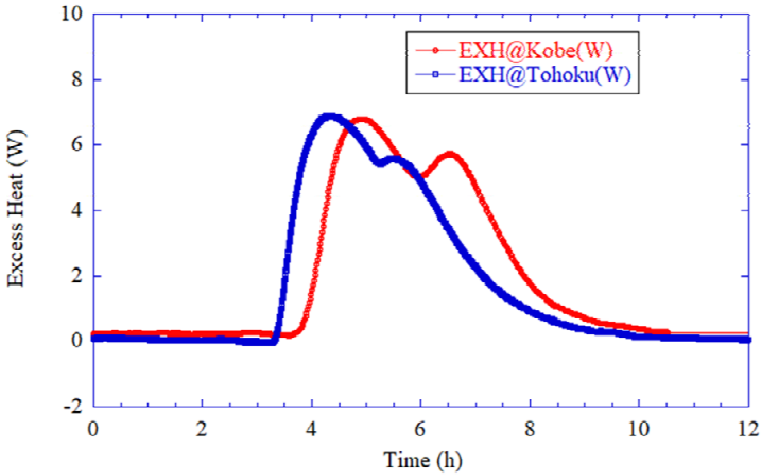

	Kobe	Tohoku
Released Enthalpy (KJ/mol-D)	53.7	50.9
Released Enthalpy (eV/D)	0.56	0.53

Figure 5. Comparison of Excess Heat between Kobe and Tohoku at Room Temperature

Figure 6 shows the comparison of excess heat power between Kobe and Tohoku Universities at elevated temperature. As the excess power obtained by the present method has certain correlation with temperature in the RC, we compared excess heat at similar RC temperatures. Same level excess powers were observed for similar RC temperature. These experimental results demonstrate that the similar level of excess power can be obtained if we use same metal nanocomposites and similar experimental set-ups.

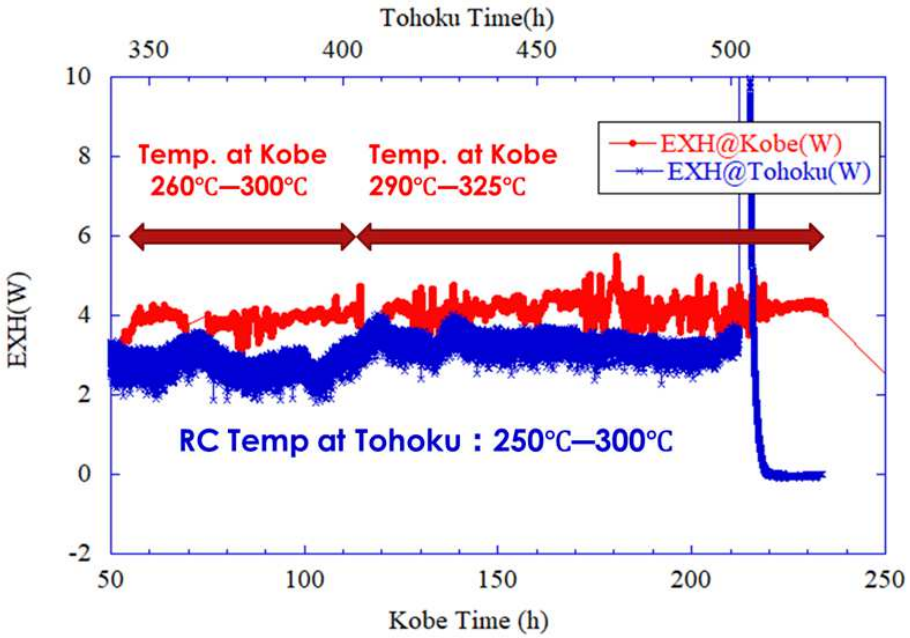

Figure 6. Comparison of Excess Heat between Kobe and Tohoku at Elevated Temperature

3.4. Coincident Increase Events of Chamber Pressure(Pr) and Upper Side Temperature

During the collaborative work, we observed very interesting coincident burst-like increase events of the pressure of reaction chamber and gas temperature for CNZ5s and CNZ6s experiments in the Table1, which suggested sudden energy releases in the reaction chamber. These events were observed for the two experiments.

Excess heat for CNZ5s calculated from the equations (1) and (2) is illustrated in Fig.7. About 4-5W and 2-4W were released during 80W and 134W heater power inputs, respectively. These excess powers are significantly larger than the estimated errors based on the equation (3). Sudden increase of excess power around 240h seemed to be induced by the increase of oil flow rate, but we have no exact explanation for it at present.

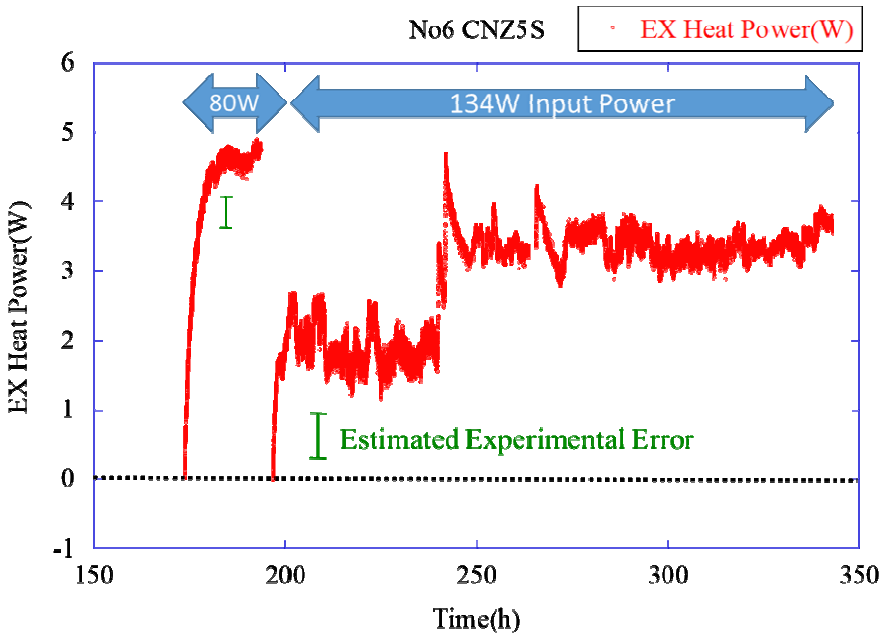

Figure 7. Excess Heat Generation (CNZ5s)

Burst-like coincident increase events of the pressure of RC(Pr) and the upper side pipe temperature(E2) at random timing were observed as shown in Fig.8. The pipe is connected to a hydrogen gas reservoir through a super needle flow regulator as shown in Fig.1. A pressure gauge is equipped with the pipe to measure the pressure of RC (Pr) and the surface temperature is monitored by thermocouple(E2). The pressure increase was about 0.02 or 0.03 MPa and the temperature increase ranged from 1℃ to 5℃. These were significant values and not explained by an outer noise as the other measurement data were stable and only Pr and E2 changed coincidently. The pipe temperature(E2) is supposed to be correspond to gas temperature in RC. We can assume that sudden energy releases induced coincident rising of gas temperature and pressure in RC.

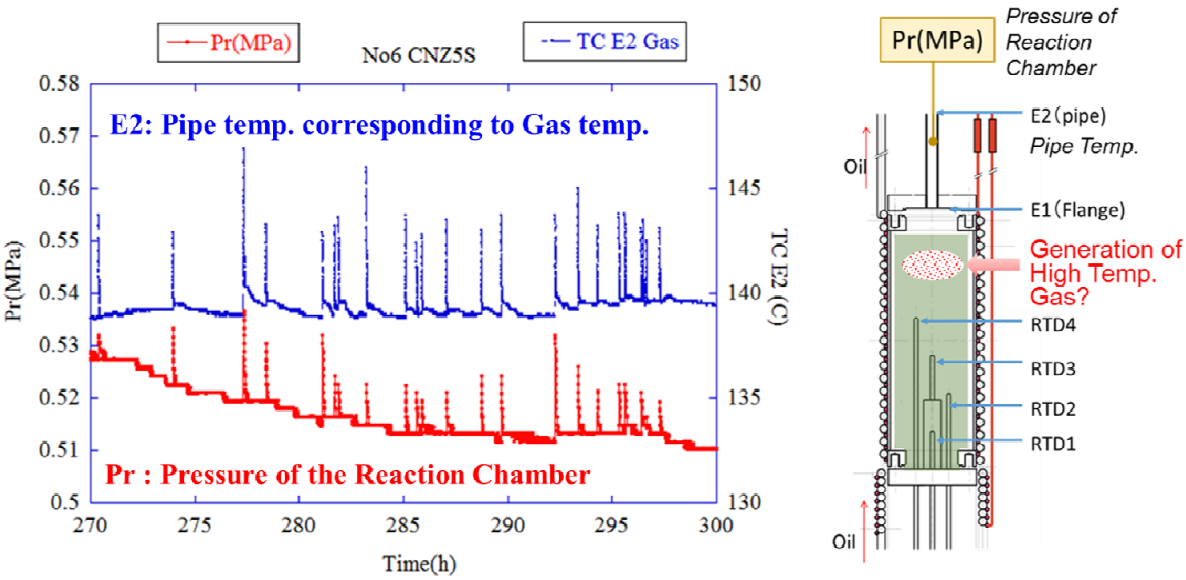

Figure 8. Burst-like Coincident Increase events of Chamber Pressure(Pr) and Upper Side Temperature(E2): CNZ5 s

The other experimental evidence that support the assumption of burst energy release is shown in Fig.9. After CNZ5s experiment, metal nanocomposite sample were sieved out to separate from ZrO_2 beads (1mmϕ). We found that some broken parts of ZrO_2 beads were mixed with the sample as shown in the right photo. ZrO_2 beads is very stiff material and difficult to be broken; it is used for crush to grind materials into a powder form. This experimental fact suggests that very large local stress, presumably due to heat burst, was loaded on ZrO_2 beads.

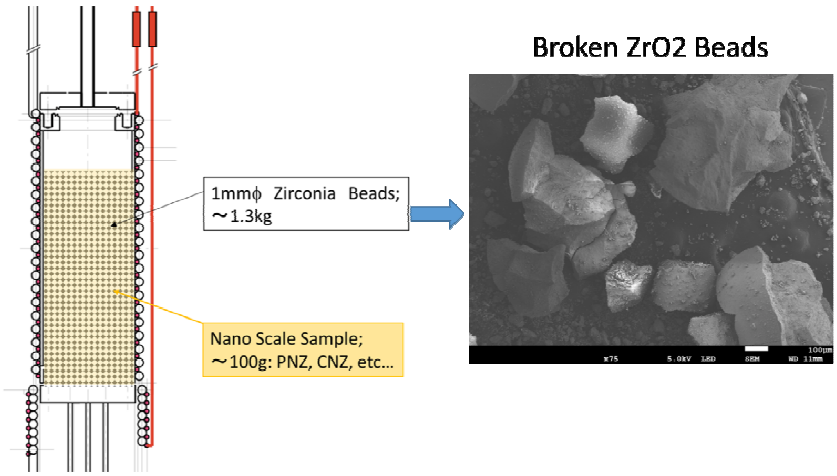

Figure 9. Broken ZrO2 beads after excess heat release

Figure 10 shows reproduced burst-like coincident increase events of chamber pressure(Pr) and upper side temperature(E2) for CNZ6s. Similar phenomena was reproduced by similar experimental conditions.

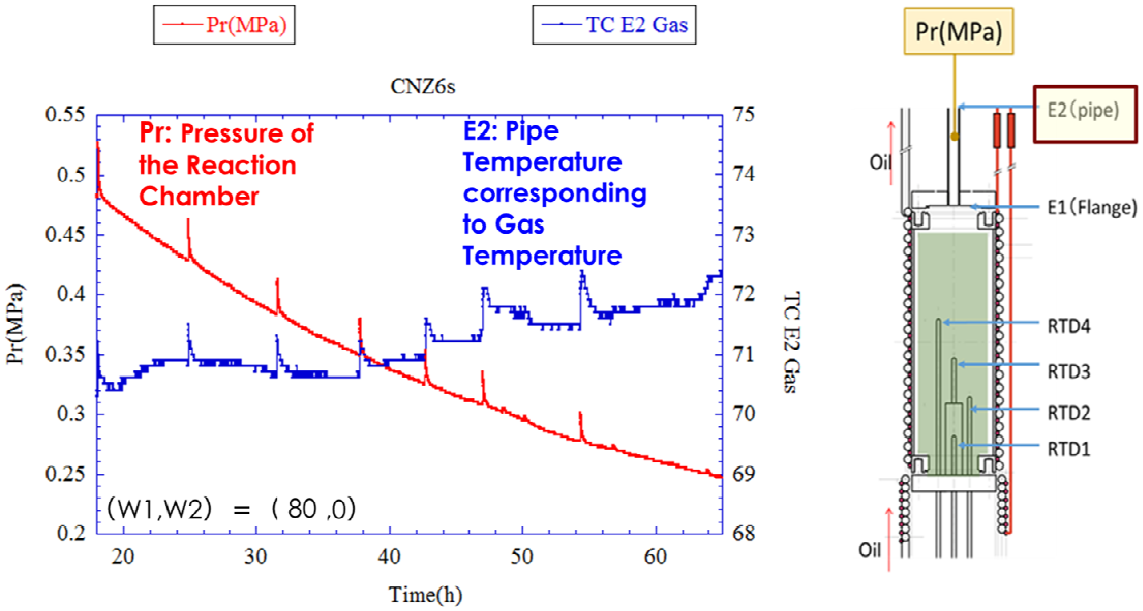

Figure 10. Burst-like Coincident Increase events of Chamber Pressure(Pr) and Upper Side Temperature(E2): CNZ6s

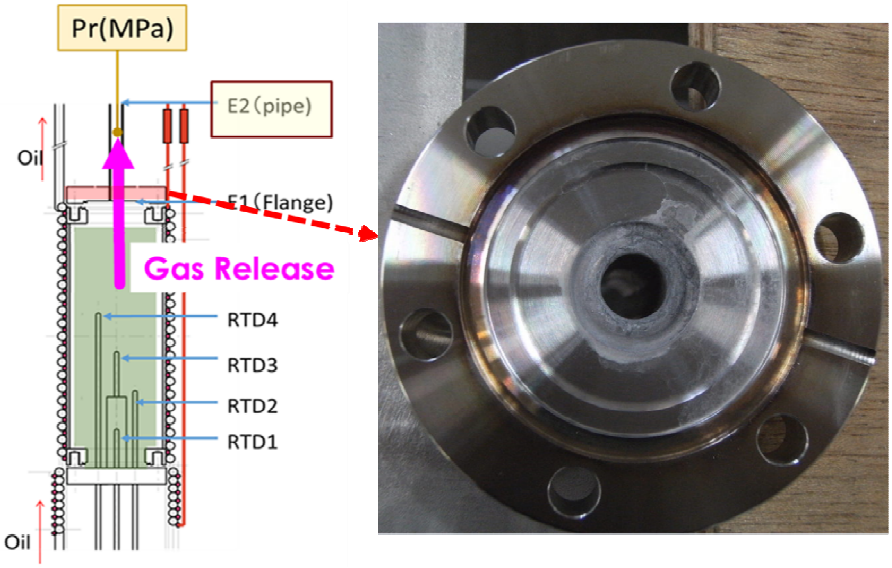

Figure 11. Photo of Upper Flange after CNZ6s experiment; Adhered Nano metal Particles?

In this experiment, an evidence that would support the assumption of burst energy release was obtained as shown in Fig.11. This is the photograph of the lower side surface of the upper flange after the CNZ6s experiment. Something adhered to the surface around the pipe of the upper flange. It would be possible to consider that CNZ6s nano-particles spouted out to the flange. This white substance was adhered firmly, we solved it by HNO_3. ICP-MS analysis will be applied to the solution. Anyway, it can be assumed that sudden energy releases induced coincident rising of gas temperature and pressure in RC.

4. Concluding Remarks

We discuss reproducibility on the anomalous excess heat phenomena with PNZ ($Pd_{0.044}Ni_{0.31}Zr_{0.65}$) and CNZ ($Cu_{0.044}Ni_{0.31}Zr_{0.65}$) samples. Two independent excess heat experiments at Kobe and Tohoku Universities using PNZ7k and PNZ7s were conducted, respectively. Qualitative reproducibility between Kobe and Tohoku experiments was good.

As to CNZ samples, we performed two experiments using CNZ5s and CNZ6s with the same composition at Tohoku University. Coincident burst-like increase events of the pressure of reaction chamber and gas temperature, which suggested sudden energy releases in the reaction chamber, were observed for both experiments using CNZ5s and CNZ6s samples. Furthermore, the other experimental evidences that support the assumption of burst energy release were obtained.

Acknowledgements

The authors would like to thank Mr. Y. Shibasaki (Tohoku U.) for his support for establishing experimental system. The authors would like to appreciate Technova Inc. for the corporation on building our experimental apparatus. We also acknowledge CLEAN PLANET Inc. for its significant contributions.

References

[1] A. Kitamura, A. Takahashi, R. Seto, Y. Fujita, A. Taniike and Y. Furuyama, “Brief summary of latest experimental results with a mass-flow calorimetry system for anomalous heat effect of nano-composite metals under D(H)-gas charging”, Current Science, vol. 108, no. 4, pp. 589-593, 2015.

[2] A. Kitamura, A. Takahashi, R. Seto, Y. Fujita, A. Taniike and Y. Furuyama, “Effect of Minority Atoms of Binary Ni-Based Nano-Composites on Anomalous Heat Evolution under Hydrogen Absorption”, J. Condensed Matter Nucl. Sci., **19** (2016) 1-10.

[3] A. Kitamura, E. F. Marano, A. Takahashi, R. Seto, T. Yokose, A. Taniike and Y. Furuyama, “Heat evolution from zirconia-supported Ni-based nano-composite samples under exposure to hydrogen isotope gas”, Proc. JCF16 (2016) 1-16.

[4] Y. Iwamura, J. Kasagi, H. Kikunaga, H. Yoshino, T. Itoh, M. Hattori and T. Mizuno, “The Launch of a New Plan on Condensed Matter Nuclear Science at Tohoku University”, J. Condensed Matter Nucl. Sci. 19 (2016) 119–126.

[5] T. Itoh, Y. Iwamura, J. Kasagi and H. Shishido, “Anomalous Excess Heat Generated by the Interaction between Nano-structured Pd/Ni surface and D_2/H_2 gas”, *J. Condensed Matter Nucl. Sci*. **24** (2017) 179–190.

[6] A. Kitamura, A. Takahashi, K. Takahashi, R. Seto, T. Hatano, Y. Iwamura, T. Itoh, J. Kasagi, M. Nakamura, M. Uchimura, H. Takahashi, S. Sumitomo, T. Hioki, T. Motohiro, Y. Furuyama, M.

Kishida, H. Matsune, “Excess heat evolution from nanocomposite samples under exposure to hydrogen isotope gases”, *International Journal of Hydrogen Energy* **43** (2018) 16187-16200.
[7] Y. Iwamura, T. Itoh, J. Kasagi, A. Kitamura, A. Takahashi and K. Takahashi, “Replication Experiments at Tohoku University on Anomalous Heat Generation Using Nickel-Based Binary Nanocomposites and Hydrogen Isotope Gas”, *J. Condensed Matter Nucl. Sci.* **24** (2017) 191–201.

In-situ XRD and XAFS Analyses for Metal Nanocomposites Used in Anomalous Heat Generation Experiments

Tatsumi Hioki[1], Kazuya Nakazawa[1], Akihisa Ichiki[1], Tomoyoshi Motohiro[1],
Akira Kitamura[2,5], Akito Takahashi[2], Koh Takahashi[2], Reiko Seto[2], Takeshi Hatano[2],
Yasuhiro Iwamura[3], Takehiko Itoh[3], Jirohta Kasagi[3],
Masanori Nakamura[4], Masanobu Uchimura[4], Hidekazu Takahashi[4], Shunsuke Sumitomo[4],
Yuichi Furuyama[5], Masahiro Kishida[6], Hideki Matsune[6]

[1] Green Mobility Research Institute, Institutes of Innovation for Future Society,
Nagoya University, 464-8603 Japan,
[2] Technova Inc., 100-0011 Japan,

[3] Research Center for Electron Photon Science, Tohoku University, 982-0826 Japan
[4] Research Division, Nissan Motor Co., Ltd., 237-8523 Japan,
[5] Graduate School of Maritime Sciences, Kobe University, 658-0022 Japan,
[6] Graduate School of Engineering, Kyushu University, 819-0395 Japan

E-mail: hioki@gvm.nagoya-u.ac.jp

Abstract Synchrotron Radiation XRD and XAFS analyses were performed for PNZ6 sample in which anomalous heat effect (AHE) was observed remarkably in a series of collaborative studies performed by 6 parties to which present authors belong. Structural changes of PNZ6 with increasing temperature up to 600℃ under hydrogen atmosphere were revealed. In the as-synthesized state, dominant crystalline phases were $NiZr_2$ and ZrO_2. Nano-scale Ni-Pd alloy particles were inferred to exist in the mixed matrix of $NiZr_2$ and ZrO_2. With increasing temperature under hydrogen atmosphere, hydride formation of $NiZr_2$ proceeded and $NiZr_2H_{\sim 5}$ was stable up to near 400℃. With further increase of temperature, a formation of ZrH_2 and $Zr_7Ni_{10}H_6$ accompanied by a decomposition of $NiZr_2H_{\sim 5}$ was observed. AHE may be enhanced by the mixed matrix of high hydrogen absorptive $NiZr_2$ and hydrogen inactive ZrO_2 in which nano-scale bimetallic Ni-Pd alloy particles are dispersed.

Index Terms – $NiZr_2$, ZrO_2, Ni-Pd alloy, Nano particles, Hydrogen, Anomalous heat effect, XRD, XAFS

I. INTRODUCTION

Anomalous heat effect (AHE) has recently been reported to be well reproducible in a series of collaborative experiments performed at elevated temperatures 200 ~ 350℃ using metal nanocomposites and hydrogen isotope gas [1 - 4]. Using an active material PNZ6 of 124g, a generation of excess heat exceeding 10W against external heater power of 90~160W was observed for more than 40days [5]. The accumulated amount of excess heat exceeded 45MJ, which could not be explained by any known chemical reactions [5].

In this paper, structural changes of PNZ6 with increasing temperature under hydrogen atmosphere were studied by in-situ XRD (X-ray diffraction) and XAFS (X ray absorption fine structure) analyses using facilities of Aichi Synchrotron Radiation Center. The analysed sample was a part of the material that was used for the heat evolution experiments at Kobe University [5]. The in-situ XRD analyses were performed at 15keV under hydrogen atmosphere of 0.4MPa, while raising temperature from room temperature (RT) to 600℃. XAFS profiles for K-edge Ni and K-edge Pd were taken under flowing hydrogen at 100

cc/min, while raising temperature from RT to 600 ℃. The obtained results were discussed in relation to AHE.

II. EXPERIMENTAL

II-1. Sample preparation

The PNZ6 sample was the one that was used in the heat evolution experiments performed at Kobe University. For the present study, a part of the sample before use was supplied by A. Kitamura. The detail of the preparation of PNZ6 is described elsewhere in this proceeding [5]. Briefly, PNZ6 was prepared by heat treating an amorphous alloy with a composition of $Pd_{0.032}Ni_{0.318}Zr_{0.65}$ at 450 ℃ for 60 h in air. With the partial-oxidation treatment, an increase in weight was observed and the composition was determined to be $Pd_{0.032}Ni_{0.318}Zr_{0.65}O_{0.24}$, assuming the increase in weight was totally due to oxidation of the sample.

II-2. XRD and XAFS measurements

The in-situ X-ray diffraction (XRD) experiments were performed using beam line BL5S2 of Aichi Synchrotron Radiation Center. A glass capillary tube of 0.3 mm in diameter and about 40 mm long was filled with a powder sample of partially-oxidized PNZ6 which was mixed with a small amount of BN powder. The inclusion of BN powder was to avoid breakage of the glass capillary tube owing to volume expansion of PNZ6 due to hydrogen absorption when the sample was exposed to hydrogen. The incident X-ray energy was 15 keV. The diffracted X-ray was detected with four flat 2D detectors (Dectris, PILATUS-100K). The data acquisition time was 10 ~ 20 min. The temperature of the sample was varied from room temperature to 600℃ by blowing hot N_2 gas against the capillary. The capillary tube was evacuated with a turbo molecular pump through a stainless pipe of 3/8 inch in diameter and about 5 m long. The attained vacuum at the sample capillary tube was probably in the order of 10 Pa. The capillary tube was pressurized up to 4 atm H_2 with a compact H_2 cylinder.

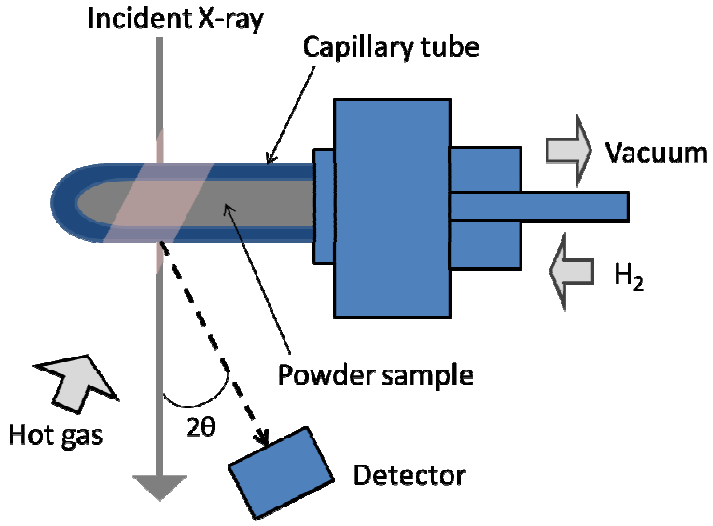

Fig.1 Configuration of in-situ XRD measurements.

In-situ XAFS measurements were performed for Ni and Pd K-edges using beamlines BL5S1 (Ni K-edge) and BL11S2 (Pd K-edge). All the XAFS measurements were conducted in a transmission mode, where three gas-filled ionization chambers were used in series to measure the absorption intensities of the sample and Ni or Pd foil as a reference standard. Pellet samples 0.5 mm thick, 7mm in diameter uniformly mixed with BN powder were set in a glass holder and put in a furnace capable of flowing hydrogen at 100 CC/min. The temperature of the furnace was able to be raised up to 1000℃.

III. RESULTS AND DISCUSSION

III-1. In-situ XRD analysis

Figure 2 shows schematically the experimental procedure of in-situ XRD measurements. The sample in the capillary tube was first evacuated at room temperature (RT, 25℃) for about 1h followed by vacuum baking at 120 ℃ for 2h. Then, the temperature of the sample was lowered to RT. XRD profiles ① and ② were taken in vacuum, at 120 ℃ during the baking process and at RT after the baking process, respectively. Then, the capillary tube was pressurized with hydrogen up to 4 atm H_2 and the pressure was kept at RT for about 0.5 h and then the XRD profile ③ was taken. XRD profiles ① and ② were completely overlapped. In Fig. 3, profile ② is shown.

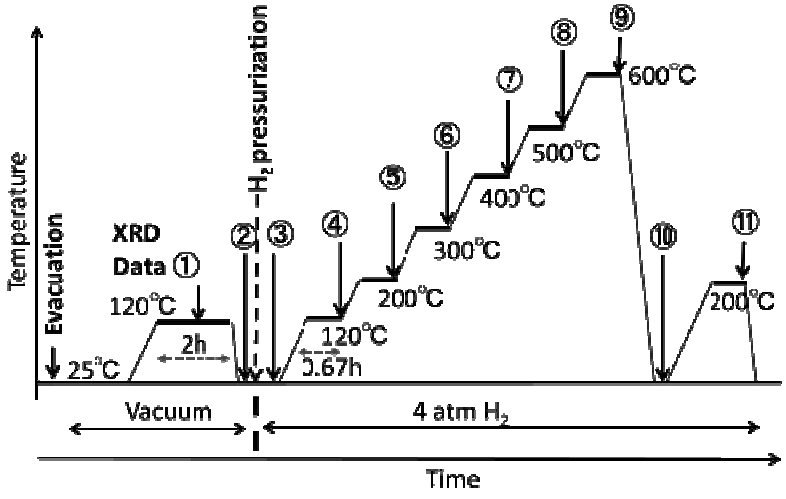

Fig.2 Procedure of in-situ XRD measurements. Circled number show the condition under which XRD data was taken.

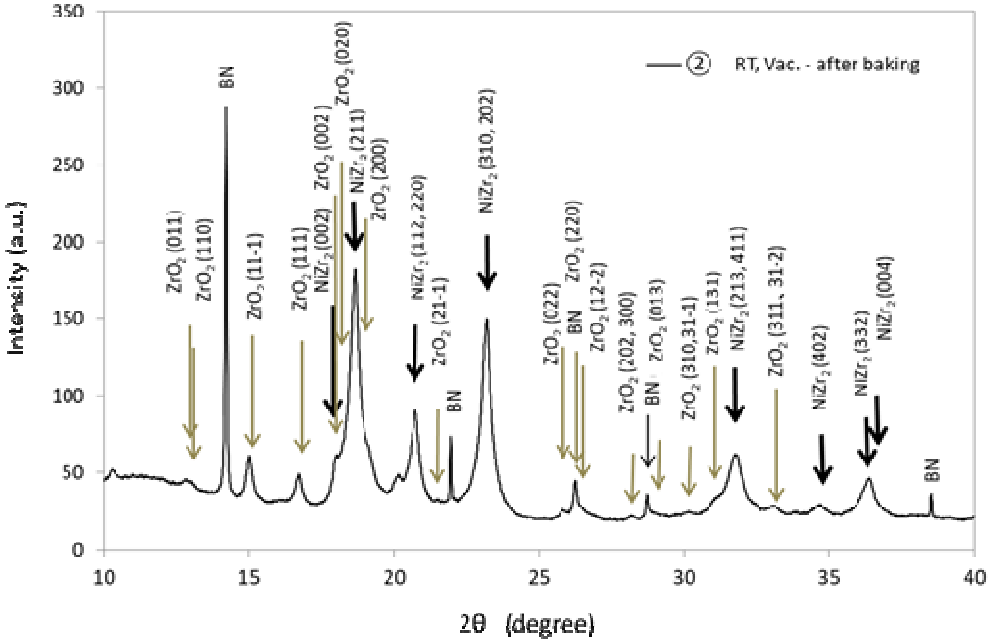

Fig.3 XRD spectrum ② for partially-oxidized PNZ6 taken in vacuum at RT after vacuum-baking at 120℃ for 1h.

It is seen that PNZ6 is dominantly composed of intermetallic compound $NiZr_2$ and monoclinic ZrO_2 as its initial state or in the state just after partial oxidation treatment. If Zr element is preferentially oxidized in the partial oxidation treatment, it is assumed that

$$Pd_{0.032}Ni_{0.318}Zr_{0.65}O_{0.24} = 0.265(Ni_{0.91}Pd_{0.09}Zr_2) + 0.12ZrO_2 + 0.085Ni_{0.91}Pd_{0.09} \quad (1)$$

In Fig.3, the XRD intensity from $NiZr_2$ is much larger than that from ZrO_2. Therefore, chemical equation (1) is assumed to be approximately valid. In Fig.3, however, no peaks from the third component in eq. (1) are seen. The third component is considered as nano-scale Ni-Pd alloy particles dispersed in the mixed matrix of $Ni_{0.91}Pd_{0.09}Zr_2$ and ZrO_2. XRD peaks from the nano-scale Ni-Pd alloy particles are expected hard to detect because of the line broadening for nano-scale particles. The line width for the peaks from $NiZr_2$ and ZrO_2 are much larger than that from BN. The crystalline size l was estimated to be 11 nm for $NiZr_2$ with $NiZr_2$ (211) and 16 nm for ZrO_2 with ZrO_2 (111), respectively, using Scherrer's equation,

$$l = 0.9\,\lambda / B\cos\theta \quad (2)$$

where, l is the grain size, λ the wave length of the incident X-ray, B the full width at half maximum of the peak, and θthe center angle of the peak.

The grain sizes of the $NiZr_2$ and ZrO_2 are significantly small and this fact may contribute to enhance kinematics of hydrogen absorption and desorption of the nano-composite sample.

Figure 4 compares the XRD data ②～⑪ taken according to the procedure of Fig.2.

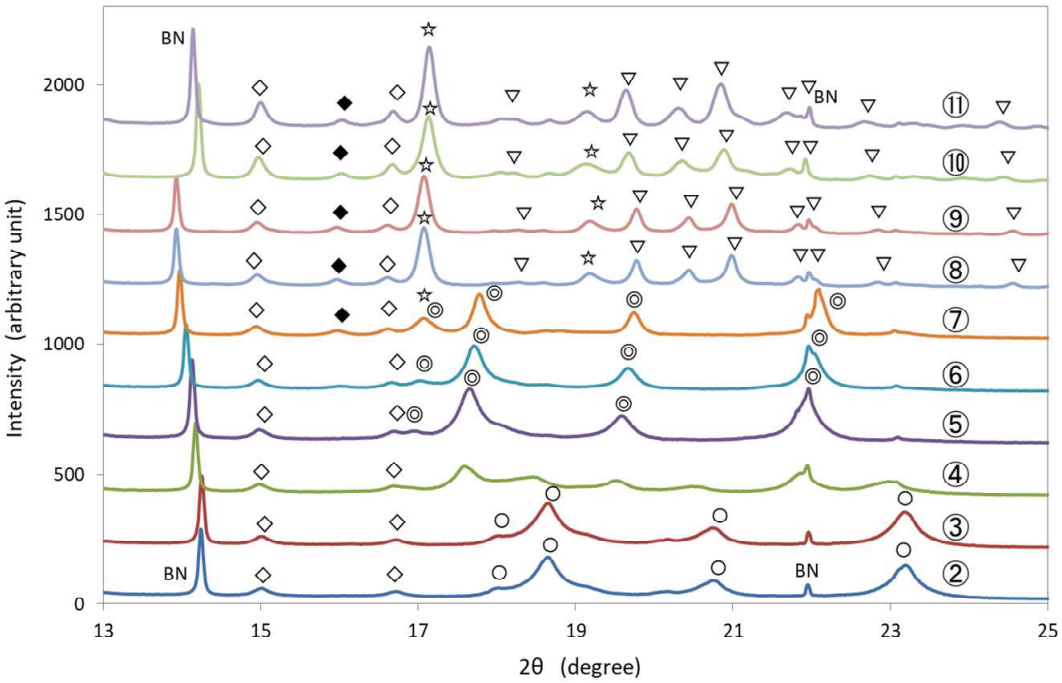

Fig.4 Variation of XRD profiles for PNZ6 with increasing temperature in 4 atm H_2. The circled number is the same with that shown in Fig.2, indicating the procedure of taking the in-situ XRD data.
○ ; $NiZr_2$, ◇ ; ZrO_2 (monoclinic), BN; Boron Nitride, ◎$NiZr_2H_{\sim 5}$, ☆ ; ZrH_2, ◆ ; ZrO_2 (tetragonal), ▽ ; $Zr_7Ni_{10}H_6$

As seen in Fig.4, the profiles ② and ③ are almost the same, indicating that the sample does not absorb hydrogen at room temperature. This was contrary to the heat evolution experiments performed at Kobe University, where PNZ6 absorbed hydrogen at room temperature. The difference is probably due to the activation treatment for hydrogen absorption. In the Kobe experiments, the sample was first heated up to 300℃ and evacuated for about 30 h up to 1.3×10^{-4} Pa. On the contrary, in the present study, the sample in the glass capillary was first heated to 120 ℃ and evacuated to ~10 Pa for ~2 h as an activation treatment. The activation treatment in the present in-situ XRD study was not enough for the sample to absorb hydrogen at room temperature. However, when the temperature was raised to 120℃, the XRD peaks from $NiZr_2$ sifted to lower angles indicating that the sample absorbed hydrogen.

Figure 5 compares the XRD profile ④ to ② in an enlarged scale. When the temperature was increased from RT to 120 ℃ under 4atm H_2, the $NiZr_2$ (211) peak at RT shifted to lower angle and split into two peaks. Similar behaviour was seen for the peaks $NiZr_2$ (112, 220) and $NiZr_2$ (310, 202). The peak shifts to lower angle are due to absorption of hydrogen by $NiZr_2$. The splitting of the $NiZr_2$ peaks indicates that there are two hydride phases $NiZr_2H_x$ ($x = x_{low}, x_{high}$). Table 1 shows that the average lattice expansions with hydrogen absorption are 1.1± 0.10 % and 6.1 ± 0.2 % for $NiZr_2Hx_{low}$ and $NiZr_2Hx_{high}$ phases, respectively.

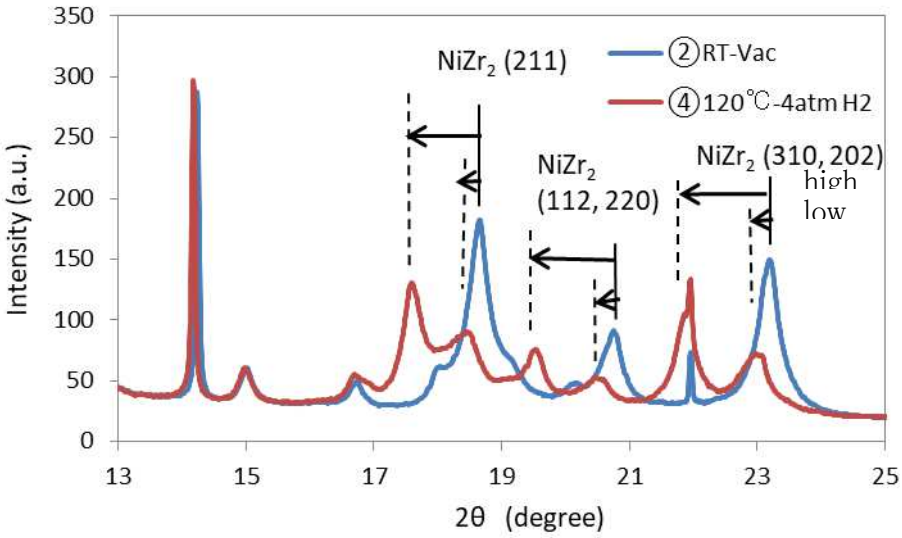

Fig.5 Comparison of XRD profiles for PNZ6; blue at RT under vacuum and red at 120 ℃ under 4 atm H_2. Each $NiZr_2$ peak at RT shifts to lower angles with a low- shift value and a high- shift value.

Table 1 XRD peak angles (2 θ), lattice spacings (d) for $NiZr_2$ at RT under vacuum and at 120℃ under 4atm H_2, and lattice expansion for $NiZr_2H_{Xlow}$ and $NiZr_2H_{Xhigh}$.

XRD peak	②RT-Vac		④120 ℃-4atm H_2			lattice expansion (%)
	2 θ (degree)	d (nm)		2 θ (degree)	d (nm)	
$NiZr_2$ (211)	18.64	0.2555	low	18.45	0.2581	1.00
			high	17.58	0.2707	5.96
$NiZr_2$ (112, 220)	20.74	0.2298	low	20.49	0.2326	1.22
			high	19.51	0.2442	6.25
$NiZr_2$ (310, 202)	23.19	0.2058	low	22.93	0.2081	1.13
			high	21.85	0.2183	6.07

As seen in Fig.4, when the temperature was raised to 200 ℃, only the high hydride phase $NiZr_2H_{Xhigh}$ was observed. According to references [6, 7], X_{high} is likely to be about 5.0. From the value of XRD shift, X_{low} is probably about 1. $NiZrH_{\sim 1}$ seems to be a hydride phase appearing only in the initial stage of hydride formation of $NiZr_2$. It was found that the higher hydride phase $NiZr_2H_{\sim 5}$ is stable between 200 and 300 ℃. At 400 ℃, it seems that ZrH_2 and tetragonal ZrO_2 starts to form, although the $NiZr_2H_{\sim 5}$ phase is still the major component. At 500℃ and 600℃, the $NiZr_2H_{\sim 5}$ phase disappears and ZrH_2 and $Zr_7Ni_{10}H_6$ [8] are formed.

The temperature range, where AHE for PNZ6 is remarkably observable, has been reported to be 200~350℃ [5]. It is noted in Fig.4 that in this temperature range, $NiZr_2H_{\sim 5}$ phase is

stable. It is also noted that once the $NiZr_2H_{\sim 5}$ phase was decomposed to form ZrH_2 and $Zr_7Ni_{10}H_6$, the $NiZr_2H_{\sim 5}$ phase never recovered even when the temperature was lowered down to RT in H_2 atmosphere. Therefore, it may be suggested that no AHE is observable if the heat evolution experiments are done at temperatures higher than ~ 400 ℃, where $NiZr_2H_{\sim 5}$ is decomposed.

III-2. In-situ XAFS analysis

In Fig. 6, Ni-K edge XAFS spectra are shown for PNZ6. The data was first taken for the sample at 25℃ in air. Then the sample was exposed to flowing H_2 for about 30 min. The data for this condition is shown in Fig.6 as PNZ6 25℃. The spectra was same with the first one, and was unchanged up to 100℃ in flowing H_2, as shown in Fig.6. Compared to the reference spectra, PNZ6 is much closer to metallic Ni. It is therefore suggested that Ni in PNZ6 is not oxidized by the partial oxidation treatment. It is also noted in Fig.6 that PNZ6 has a marked pre-edge peak arising probably from the structure of intermetallic compound $NiZr_2$.

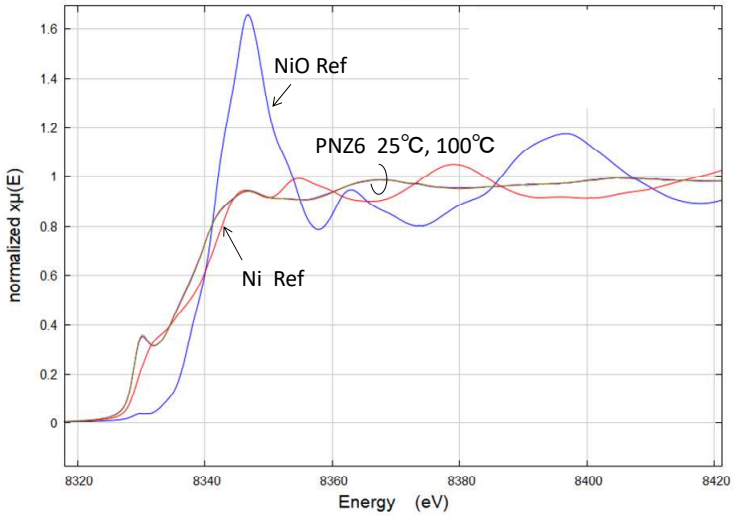

Fig. 6 Ni-K edge XAFS spectra for PNZ6 at 25℃ and 100℃ in H_2 flow.
(Reference spectra are shown for NiO and Ni in ambient atmosphere)

Figure 7 shows the temperature variation of XAFS spectra around the pre-edge region. The marked pre-edge peak seen at temperatures lower than 100℃ was lowered remarkably in the temperature region 200 ~ 300 ℃, probably corresponding to hydrogen uptake into $NiZr_2$ around this temperature region as shown in the above XRD analysis. As the temperature was further increased, the spectra became closer to that for Ni reference. These variations seem to correspond to the decomposition of $NiZr_2H_{\sim 5}$ and formation of $Ni_{10}Zr_7H_6$ and ZrH_2.

To know about the chemical state of Pd in PNZ6, Pd K-edge XAFS spectra were taken.

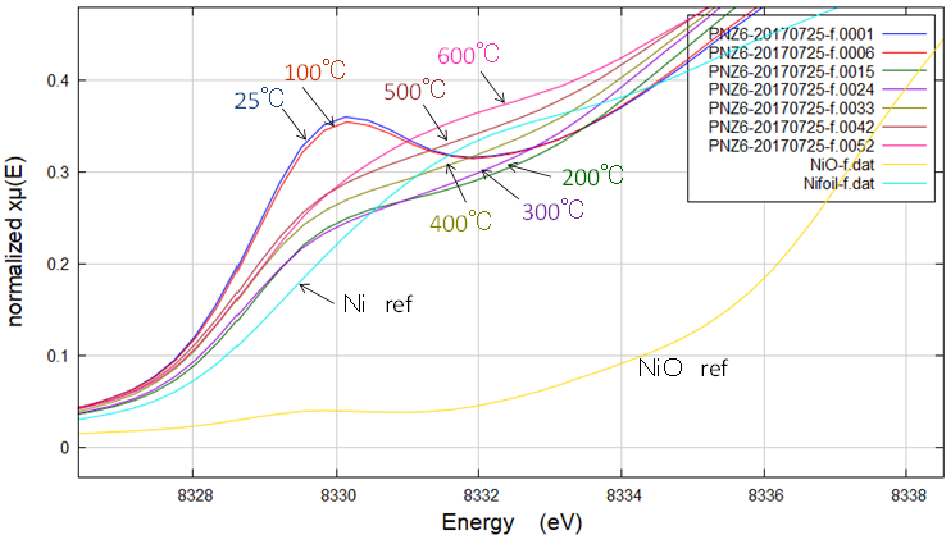

Fig.7 Variation of Ni-K edge XANES spectra with temperature for PNZ6 under flowing H_2

Figure 8 shows the spectra at 25℃ in air compared to references of PdO and Pd. It is evident that Pd is not oxidized in the as synthesized state. Therefore, it is suggested that the chemical state of Pd in as-synthesized PNZ6 is (i) Ni-Pd alloy particles dispersed in ZrO2, (ii) inter metallic compound $(Ni_{0.91}Pd_{0.09})Zr_2$ and/or both.

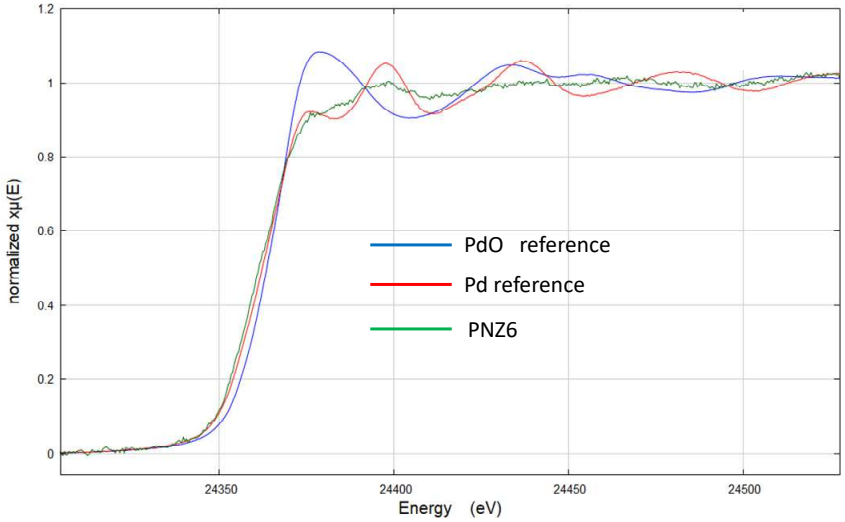

Fig.8 Pd-K edge XAFS spectra for PNZ6 at 25℃ in air.

Figure 9 shows the variation of the XAFS spectra with temperature under flowing H_2. The spectra were not changed significantly up to 300℃. As seen in Fig.8 and Fig.9, the amplitude of EXAFS oscillation was very weak for Pd-K edge in PNZ6, resulting in the little variation of the spectra with increasing temperature under H_2 flow. This is in contrast to the

case of nano-sized-Pd/ZrO_2 composite [9], in which XAFS spectra of Pd K-edge varied depending on atmospheric condition, i.e. under H_2 or under vacuum. For PNZ6, Pd is alloyed with Ni. It seems that nanoscale particles of Ni rich Ni-Pd alloy hardly absorb hydrogen and Pd K-edge XAFS spectra are expected insensitive to hydrogen.

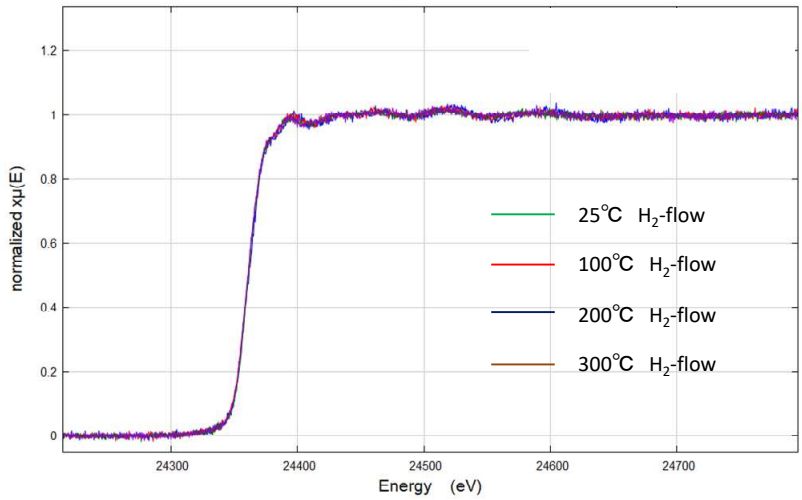

Fig. 9 Pd K-edge XAFS spectra for PNZ6 at different temperatures in flowing H_2

IV. SUMMARY AND CONCLUDING REMARKS

XRD and XAFS analyses were carried out for the PNZ6 sample that exhibited most remarkable AHE in a series of collaborative experiments performed by the 6 parties. With the XRD analyses, following results were obtained: i) before hydrogen exposure, PNZ6 dominantly consisted of $NiZr_2$ and ZrO_2, ii) after hydrogen exposure, at 120℃ the peak from $NiZr_2$ was divided into two peaks, suggesting the formation of two hydride phases $NiZr_2H_{\sim1}$ and $NiZr_2H_{\sim5}$, iii) at 200 ~ 300 ℃, PNZ6 dominantly consisted of $NiZr_2H_{\sim5}$ and ZrO_2, iv) at 400℃, the formation of ZrH_2 started, v) at temperatures higher than 500℃, ZrH_2 and $Ni_{10}Zr_7H_6$ formed with a decomposition of $NiZr_2$. The XAFS data were qualitatively consistent with the XRD results. From the Pd- and Ni- K edge XAFS data, it was suggested that nano-scale metallic Pd-Ni alloy particles exist in mixed matrix of $NiZr_2$ and ZrO_2 even just after the partial oxidation treatment. It was inferred that nano-scale Ni-Pd alloy particles enhance kinematics of hydrogen absorption and desorption of $NiZr_2$ which have high hydrogen storage capacity. The remarkable AHE observed in PNZ6 may be correlated with such complex structure of nanoscale Ni-Pd alloy particles dispersed in mixed matrix of highly hydrogen absorptive $NiZr_2$ and hydrogen inactive ZrO_2.

Acknowledgements

We greatly thank Drs S. Towata and H. Azuma of Aichi SR Center for supporting XRD and XAFS analyses. We also thank staff members of BL5S2, BL5S1, and BL11S2 for XRD and XAFS measurements.

Reference

[1] A. Kitamura et al., Proc. JCF**17** (2017) 1-14.
[2] Y. Iwamura et al., Proc. JCF**17** (2017) 15-17.

[3] A. Kitamura et al., J. Condensed Matter Nucl. Sci. **24** (2017) 202-213.
[4] Y. Iwamura et al., J. Condensed Matter Nucl. Sci. **24** (2017) 191-201.
[5] A. Kitamura et al., Proc. JCF**18** (2018) to be published.
[6] F. Aubertin and S.J.Campbell, Hyperfine Interactions **54** (1990) 767-774.
[7] M.M. Elcombe et al., J. Alloys & Compounds **232** (1996) 174–179.
[8] H.T. Takeshita et al., J. Alloys & Compounds **376** (2004) 268–274.
[9] Y. Arachi et al., Solid State Ionics **177** (2006) 1861-1864.

Nuclear Fusion Mechanism in Metal Crystals

Kazuo Ooyama (Ooyama Power Inc.)
k1@ ooyama-power.com

Abstract

In this paper, the transmutation mechanism estimated from past experimental results is written.

The author selected "Transmutation Experiments induced by Deuterium Permeation" [1] by Iwamura et al. as an experiment in which a nuclear reaction has definitely occurred and believed this experiment and "Excessive Heat generation of the Pd cathode" by M. Fleichmann and S. Ponds[2] had a common mechanism and studied the fusion mechanism in metal crystal. This is because it is difficult to think that two different mechanisms unknown to mankind exist in similar experiments.

In these experiments, Pd is divided into two phases, the α phase with low deuterium concentration and the α 'phase with high deuterium concentration. At first glance it seems static, but due to changes in concentration distribution and temperature distribution phase transformation occurs in crystal grain unit, internal stress is generated. For this reason, edge dislocation that always exist in the crystal moves, abnormal accumulation of D nuclei that does not occur in the static state occurs, and D-D fusion due to the tunnel effect occurs. When the generated ion beam reaches the α phase, it is led to the D nucleus of the interstitial atom by the channeling phenomenon, and it is made into an ion beam. The generated D ion beam is guided to the nucleus of another interstitial atom, and a nuclear reaction occurs.

Furthermore, the author constructed “Binary nucleus model” that realizes a nuclear reaction that does not generate radiation with high penetrating power. The characteristics of nuclear fusion by this model are in good agreement with the nuclear fusion probability increase phenomena in the metal whose reason was unknown.

With these synergies, the nuclear fusion is continued, ^{4}He are generated, ^{6}Li are generated, and an α beams are generated by the 2α reaction. These chain reactions generate excessive heat.

After the α beam and the nuclear that will undergo transmutation form a binary star nucleus, nuclear fusion is caused to generate transmutation nuclei.

Index Terms--- Nuclear fusion, Reaction mechanism, Chain reaction, Crystal, Metal, Channeling, Palladium, Deuterium, Ion beam, Binary nucleus, Crystal lattice, Triple nucleus fusion, Excessive heat, Transmutation, ^{6}Li, 2α reaction

1. Introduction: Jigsaw puzzle made by God

In recent years the price of fossil fuels has increased, global warming is also a problem, and whether we humanity can use nuclear fusion energy or not is the urgent task of all human beings. We humanity have not been able to elucidate the theory of the excessive heat generation even though 29 years have passed since the announcement of "the Excessive Heat generation of the Pd cathode" by M. Fleichmann and S. Ponds in 1989[2]. Therefore, the existence of low temperature nuclear fusion itself is denied, securing budget etc. becomes difficult, researchers are decreasing. Also, as time passes, wrong information gets mixed in, make it more difficult to pursue the theory.

As a reason why, the theory was not elucidated for a long time, the author considered that excessive heat generation is thought to be explained by a single phenomenon. Excessive heat generation is a complex mechanism, a sort of jigsaw puzzle God has given to mankind. God gave us the possibility, but he also set a time limit in the form of fading away from human memory over time.

First, I had to decide the policy to solve this jigsaw puzzle. I decided to consider the mechanism based on “Transmutation experiment by deuterium penetration into Pd multilayer film[1]” by Iwamura et al. I thought this report is extremely reliable because this report has a lot of information volume, such as identification of conversion elements and gamma ray peak of 511.5keV reported, and reported by Toyota Central Research Institute's replacement test report[3]. The sample in this experiment uses multilayers of Pd and Ca, but the basic is a combination of Pd bulk and deuterium as in the experiment of M. Fleichmann and S. Ponds[2]. So, I decided to think that common mechanisms worked in these experiments.

Next, I had to grasp the whole image of the jigsaw puzzle. Since transmutations confirmed by transmutation experiments have been confirmed to increase by an integer multiple of the same amount of nucleon as ^{4}He, it is natural to think that α nuclei fusion continuously. However, energy of about 1MeV is necessary for atomic nucleus of atomic number 55 of Cs to nuclear fusion with ^{4}He. In addition, the reaction rate from ^{133}Cs to ^{141}Pr is as high as 62% on average at three points of 80°C around 200kPa. I thought that it is necessary for active reaction of nuclear fusion chain reaction to occur in the neighborhood in order to react with high probability like this. It is possible to explain the results of both experiments if it is thought that a unique nuclear fusion mechanism exists and chain reaction of nuclear fusion is occurring in the metal. I imagined that a nuclear fusion chain reaction occurred inside the metal.

However, in order for chain reaction to take place, it is necessary that a starting nuclear fusion reaction occurs. Since the distance between the D-D nuclei in Pd does not approach the D_2 molecule in the gas phase in the static state, it is the theory that there is no possibility of a

D-D fusion due to the tunnel effect. Also, the reaction cross section is lacking by orders of magnitude to cause fusion chain reaction. No matter how much I thought, it seemed to me that the pieces filling up the hole in this whole picture were missing.

However, I thought of other various mechanisms, but I could not find a mechanism to explain the two experiments. So, I decided to believe that there was a piece to fill the hole and look for a missing piece. I thought that nuclear fusion as a starting point would occur by creating a dynamic state by the movement of dislocations in metal crystals. When I thought about how to find the remaining piece, I noticed that We humanity had a lot of knowledge as a combination of only two elements of metal and ion beam. Therefore, as a result of investigating the phenomena related to metal and ion beam, I arrived at the channeling phenomenon due to the crystal structure and the phenomenon that nuclear fusion probability increases within the metal. The latter phenomenon affirmed my proposed binary nuclear model.

I consider the mechanism of these phenomena and constructed unique nuclear fusion mechanism in metal crystals including binary nuclear model. If this nuclear fusion mechanism in metal crystals is correct, it should be able to explain the excessive heat generation and the results of transmutation experiments[1].

2. Ignition reaction

1) Excessive Accumulation of D nucleus by movement of edge dislocations

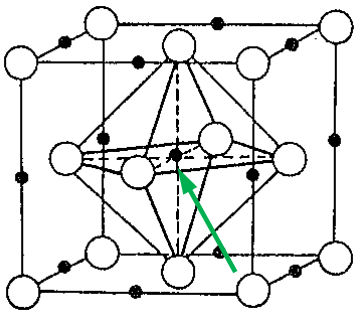

Fig.1 Pd crystal structure (fcc).

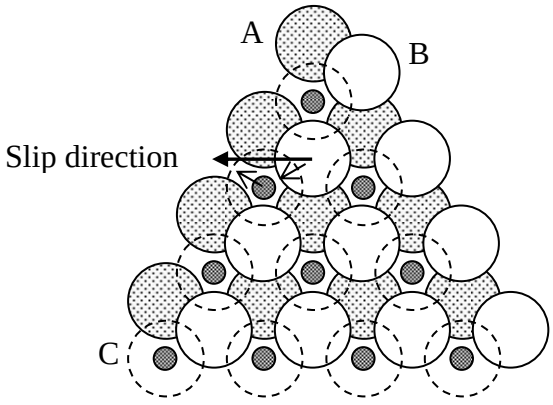

Fig.2 Pd closest packing surfaces.

Metal Pd has the close-packed structure of fcc (face-centered cubic lattice) drawn in Fig. 1, and deuterium D indicated by black circle enters its O site. Fig.2 shows the drawing from the [11-1] direction of the green arrow in Fig.1 with the close-packed planes overlapping. On the close-packing surface, Pd atoms are aligned in a honeycomb so as to be densest. The stippled circles show the Pd atoms at the back of the D nucleus in the center of fcc. This layer is the

first layer and the Pd position of this layer is A. White circles represent the Pd atoms of the second layer on top of the first layer and are aligned a honeycomb at the B position evenly on top of the three Pd atoms of the first layer. The circles drawn transparently by the dotted lines represent the Pd atoms of the third layer further above the second layer and likewise aligned in a honeycomb manner at the position of C evenly on three of the Pd atoms of the second layer. Since Pd atoms are again placed on the position of A on the third layer, a laminated structure is repeated with A - B - C - A - B - C.

In Fig.2, only the D atoms between the first layer and the second layer are drawn with small black circles in the state where D atoms are in all the O sites. Therefore, both Fig.1 and Fig.2 show the state where the ratio of Pd and D atoms is 1: 1. Actually, since deuterium gas at 10 atmospheric pressure at 80°C contains only about 0.7 D atoms for Pd atom 1, it does not enter as much as in In Fig.2. Also, in Fig.2, the arrangement of Pd atoms in the ideal state fcc structure is shown, but in practical metals there are always some mismatches called crystal defect.

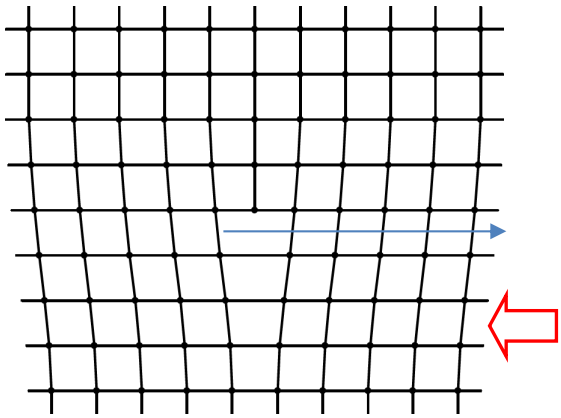

Fig.3 Edge dislocation.

One of the crystal defects is an edge dislocation in which the layer is locally increased or decreased by one. Fig.3 is a conceptual diagram showing commonly used edge dislocations. When such an edge dislocation is present, a portion that becomes sparse and a portion that becomes dense can be formed, so that D accumulates in a sparse portion. Since the dislocation is in an unstable state, when a light load is applied in the direction of the red arrow, the dislocation easily moves toward the blue arrow. The plane where the dislocations move in this way and the lattice constituent atoms move in the opposite direction is called the slip plane.

The close-packed surface also serves as a sliding surface when the crystal lattice of the fcc structure is deformed. When the metal receives a load, the entire crystal deforms as Pd atoms move on this sliding surface. The large arrow shown in Fig. 2 represents the sliding direction [1-10] of one of the Pd atoms at the B position contained in the (11-1) plane. However, rather

than moving one atom at a time to the next B position at a stroke, moving to the C position once as indicated by a small arrow once moves to the next B position has less distortion applied to its surroundings.

Fig.4 shows a state where one row of Pd atoms in the upper left corner of the second layer is moved from the B position to the C position as seen from the side which becomes sparse due to the edge dislocation. Since the Pd atoms in the layers above the second layer also move at the same time, the lower right side is A - B - C - A - B - C whereas the upper left side is A - C - A - B - C. Since the structure differs between the lower right and the upper left, the two-dot chain line indicating the boundary between them is the position of the edge dislocation. Fig.4 shows how D atoms accumulate in the sparse part of edge dislocations.

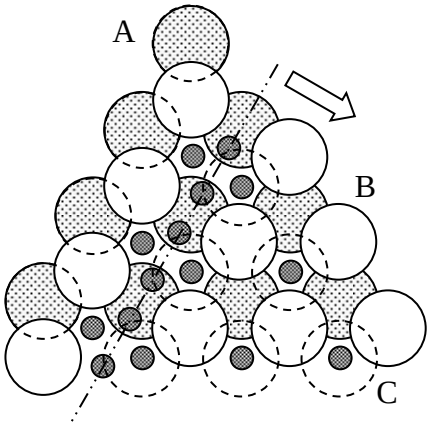

Fig. 4

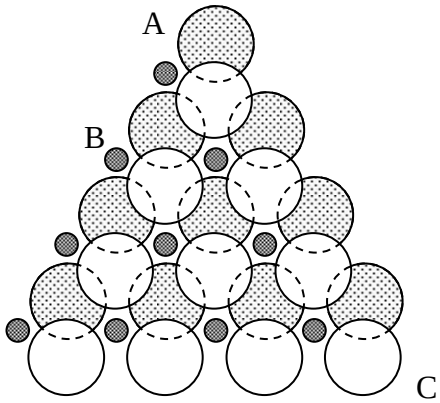

Fig. 5

Fig. 4 depicts a small part of the crystal to represent the dislocation structure, but if a number of edge dislocations are present in parallel in a vertical direction, the orientation of the crystal at the right and left of the edge dislocations Will tilt slightly. The crystal grain boundary can also be said to be a place where many dislocations gathered as the crystal orientation clearly changes. In other words, if the crystal grain size changes even if the sample does not see any movement, many dislocations are moving at the same time.

Fig.5 shows a state in which the edge dislocation moves in the direction of the arrow in Fig.4 and goes to the lower right and becomes a laminated structure of A - C - A - B - C. The D atoms between the first layer and the second layer enter the position B where Pd atoms are not present nearby. Furthermore, since the structure of A - C - A - B - C has a structure different from the ordinary structure, the bonding force between A - C becomes weak. Also, since the position of the adjacent atom separated by the dislocation is B, D atoms accumulate between A - C. When this layer containing D atoms is represented by (D), it can be expressed as A - (D) - C - A - B - C.

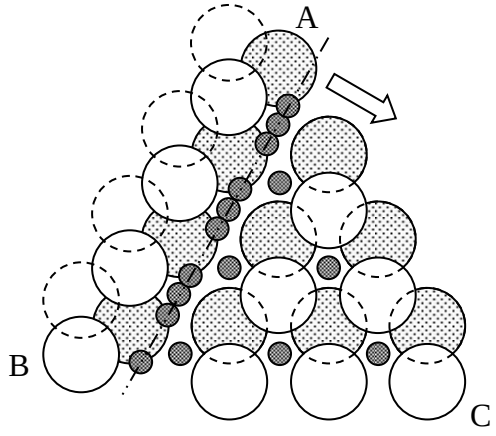

Fig. 6

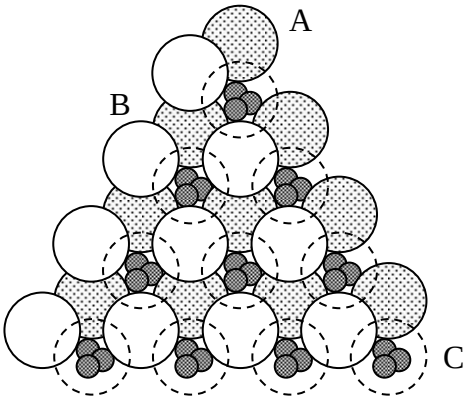

Fig. 7

Next, Fig. 6 depicts a state in which the edge dislocations moving the Pd atoms of the second layer from the C position to the original B position come from the same direction. Returning to the laminated structure of A - B - C - A - B - C, if this edge dislocation goes out to the lower right, as shown in Fig.7, it returns to the structure of Fig.2, and between Fig.4 and Fig.7, the layer above the second layer Pd atoms are moved by one in the [1-10] direction.

Let's follow the movement of D with these movement of dislocations. D atoms are accumulated between A and C in the stacked structure of A - C - A - B - C after the dislocations in Fig. 4 move, and a layer (D) is formed. After that, when the edge dislocation of Fig. 6 passes, the D atom of the layer (D) is crushed by the layer of Pd and a plurality of D atoms enter one O site.

2) Ignition

At this time, the speed at which the Pd atoms return to the fixed position is a function of the elastic constant and the density of Pd. The sound velocity c is expressed by the following equation.

$$c = \sqrt{\frac{M}{\rho}}$$

Where M is the elastic constant of Pd and ρ is the density of Pd. The speed of sound is 3070 m/sec, which is 5.2 eV in terms of kinetic energy per Pd atom. If several layers of Pd are approaching from above and below, and one D nucleus receives the kinetic energy of ten Pd atoms, the D nucleus will have kinetic energy of 52 eV. If there are D nuclei with kinetic energy of 52 eV among many abnormally accumulated D nuclei, nuclear fusion can be caused with a significant probability by the tunnel effect.

If D-D fusion occurs, the following well - known reactions occur.

(a) $^{2}H + {}^{2}H \rightarrow {}^{3}{}_{1}H$ (1.0MeV) + p (3.0MeV)

(b) $^{2}H + {}^{2}H \rightarrow {}^{3}{}_{2}He$ (0.8MeV) + n (2.5MeV)

(c) $^{2}H + {}^{2}H \rightarrow {}^{4}{}_{2}He + \gamma$ (23.8MeV)

When ^{1}H, ^{2}H, ^{4}He are described in the reaction formula, these represent the nuclei present as interstitial atoms, and when p, D, α are described ion beams of ^{1}H, ^{2}H, ^{4}He, respectively. For other nuclei I do not write like this.

3) Ignition part of Transformation sample

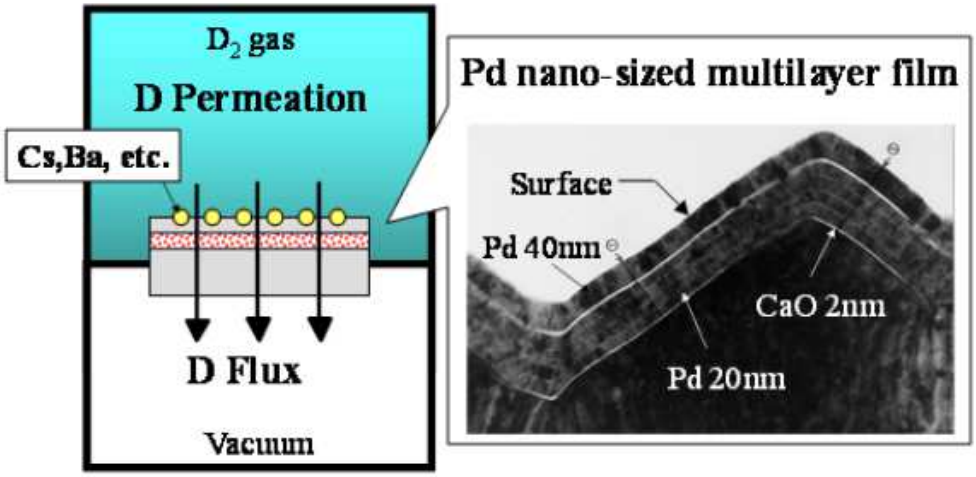

Fig.8 Transmutation sample profile[1].

Fig.8 shows a conceptual diagram and a partially enlarged photograph of the surface of the experimental sample of Iwamura et al[1]. There is a laminated structure of five layers of 2nm of CaO and 20nm of Pd on the upper surface of a 1t pure Pd plate and a 40nm Pd layer obtained by further mixing a substance to be converted thereon. Since the upper surface of this sample is filled with D_2 gas and the lower surface is in vacuum, permeation of D occurs.

The function of the laminated structure of Pd - CaO is thought to be that CaO plays the role of a flat orifice, and permeation becomes uniform by the laminated structure.

Therefore, it is considered that the Pd layer on the upper side of the laminated part is the ignition part with high D concentration. This is thought to make it easier for D - D nuclear fusion to occur by increasing the solid solubility of deuterium and making it deformable easily.

Fig. 9 shows the State diagram of palladium and hydrogen[4]. The D/Pd ratio of the surface seems to be around 0.57 under the condition of 80°C and 200kPa which is written as high reaction rate in transmutation experiments[1].

Since it is a deuterium permeation in a static state, it seems that there is no shift of

dislocation if it is simply considered. However, in this experiment, on / off valve is used for supply control of deuterium gas, and fluctuation of pressure is reported. If there is pressure fluctuation, the thin film sample undergoes a change in bending load due to pressure. In addition, Pd expands upon transformation from α phase to α' phase. Since this phase transformation occurs for each crystal grain, even a subtle change in pressure or a change in temperature distribution will result in expansion of a part of the crystal grains in the whole. The grains around the expanded crystal grains are subjected to tension, and the expanded crystal grains themselves undergo compression. In this way, even though the entire sample appears static, the dislocation will cause movement and D-D fusions will occur.

The microstructure of the triangular groove formed on the surface has an effect of a role of concentrating stress on the α' layer of the valley groove portion, I think.

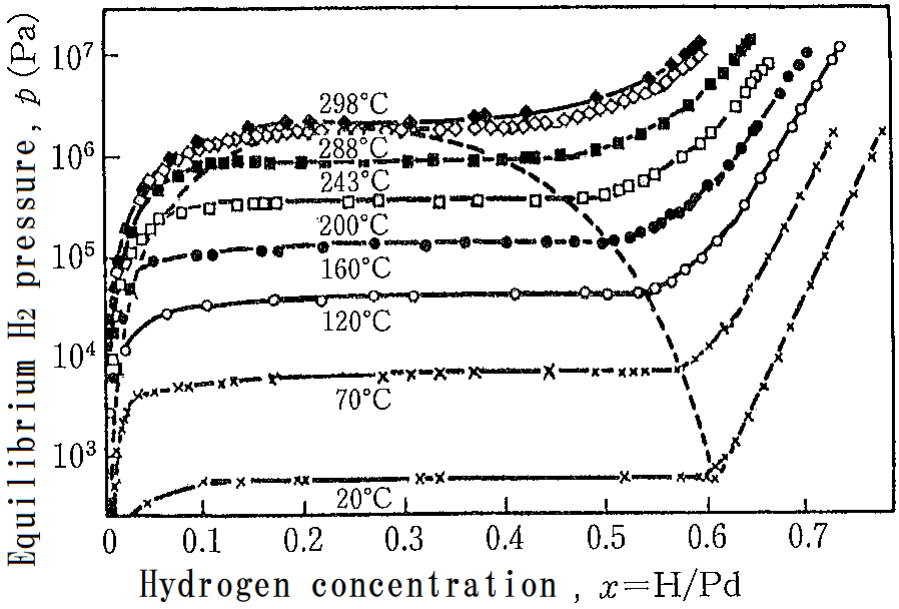

Fig.9 State diagram of palladium and hydrogen[4].

3. Combustion reaction

1) Find a missing piece

The charged particles of p, $^{3}_{1}$H, and $^{3}_{2}$He generated by the D-D fusion have sufficient kinetic energy to overcome the Coulomb barrier with the interstitial atom D and cause nuclear fusion. However, reaction cross section is only 6b for $^{3}_{1}$H and 0.8b for $^{3}_{2}$He at the maximum [5], these charged particle beams are stopped at a distance of about 10μm in Pd by stopping power. Even for the $^{3}_{1}$H beam having a larger reaction cross section, the D nuclei uniformly distributed at a concentration of D / Pd = 0.7 farther than 2.75Å which is the distance of the adjacent O site in a sphere of 10μm radius, calculating the cross-sectional area as an average

of 5b, the total reaction cross section is only 1.5×10^{-8} of the full solid angle. Therefore, the probability that the generated charged particles collide with the D nucleus as an ion beam is extremely low, and the probability of nuclear fusion chain reaction has been considered to be extremely low.

If one D-D nuclear fusion is the starting point and a significant nuclear fusion chain reaction occurs, the cylinder filled with deuterium gas at high pressure becomes a nuclear bomb by a strong cosmic ray. But such things will not happen. This suggests that "If there is a chain reaction in the Pd crystal, there must be a mechanism to increase the fusion probability in the Pd crystal". So, I decided to look for this missing piece.

2) Mechanism to increase probability of nuclear fusion in crystal Part 1: Channeling phenomenon

The first thing I focused on is channeling phenomena due to crystals which are known for crystallinity evaluation of Rutherford backscattering analysis and abnormal doping depth during semiconductor manufacturing. This Rutherford backscattering analysis is a technique to measure the energy and intensity of ions scattered backward by irradiating a solid sample with an ion beam and scattering.

Charged particles generated in equations (a) and (b) are ion beams with energy values in parentheses. Due to the channeling phenomenon, the crystal field gives directivity to the ion beam, so the ions with positive charges are confined by the crystal lattice of Pd and pass between the crystal planes. One of the causes of such directivity is the Coulomb force from the nuclei constituting the crystal lattice. The other is magnetic repulsion caused by movement of free electrons and electrons peeled off from atoms by an ion beam so as to cancel magnetic lines of force generated by the movement of ions. This force strongly receives from the denser side of the electron distribution. As a result of these forces, when the sparse part of the crystal lattice is out of the center of the continuous path, a force returning to the center works, and the ion beam will make a gentle S-shaped turn slightly off the straight line along the channeling path.

When the charged particles perform acceleration motion, they emit energy as electromagnetic waves. The electromagnetic wave energy P radiating per time is expressed by the formula of Larmor as follows.

$$P = \frac{q^2\dot{\mathbf{u}}^2}{6\pi\varepsilon_0 c^3} = \frac{2}{3}\frac{1}{4\pi\varepsilon_0}\frac{q^2\dot{\mathbf{u}}^2}{c^3} \qquad \cdots(1)$$

Here, ε_0 is the vacuum permittivity, q is the charge, ù is the acceleration vector, and c is the speed of light. Since the product of vectors here is an inner product, P is a scalar quantity.

Fig. 10 S-shaped turning ion beam

Fig. 10 is a schematic diagram showing the movement of an ion beam that makes an S-shaped turn when the center line of channeling path is indicated by a dotted line. Here, the stopping power in the direction of the channeling path is neglected. When the ion beam deviates from the center line of channeling path, it receives a force in the direction of returning to the center line, that is, acceleration ù. This acceleration ù increases with increasing distance from the center line.

Since electromagnetic waves proportional to the square of this acceleration ù are emitted from equation (1), the attenuation of the S-shaped turning motion increases as the distance outside the center line increases. Since the metal reflects this electromagnetic wave as a fixed end, the attenuation becomes stronger. Therefore, the movement of the ion eventually becomes linear, and it passes through the center of the sparse part of the crystal lattice accurately. As a result, the probability that the ion beam collides with the D nucleus of interstitial atoms increases.

Here, supplementation will be made on the probability of the ion beam entering the channeling path. When irradiating the proton beam to the <100> direction from the outside of the sample of tungsten, the scattering probability abruptly increases when the angle is tilted by 2°[6]. The solid angle of this half apex angle of 2 ° is only 0.0003045 of the total solid angle, but this is only the probability of entering one channeling path when the ion beam first enters the metal. Azimuths that can be represented by numbers up to 2 have a total of 98 directions including <100> 6 directions, <110> 12 directions, <111> 8 directions and <210> <211> <221> 24 directions each. Also, the internally generated ion beam gains chances as long as it does not go out even if scattered inside, so the probability of getting into the channeling path if it scatters 100 times exceeds 95%. Rather, the probability is lower that the channeling path in which the D nucleus falls behind the Pd atom is 62 directions among these 98 directions.

In addition, the probability of making the D nucleus into an ion beam by Coulomb force and nuclear force as the ion beam passes through the neighborhood is higher than the ion beam directly collides the D nucleus. This D ion beam has energy due to Coulomb repulsion of the nucleus of the original ion beam. For the mechanism of delivering energy, please refer to the explanation of “4-1) Binary nucleus model” below. In this way since the number of ion beams increases, there is an effect of increasing the fusion probability. These are the

expansion mechanism of the nuclear fusion rate due to the channeling phenomenon.

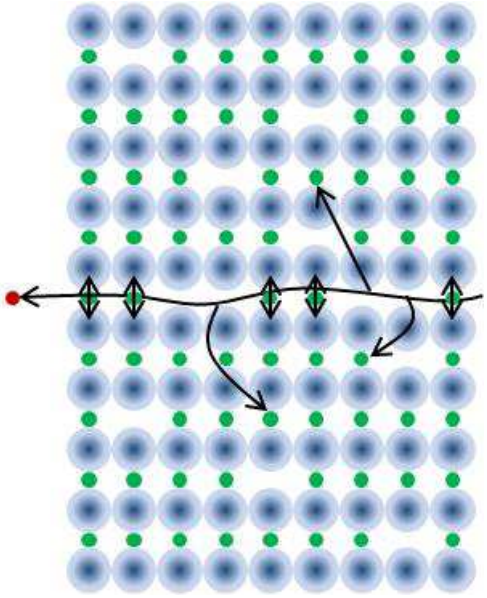

Fig.11 α’ phase Palladium.

In order to facilitate the channeling phenomenon, it is necessary to have a crystal structure with few lattice defects. Fig.11 is a conceptual diagram of the α' phase of Pd. Since the D nucleus of the interstitial atom bends the path by the Coulomb force with respect to the ion beam coming through the channeling path, even if the channeling phenomenon occurs at high D concentration, the accuracy of centering is poor and it cannot give the nucleus fusion energy to the D nucleus.

Fig.12 is a conceptual diagram of the α phase of Pd. The thinner the D concentration, the better the centering accuracy due to the channeling phenomenon, the closer the ion beam to the interstitial atoms D nucleus, the more energy can be delivered. Since the α nucleus has twice the charge of the D nucleus, the D ion beam generated at this time will exceed the Coulomb barrier of the D nucleus with a high probability. However, if it is too thin, it will be impossible to generate a D ion beam, and the D ion beam will not collide the D nucleus, so that the D-D fusion will not occur. Thus, there is a suitable concentration of D in the chain reaction. Many experiments have tried to simply increase the D concentration so far, but it seems that it was necessary to adjust the concentration more. In fact, there is experimental example in which a large amount of abnormal heat generation was observed after the majority of deuterium was released from the sample, after electrolysis in electrolysis experiments [7].

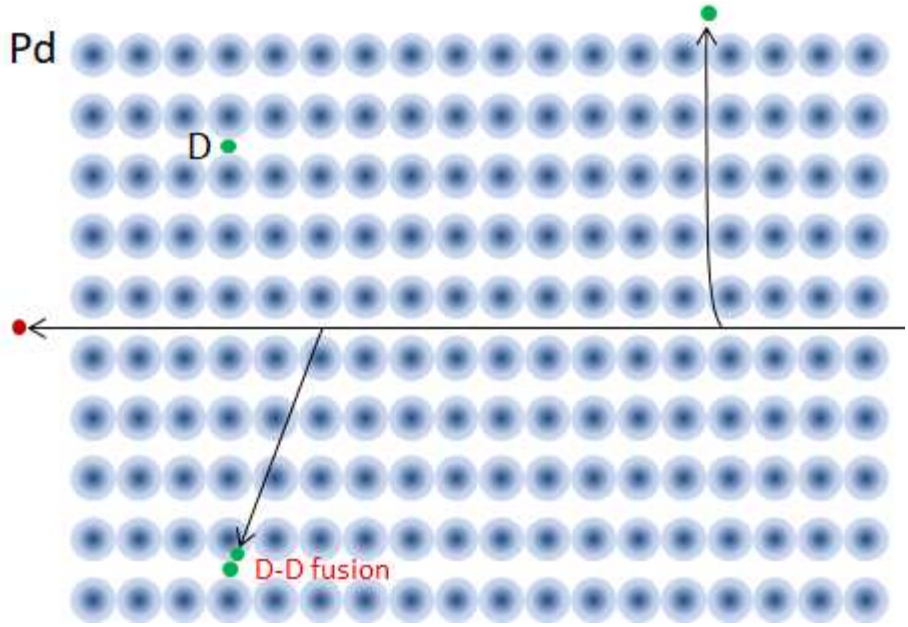

Fig.12 α phase Palladium.

3) Experiments suggesting an increase in fusion probability due to channeling phenomenon

Fig.13 shows the relationship between the shielding energy and the deuteron density of the D (d, p) T reaction when a large amount of D ion beam is implanted into each metal [8]. The effect that the charge of the nucleus is canceled by the electron is called a shielding effect. And the atom that gathers electrons than the bare atomic nucleus can obtain the same nuclear reaction rate with the ion beam of low energy, so this energy difference is called shielding energy. As can be seen from the following FIGS. 18 and 19, the higher the shielding energy Us, the higher the rate of increase of fusion probability. In the case of metals, this shielding energy is one order of magnitude larger than that of nonmetals[9]. However, the reason for this has not been explained so far.

In Fig. 13, since the horizontal axis is the reciprocal of the density, it is shown that the lower D density, the larger the shielding energy. The higher the shielding energy is, the higher the probability of D - D nuclear fusion is, so that the lower the D density, the higher the fusion probability.

Since the channeling phenomenon is a phenomenon caused by a crystal lattice, the channeling phenomenon is more likely to occur with less crystal lattice defects with large crystal and no distortion. Here, D is an interstitial atom of Pd, so it is one of lattice defects. Here, D ions exceeding the D concentration of each α phase are irradiated to each metal of Ti, Au, Fe, and Pd. By irradiation with such a large amount of D ion beam, it is considered that a hydrogen compound and β phase are precipitated inside the samples, the crystals are refined and large internal stress is generated, further the crystal structure of the metal is broken and it

becomes amorphous. On the other hand, PdO is considered to have a low D density and a good crystalline state, so that channeling phenomenon is likely to occur.

From these facts, I think that Fig. 13 shows that the easier the channeling phenomenon occurs, the fusion probability increases. Through the channeling phenomenon, the D ion beam penetrates precisely between the lattices and passes through where the D nucleus of interstitial atoms exists.

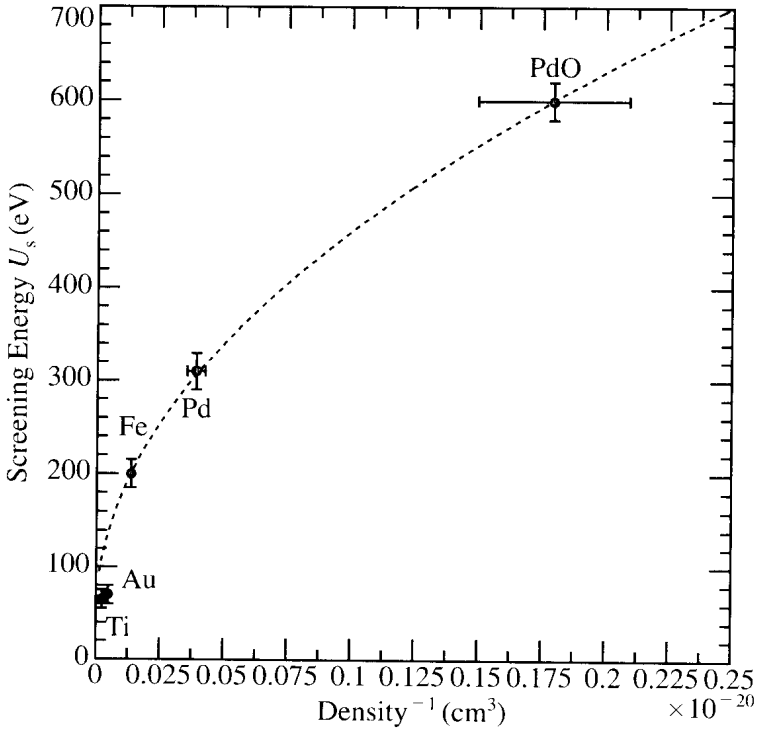

Fig. 13 Relationship between fusion probability and deuteron density of D(d, p)T reaction in metal[8].

4-1) Mechanism to increase probability of nuclear fusion in crystal Part 2: Binary nucleus model

However, usually in the case of D-D nuclear fusion, the reaction cross section is reduced to 10^{-4} b at around 20keV[5]. This is quite small for Pd crystal lattice with a lattice constant of 3.89 Å. Although it leads to the path where the D nucleus is present due to the channeling phenomenon, the fusion probability is unlikely to be high enough to cause a chain reaction.

By the way, at this time, D nucleus is not exactly fixed at the center of the O site, but it is distributed with high probability that it exists near the center of the O site by the uncertainty principle. Since it is considered that the temperature range of D nucleus is considerably limited by exchanging phonons with free electrons, if the temperature range of D is about 100 degrees, the uncertainty Δp of the momentum represented by the expression (2) is 28.8 × 10

$^{-25}$ [kgm / sec], so the uncertainty of the position of the D nucleus Δx is 3.6μm. It is thought that D nucleus is distributed over a fairly wide range of O sites.

$$\Delta x \, \Delta p \geqq \frac{h}{2\pi} \qquad \cdots (2)$$

Also, if the cause of excessive heat generation is ordinary D-D fusion, neutrons and charged particles should appear as in the above formula (a) or (b). Further, the charged particles cause secondary reaction and tertiary reaction as described below. Therefore, if it reacts actively enough to generate a large amount of excessive heat, radiation with strong penetrating power such as neutrons and gamma rays contained in the reactions of (d), (f), and (g) appears.

(d) $p + {}^{2}H \rightarrow {}^{3}He + \gamma$ (5.5MeV)

(e) ${}^{3}He + {}^{2}H \rightarrow \alpha$ (3.7MeV) + p (14.7MeV)

(f) ${}^{3}H + {}^{2}H \rightarrow \alpha$ (3.5MeV) + n (14.1MeV)

(g) $\alpha + {}^{2}H \rightarrow {}^{6}Li + \gamma$ (1.5MeV)

This is in contradiction to the result that excessive heat is greater than 12 to 13 digits, calculated from the measured number of neutrons in the case of a large amount of excessive heat[10]. Also, no notable γ rays have been reported. Therefore, the authors felt that a model to further increase the fusion probability and cause mild nuclear fusion without neutron beams and gamma rays is necessary, and constructed “Binary nucleus model” to be described from now on.

Consider the case where a floating star enters the gravity region of the sun. Since the total energy of kinetic energy and potential energy of floating stars and the sun is preserved, normally it is not possible to capture floating stars as a binary star unless the floating stars collides with the sun. A floating star passes through the vicinity of the sun, goes out of the gravity area, returns to outer space again, and the sun obtains kinetic energy by the gravitation of the floating star. This is easy to understand when thinking that the total energy is preserved in the coordinate system with the center of gravity of both the floating star and the sun as the origin.

However, when there is a large amount of dust around the sun like the primitive sun, when the floating star pass through the vicinity of the sun, it is decelerated by the surrounding dust, so it may not be able to return to space again. In this case the sun takes in the floating star and becomes a binary star.

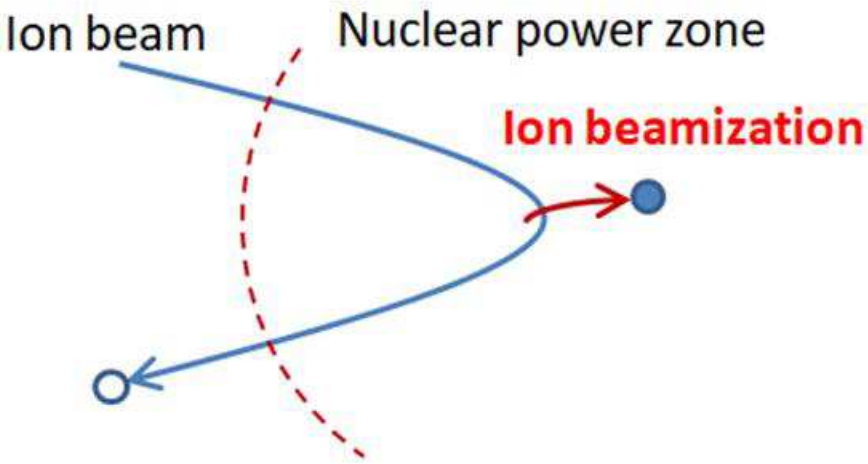

Fig.14 Ion beam pass through the nuclear power zone,

Fig.14 is a conceptual diagram in which the floating star is replaced with ion beam and the sun is replaced with interstitial atom. Let X be the nucleus of this interstitial atom. Since the centering is performed by the channeling phenomenon, the probability of the ion beam striking against X also increases, but the number of ion beams entering the nuclear power zone of X is much larger. When the ion beam has energy exceeding the Coulomb barrier of X, most of the ion beam that came towards X enters the nuclear power zone of X but changes its direction and flies away. The ion beam is scattered by X and X acquires momentum by nuclear force and coulomb force by ion nucleus.

Fig. 15 is a conceptual diagram of the distance between the D-D nucleus and the potential energy. The vertical axis Y is obtained by converting the potential energy Ep by the following equation.

Y= 40-Ep [keV]

This Y is a coefficient set to represent Ep where positive and negative are switched by one logarithmic graph, and has no physical meaning. The vertical axis is reversed. The horizontal axis is the D-D internuclear distance and is drawn at the position of Ep = 0(Y=40). The Ep was obtained as follows.

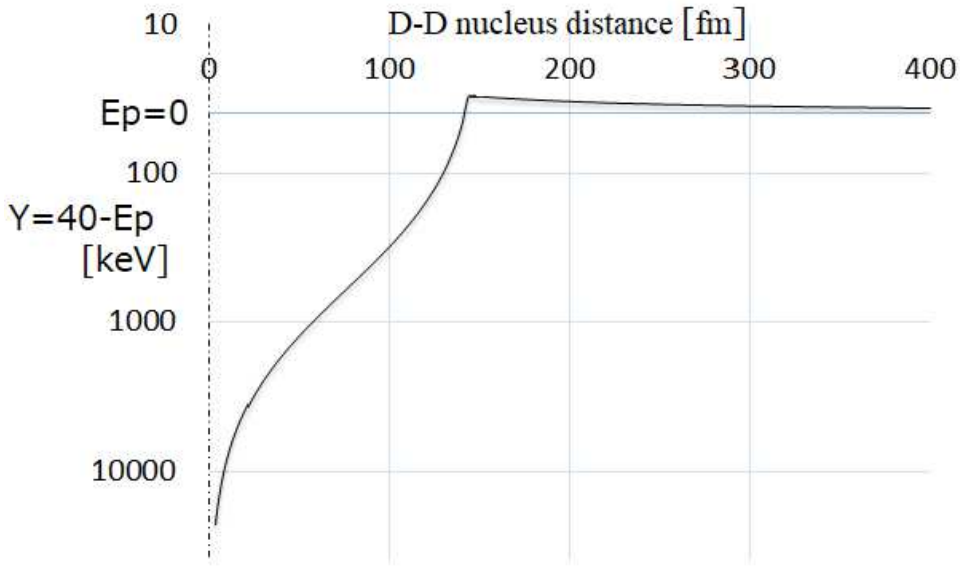

Fig. 15 D-D nucleus distance and potential energy conceptual diagram.

Coulomb force Fc: It is a well-known formula in Coulomb's law, but it is a repulsive force, so it is a minus.

$$Fc = - e^2/(4\pi\varepsilon_0 L^2)$$

Where ε_0 is the vacuum permittivity, e is the charge of the deuterium nucleus and L is the D-D internuclear distance.

Nuclear force Fn: that was constructed so that Fig. 15 approaches the author's image, and there is no physical basis. If the nuclear force Fn is inversely proportional to the third power of L or more, centrifugal force that balances the nuclear force cannot be obtained even if accelerated by nuclear force. Therefore, I assumed that Fn is inversely proportional to the square of L as well as the Coulomb force.

When $L > L1$

$$Fn = 0$$

When $L \leq L_1$

$$Fn = 1/(4\pi NL^2)$$

Where L_1 is the distance of the Coulomb barrier of D nucleus and N is the nuclear force coefficient. As I thought that the nuclear power varies depending on the combination of nuclides, I set N as a coefficient corresponding to ε_0 / e^2.

The sum of the Coulomb force and the nuclear force integrated by L is the potential energy

Ep.

$$Ep = \int_{L}^{\infty} (Fc + Fn)\, dL$$

The integral constant is obtained from the fact that Ep = 0 when L = ∞, and Ep is continued at L = L_1, and the following equation can be obtained by substitution.

When L > L1

$$Ep = e^2/(4\pi\varepsilon_0 L) \qquad \text{---(3)}$$

When L ≤ L1

$$Ep = e^2/(4\pi\varepsilon_0 L) + 1/(4NL_1) - 1/(4NL) \qquad \text{---(4)}$$

Assuming that the height of the Coulomb barrier is Ep = 10KeV, L1 = 144fm can be found from the equation (3). Assuming that Ep is -23.8 MeV of generated energy when ^{4}He is generated when Lmin = 3.56fm of the diameter of the maximum reaction cross section 0.1b[5] during D-D nuclear fusion, N = $2.25 \times 10^{+25}$ can be found from the equation (4).

Below, if affirming the Fig. 15, when the D ion beam of 20keV comes closer to the D nucleus of the interstitial atom from right in front, the kinetic energy of the D ion beam becomes 10keV when approaching 144fm by the Coulomb repulsive force, and conversely, the D nucleus which was the interstitial atom is accelerated to 10KeV, and the speeds are almost the same. Once the relative velocity at the apex of the Coulomb barrier is almost 0, the D ion beam falls straight towards the D nucleus and causes nuclear fusion.

If the angle of the D ion beam slightly deviates, it will climb the Coulomb barrier diagonally and will shift laterally more. It cannot exceed the Coulomb barrier and nuclear fusion reaction does not occur. In this way of thinking, it can be explained that the smaller the energy D ion beam, the smaller the reaction cross section becomes. The reaction cross section of the D-D nuclear fusion is maximum at about 0.1 b even when the energy of the D ion beam is several MeV, decreases as energy decreases, and decreases to 10^{-4} b at about 20keV[5].

Conversely, for example, when an α beam of 6.2MeV is incident at a slight angle to the D nucleus of an interstitial atom, it goes beyond the Coulomb barrier once into the nuclear power zone, but it goes around the D nucleus and turns in the shape close to an open ellipse, and it goes out beyond the Coulomb barrier again. At this time, the D nucleus of the interstitial atoms is accelerated by the Coulomb force and the nuclear force of the α ion beam nucleus and gets kinetic energy.

In the case where D nucleus gets the greatest energy, the case where the ion beam passes near the D nucleus is a case where the α beam is inverted by almost 180 degrees when the center of gravity of the two nuclei are used as a reference. Calculating that the total energy is

preserved, when the α ion beam with the mass number 4 and the velocity 3 comes, the D nucleus with the mass number 2 is accelerated to the velocity 4 and the α ion is decelerated to the velocity 1, so that 8/9 of kinetic energy of the α beam is delivered. In the case where D nucleus gets the smallest energy, in the case where the ion beam slightly passes through the course of entering the nuclear power zone of D nucleus, and the bending due to the coulomb force is canceled by the bending by the nuclear force, the delivered energy becomes almost zero. In this way, D ion beams with various energies from about 0 to 5.5MeV are generated.

Similarly, the D nucleus got a large energy and becomes a D ion beam gives energy of at least 0 and at most 1/2 to the next D nucleus. In this way, ion beam which got the large energy and Ion beams with large remaining energy will ionize D nuclei of interstitials one after another. In this way, as described in 2) "Channeling phenomenon", if the channeling phenomenon stably occurs, the energy of the ion beam having high energy is distributed to the D nuclei of the interstitial atoms and many D ion beams are generated.

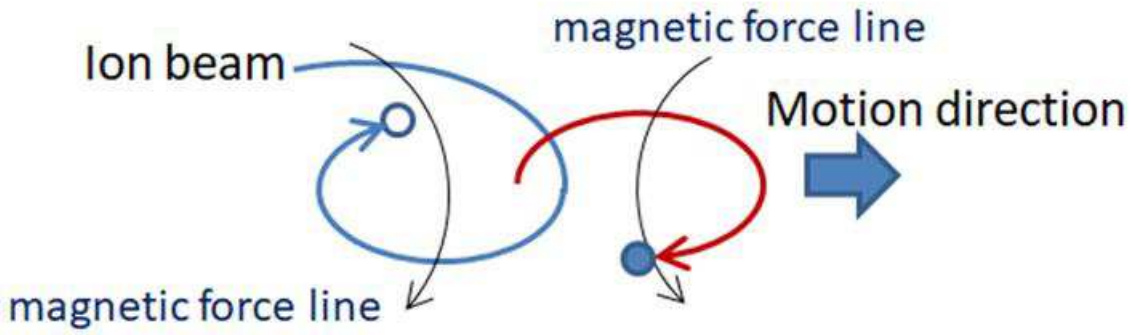

Fig.16 Binary nucleus formation.

Fig.16 is a conceptual diagram in the case where an ion beam having energy capable of exceeding the Coulomb barrier enters the nuclear power zone of X. Since both the ion beam and the X nucleus are charged particles, when they rotate around each other, electric current flows in the orbit. Free electrons in the metal are moved in a direction that cancels the lines of magnetic force generated from this current, resulting in eddy current, which replaces heat by electric resistance. In this way, since the swirling kinetic energy of the charged particles is absorbed in the metal, there are cases in which they are in a state in which they rotate around each other. Let's call this a binary nucleus.

Let us now consider an ion beam that has energy below the Coulomb barrier. Even when a D ion beam of 20keV or less is incident at a slight angle to the D nucleus of the interstitial atoms, it may enter the nuclear power zone due to the tunnel effect and forms a binary nucleus. But, since the swirling energy is not absorbed in vacuum or nonmetal, either of them is necessarily separated by tunneling effect, so it is observed only as scattering.

However, since the swirling energy is absorbed in the metal, the binary nucleus is less likely to separate in the metal. If the Coulomb barrier is at the same height, the tunneling effect increases as the energy of the ion beam increases. Therefore, the higher the energy amount of the ion beam, the easier it is to become a binary nucleus beyond the Coulomb barrier, but on the other hand it is easier to separate beyond the Coulomb barrier by the tunnel effect. In other words, the possibility that the ion beam forms a binary nucleus together with an interstitial atom is increased in the both solid and liquid metal, and the possibility that the formed binary nucleus may separate is low.

Since the momentum of the binary nucleus is equal to the momentum of the incident ion beam, the motion direction of the formed binary nucleus becomes the same as the incident ion beam. When the ion beam enters from the left in Fig. 16, the consecutive nucleus moves to the right like an arrow. Therefore, when an ion beam enters along a channeling path to form a binary nucleus, the formed binary nucleus also goes on the same channeling path as it is. And the binary nucleus becomes a binary ion beam. The pivot axis of the binary nucleus is perpendicular to the direction of the incident ion beam. Since the binary nucleus emits magnetic lines of force in the direction of this pivot axis, magnetic flux penetrates into the metal at right angles to the direction of travel. Therefore, an eddy current is generated in the metal, and a strong stopping power is exerted on the binary ion beam.

If the concentration of D in the metal is low, it stops without colliding the D nucleus, captures the surrounding electrons as the binary nucleus and fits between the metal lattices as a pseudo atom. Because the charged particles receive acceleration due to the nuclear force of each other's nucleus forming a stationary binary nucleus, they continue to emit energy as electromagnetic waves according to Larmor's formula (1). The turning diameter of the binary nucleus becomes small, and the nuclei constituting the binary nucleus get close to each other, and eventually nuclear fusion occurs.

This binary nuclear model also solves the problem of reaction cross section. Since the area of the circle with a radius of 144fm in Fig.15 is 651b, the possibility of nuclear fusion via the binary nucleus is much higher than the possibility that direct D nuclei collide directly. An ion beam that exceeded the Coulomb barrier and entered the nuclear power zone, drawn by nuclear forces and approach the nucleus of the opponent once, but if energy is not lost, it returns to the same Coulomb barrier again in orbits close to the ellipse. At this time, the swirling kinetic energy may be absorbed by the metal as described above and become a binary nucleus in some cases.

Looking a little more in detail, when each other's nucleus approaches, since the nuclear power is strong and the speed is fast, since large current flows with a small radius, high-density lines of magnetic force appear. When the line of magnetic force changes, in the

metal the current flows in the direction to suppress the change and changes to heat, a large amount of kinetic energy is lost at the intersection of long circular orbitals where the magnetic field line changes greatly, and the orbit will approach the circle. Explain again using Larmor's formula (1), the ion beam generates a lot of electromagnetic waves and loses a lot of kinetic energy in the part where the nuclear power works strongly. Since the metal reflects this electromagnetic wave as a fixed end, the loss of kinetic energy becomes larger within the metal and the orbit becomes closer to the circle faster.

The D-D binary nucleus takes over the momentum of the D ion beam that entered during formation, and the mass after formation is doubled, so the velocity is halved. Therefore, the kinetic energy of the D-D binary ion beam with half the speed of the incoming D ion beam is halved. The remainder becomes turning kinetic energy of the binary nucleus.

If a D ion beam of 60KeV is entering the nuclear power zone of D nucleus by a tunnel effect at an angle that cannot come beyond the Coulomb barrier, 30KeV becomes the kinetic energy of the D-D binary ion beam and the remaining 30KeV becomes the internal energy of the binary nucleus. Considering the center of gravity of the binary star as the origin, the kinetic energy is 15keV per D nucleus at Ep=0 points. D nucleus gains speed by nuclear power when approaching each other, and returns to its original position against the nuclear force by centrifugal force if the speed goes up too much. If D nuclei can keep the elliptical orbits, there are chances to get closer to the Coulomb barrier as many times as possible and again to escape from the nuclear power zone by the tunnel effect.

The D-D nuclear distance in the conceptual diagram of Fig. 15 corresponds to the diameter of the turning circle of the D-D binary nucleus. In the conceptual diagram of Fig. 15, the nuclear power is drawn as being proportional to the reciprocal of the square of the distance. If the nuclear power follows this calculation, taking the circular orbit while maintaining the internal energy, in order to obtain the speed at which the nuclear power and the centrifugal force are balanced, it is necessary for the D-D nuclear distance to approach 50fm. The total turning kinetic energy of the two D nuclei at this time is about 900keV.

Since it is necessary to convert the potential energy to kinetic energy so as to be balanced with the centrifugal force in this way, the D nucleus moves away from the Coulomb barrier as it becomes a circular orbit and it becomes difficult for D nucleus to leave the nuclear power zone. So, when the binary nucleus does not separate when the turning trajectory in the early stage of the binary nucleus formation is close to an ellipse, there is no chance to approach the Coulomb barrier afterwards, and the possibility of eliminating the binary nucleus by the tunnel effect becomes extremely low. Since the acceleration due to nuclear force is large, the emission of electromagnetic waves by Larmor's formula (1) is also large, and once it is settled as a binary nucleus, it causes almost fusion.

This nuclear fusion will be a "Mild nuclear fusion" with much lower energy than usual. Normally, when a D-D fusion occurs, it branches to one of the nuclear fusion reactions (a) to (c) above. However, when approaching about 10fm in the form of losing the 4MeV swirling energy as an electromagnetic wave as it is, the branches of (a) and (b) can no longer occur. When the binary star nucleus approaches to about 4fm, almost all the 11.4MeV of the remaining fusion energy after losing as electromagnetic wave is converted into kinetic energy. Therefore, when the reaction of equation (c) occurs at about 4fm, when ^{4}He is generated, it radiates kinetic energy as phonons and transmits it as heat to nearby Pd nuclei, and the remaining small energy γ rays are emitted.

4-2) Incomplete combustion due to excess D

As shown by the State diagram of palladium and hydrogen in Fig. 9, the D / Pd of the α 'phase at 100 ° C exceeds 50%. Since the binary ion beam goes on the same channeling path as the captured D ion beam, if D / Pd is 50%, there is a D nucleus of an interstitial atom at the O site where one was placed, and as soon as it is formed collide with D nucleus.

As described above, the kinetic energy of the D-D binary ion beam is half of the D ion beam taken in its formation, and the internal energy also has the same value. If the coulomb barrier between the D nuclei is set to 10keV as shown in Fig. 15, unless the tunnel effect is taken into consideration, unless the D ion beam exceeds at least 20keV, the binary nucleus is not formed beyond the Coulomb barrier. That is, the kinetic energy of the D-D binary ion beam immediately after formation is at least 10keV and the internal energy is also 10keV.

When the coulomb barrier height between D nuclei is 10keV, the coulomb barrier height of the D-D binary nucleus and D nucleus is 20keV. Also, when the D-D binary ion beam collides with a stationary D nucleus, when looking at the center of gravity as the origin, the speed of the D-D binary ion beam is 1/3, and the D nucleus with a mass number of half is approaching at a speed 2/3 from the reverse direction. From this point of view, total kinetic energy is 1/3 of the kinetic energy of the original D-D binary ion beam, which is the maximum energy that can be used to exceed the Coulomb barrier. Therefore, in order for the D-D binary ion beam to exceed the Coulomb barrier of the stationary D nucleus, a minimum energy of 60keV is required. For the kinetic energy of the D-D binary ion beam to be 60keV or more, a D ion beam of 120keV or more is required. Conversely, even if a D-D binary ion beam formed by a D ion beam with an energy of 120keV or less collides with D nucleus, it will be pushed back by its Coulomb barrier.

In the D-D binary nucleus that has just formed the binary nucleus, the orbit of the lower internal energy is flattened, and the closest distance is close to the size of the nucleus. Therefore, when the D-D binary nucleus collides with the D nucleus of the interstitial atom,

the binary nucleus orbit will bend with the Coulomb force of the D nucleus, and the D nuclei constituting the binary nucleus collide with each other, resulting in ordinary D-D fusion. The lower the energy, the lower the possibility of forming a binary nucleus, but since the nearest distance of orbit is closer to the D-D binary nucleus formed by the low energy D ion beam, the possibility that the D nuclei constituting the binary nucleus collide with each other and cause ordinary D-D fusion increases.

However, when a D ion beam of 120keV or more is used, since the D-D binary ion beam enters the Coulomb barrier, there is a possibility that 3D nuclear fusion will occur as well as D-D nuclear fusion where two nuclei collide. 3D fusion splits into the following two equations[11].

(h) $\underline{D + D} + {}^{2}H \rightarrow {}^{3}He$ (4.7MeV or less) + ${}^{3}H$ (4.7MeV or less)

(i) $\underline{D + D} + {}^{2}H \rightarrow \alpha$ (7.9MeV or less) + D (15.8MeV or less)

Here, it is shown that the underline part is a binary ion beam state.

This reaction occurs in the same way when the D ion beam goes into the binary nucleus just fits between the lattices as a pseudo atom. In this case, the minimum required energy of the D ion beam is 30keV which is 3/2 of 20keV of the height of the Coulomb barrier.

If ion beams of ${}^{3}He$ or ${}^{3}H$ are generated by the equation (h), the reactions of the equations (e) and (f) occur, and α rays, p rays and neutron rays are generated. The reaction of equations (a) to (c) takes place from ordinary D-D fusion, and the secondary reaction and tertiary reaction from (d) to (g) occur. Therefore, from the p generated by the reaction of the equation (e), the following triple nucleus fusion may also occur.

(j) $\underline{p + D} + {}^{2}H \rightarrow \alpha$ (4.8MeV or less) + p (19.1MeV or less)

From the above, when a D ion beam of 120keV or more is used in the state of excess D, ${}^{3}He$ (4.7MeV or less), ${}^{3}H$ (4.7MeV or less), α (7.9MeV or less), D (15.8MeV or less) and p (19.1MeV or less) which do not appear in ordinary D-D fusion occurs. If these particles can be confirmed, the presence of a binary ion beam can be proved. However, such these reactions occur, neutrons and gamma rays are emitted.

4-3) Complete combustion (Nuclear fusion chain reaction)

When the D/Pd concentration is not high enough to cause the above incomplete combustion, after formation of the D-D binary ion beam, it does not collide with other D nuclei and fits within the lattice as a pseudo atom as it is a binary nucleus. Since the nucleus constituting it continue to be accelerated to each other, they gradually lose energy due to braking radiation and approach, to "mild nuclear fusion" and change to 4He nuclei. This is expressed by the following equation.

(k) $D + {}^{2}H \rightarrow {}^{4}He$ (~ 0 MeV): For explanation of "Mild nuclear fusion" including

explanation that there is no other branching, please refer to the last row of "4-1) Cascaded kernel model". As described above, D ion beam exceeding 20keV is necessary for binary nucleation.

In this way, ^{4}He increases and ^{4}He accumulates between the Pd lattices, and the reaction of the following equation increases.

(l) $D + {}^{4}He \rightarrow {}^{6}Li$ (1.5 MeV or less) : Since the sum of the masses of D and ^{4}He is less than the sum of ^{3}He and ^{3}H, the reaction as shown in (h) does not occur. Since this is also " Mild nuclear fusion", the energy of gamma rays emitted is small.

In this way, ^{6}Li increases and ^{6}Li accumulates between Pd lattices, and the reaction of the following equation increases.

(m) $D + {}^{6}Li \rightarrow 2\alpha$ (11.2 MeV or less): Branch that binary nucleus of D and ^{6}Li undergoes " Mild nuclear fusion", releasing the rotational moment in the form of phonons to once become ^{8}Be nuclei and separating into two α nuclei by ordinary disintegration may be conceivable. But the energy of the emitted α-beam in this case is as low as 47keV.

However, it is believed that ^{8}Be nuclei are divided into clusters with α nucleus as a unit, and two α nucleus clusters are bonded with loose nuclear power. For this reason, when the binary nucleus of D and ^{6}Li undergoes " Mild nuclear fusion", two α nuclear clusters are formed, at the same time two α nuclear clusters lose the centrifugal force by turning and separate into two α nuclei I believe. Most of the reactions are this branch, in this case since they do not emit phonons, the emitted α-beam inherits the swirling energy of the binary nucleus as kinetic energy. Therefore, I think that it has much higher energy than the α beam due to the collapse of ^{8}Be mentioned above.

Since ^{6}Li is mass three times as large as D, 3/4 of the energy of the D ion beam can be used to come beyond the Coulomb barrier, but in order to form a binary star nucleus, a D ion beam exceeding 40keV is necessary.

Then, this high energy α beam is led to the ^{2}H nucleus of the interstitial atom by the channeling phenomenon, and many D ion beams are generated. This is expressed by the following equation.

(n) $\alpha + {}^{2}H \rightarrow \alpha + D$: A high energy α beam cannot form a binary nucleus but generates many D ion beams. Refer to the explanation of Fig. 15 below.

These chain reactions of (k) to (n) are nuclear fusion chain reaction in the metal crystal which occurred excessive heat with no neutrons or strong γ rays.

If these Li and He concentrations become excessive, the accuracy of channeling is lowered and the chain reaction is difficult to continue. I believe that it is necessary to be equal to or lower than the concentration of Pd α phase of D nucleus having a small mass number. In order to continue the nuclear fusion chain reaction in metal crystal, it is considered that devises to

discharge He of the final product are particularly necessary.

5-1) Experiments suggesting nuclear fusion by Binary nucleus model

I searched for past experimental results that affirm the above binary nucleus model. As a result, I arrived at the phenomenon known as "Abnormally increased phenomenon of nuclear reaction in solid" in Fig.17 and "Shielding effect in metal" in Fig.18.

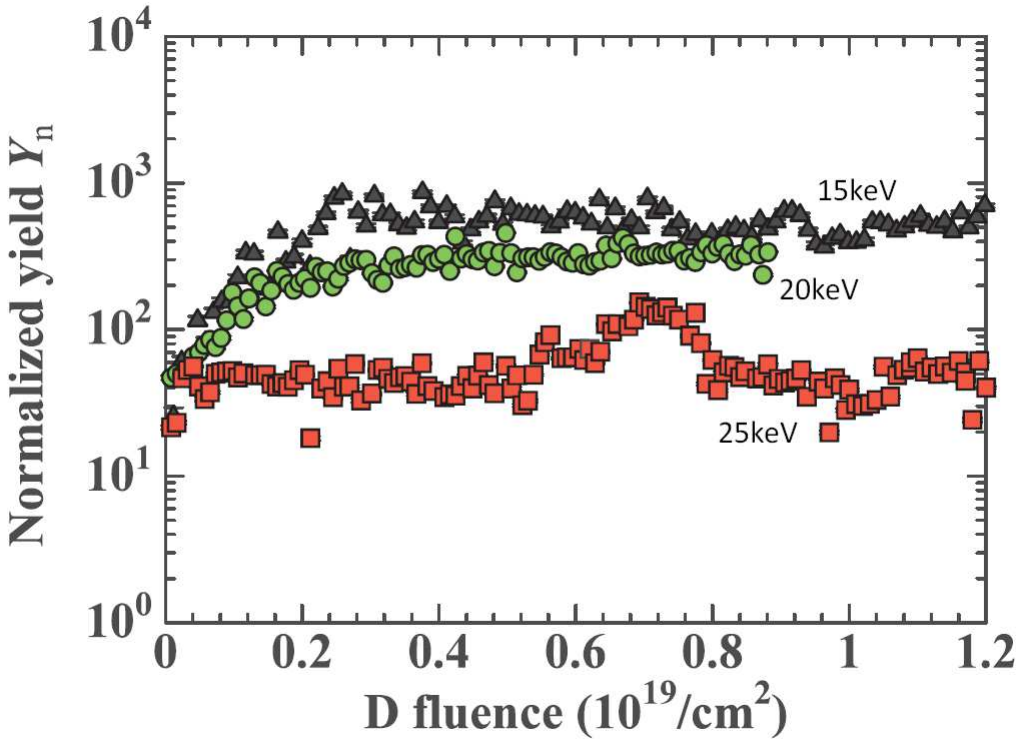

Fig.17 Evolution of yield during D_2^+ irradiation to the Au coating PdDx[12].

Fig.17[12] shows the yield of protons in the case where Au is coated on Pd in which D is dissolved as solid solution, and the D_2^+ ions of each energy are irradiated there. The horizontal axis is the irradiated D fluence. The vertical axis is the normalized yield in which the yield of protons is represented by the usual D-D fusion reaction yield by TRIM calculation as 1. Since D_2^+ molecular ion is used, the energy of the D ion beam is half of the numerical value shown in the figure.

In all cases, the normalized yield is 1 or more, and the lower the ion energy, the larger the normalized yield. This indicates that the fusion probability increases within the metal. Furthermore, as the energy of the ion is lower, the rate of increase of the nuclear fusion probability increases, "4-2) Incomplete combustion due to excess D" is shown.

In this experiment, since the backside of Pd is filled with 1atm deuterium gas, according to the state diagram of Fig. 9, D/Pd = 0.7 if it is 70 ° C. I think the D / Pd ratio is excessive to

cause chain reaction. If the D concentration is excessive, the binary ion beam just formed is collided with the D nucleus, causing normal D-D nuclear fusion by the explanation of "4-2) Incomplete combustion due to excess D". Since protons generated at this time can be counted as yields, I think that the yield of protons increases as the energy of the D ion beam decreases.

Also, if the binary nucleus causes " Mild nuclear fusion", protons will not come out and it will not be counted. I think that ^{4}He generated exists in the Pd sample after D ion beam irradiation. Furthermore, by adjusting the D concentration in Pd, I believe that nuclear fusion via the binary star nucleus can be increased. Then, by irradiating D^{2+} ions with an energy of 80keV or more so that a binary star nucleus can be formed for ^{4}He and ^{6}Li, the nuclear fusion chain reaction can occur and excess heat can be utilized, I believe.

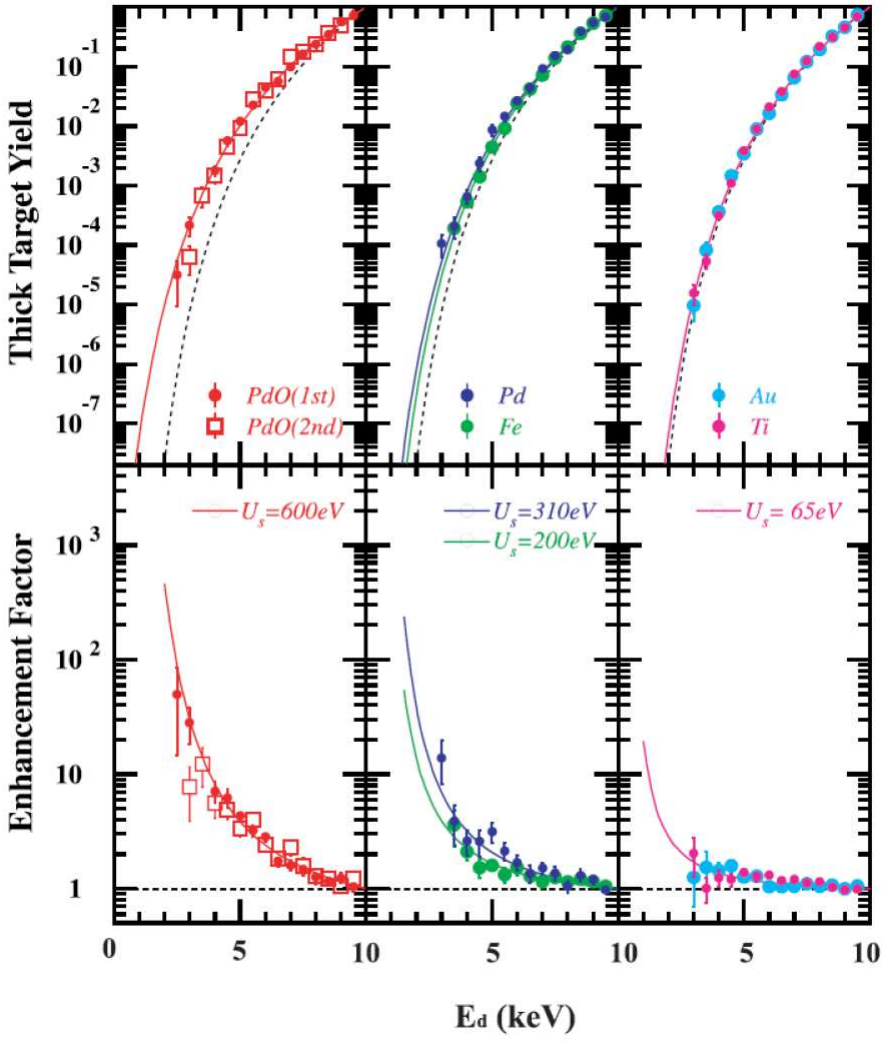

Fig.18 Yield of protons by irradiation of D ions to each metal[13].

Fig.18 [13] shows the yield of protons when D ions are implanted into each metal of PdO,

Pd, Fe, Au and Ti. The upper part of the figure plots the D ion yield versus Ed and the dotted line is the calculated value of the D-D nuclear fusion yield when there is no shielding effect. In the upper part of the figure, the D-D nuclear fusion yield relative to the energy Ed of the D ion is plotted by normalizing it with Ed = 10keV, and the dotted line is the calculated value of the D-D nuclear fusion yield when it is assumed that there is no shielding effect. The lower row shows the yield measurement divided by this dotted line value, and the solid line is the calculated value of yield taking into account the value of the shielding energy Us shown in the figure. Also in FIG. 19, the shielding energy Us is larger as the fusion probability increases.

As in Fig. 17, the lower the ion energy, the higher the rate of increase in the fusion probability, which indicates the nature of the Binary nuclear model. This phenomenon occurs even with a liquid metal having no crystal structure, so it is clearly another phenomenon different from that caused by the channeling phenomenon.

5-2) Experimental data suggesting detection of α by chain reaction

Fig.19 shows the yield of α rays with respect to the energy of irradiated ions when D ions are irradiated to Pd in which Li was dissolved as solid solution. The left side (a) shows Pd, the right side (b) shows Au, the solid line in the upper figure shows the relative excitation function normalized at 75keV, and the dotted line shows the standard calculated value[14].

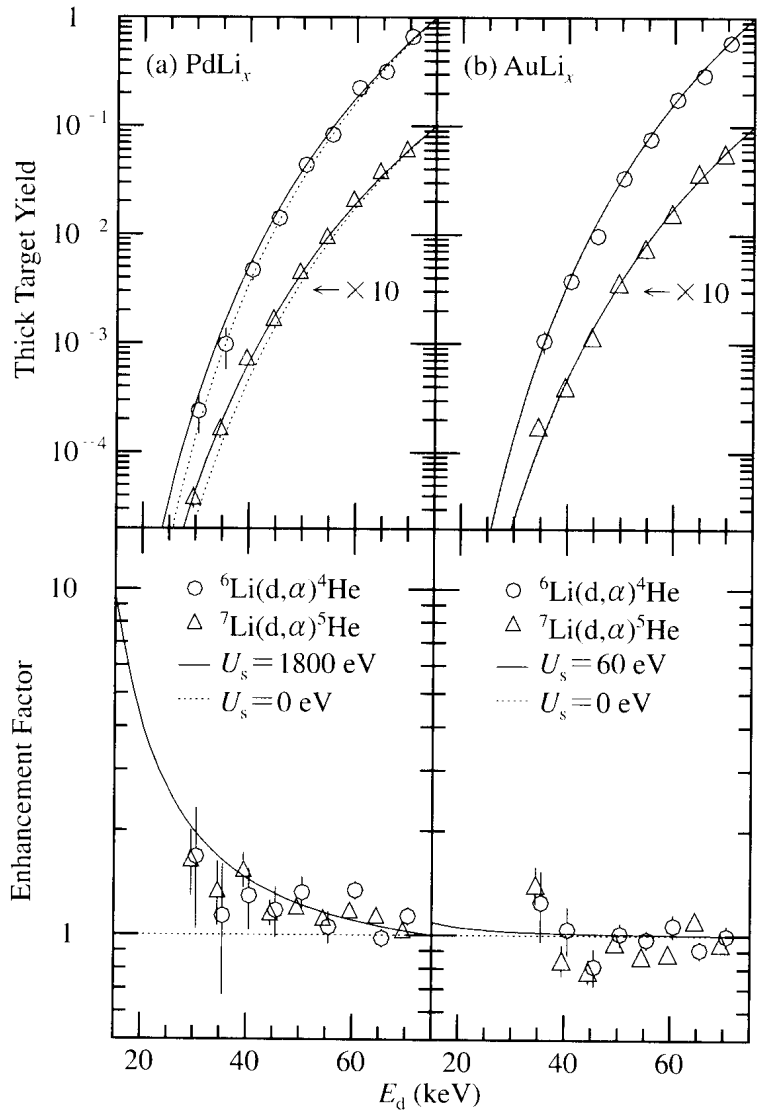

Fig. 19 Irradiation energy dependence of the yield of ^{6,7}Li (d, α) ^{4,5}Hereaction in metals[14].

The increase rate of Pd is 1800eV as the calculation result of the shielding energy and it is larger than 60 eV of Au and the nuclear fusion probability that exceeds the normal shielding effect is seen. I think this is because D concentration in the vicinity of the surface becomes thin enough to cause the channeling phenomenon due to the sample being placed in a vacuum, so that nuclear fusion chain reaction in metal crystal occurs, and the generated α rays are included.

5-3) Experimental example to suggest detection of particles by incomplete combustion

All of the irradiation D ions in the experimental examples in this section have energy

values of 120keV or more necessary for 3D fusion through the D-D binary nuclei. All of the ions that match the energy values of the triple fusion in these experiments are considered to be triple fusion through the binary nucleus. This is because it is unlikely that three nuclei are gathered in one place at the same time and become dense enough to cause nuclear fusion.

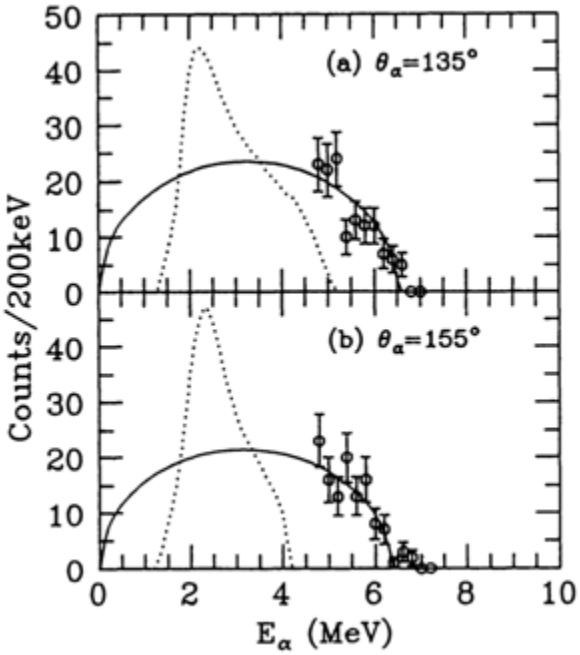

Fig.20 Spectrum of measured alpha line[15].

Fig.20 and 21 show the α-ray spectrum and the proton beam spectra of TiDx placed in a vacuum when irradiated with 150KeV deuteron beam. α rays of 4.5MeV or less are not detected by the setting of the detector. The angles described in (a), (b) and (c) are the detector's respect to the beam directions. The spectrum shown in (a) was measured with a 200-μm thick Al absorber, whereas the spectra in (b) and (c) were measured with a 15-μm one. The vertical axis is the count number of the detector. A rays of 4.5 MeV or less are not detected by the setting of the detector[15].

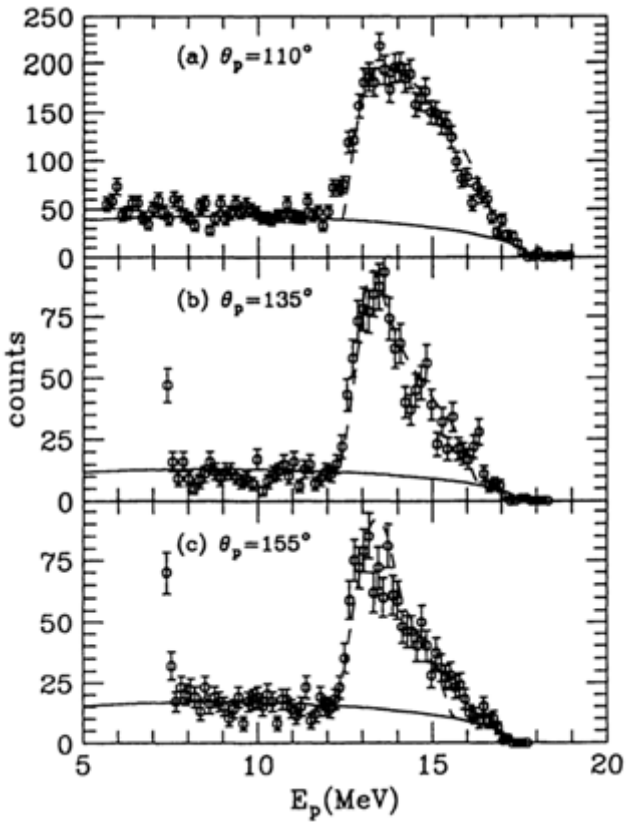

Fig.21 Spectrum of measured proton beam[15].

I will write my interpretation. Although the D concentration of the sample is increased by irradiating a large amount of deuteron beams, the concentration in the vicinity of the surface should be thin since the atmosphere is vacuum. In Fig.20, α (7.9MeV or less) of the equation (i) of triple nuclear fusion is considered, and in Fig.21, p (19.1MeV or less) of the equation (j) is considered. The reason why the maximum energies are low is considered to be that triple fusion does not occur because the D concentration on the surface part is small. The reason that the peak exists in the p ions of the equation (j) is considered that the reaction becomes active at the depth reachable of the p(3.0 MeV) ion beams generated by the reaction of the formula (a) by the 150KeV deuteron beam radiation. When p of 12MeV or less in Fig.19 is p (14.7MeV) of the reaction (e) of the secondary reaction of fusion, which occurs at above a certain concentration, is considered.

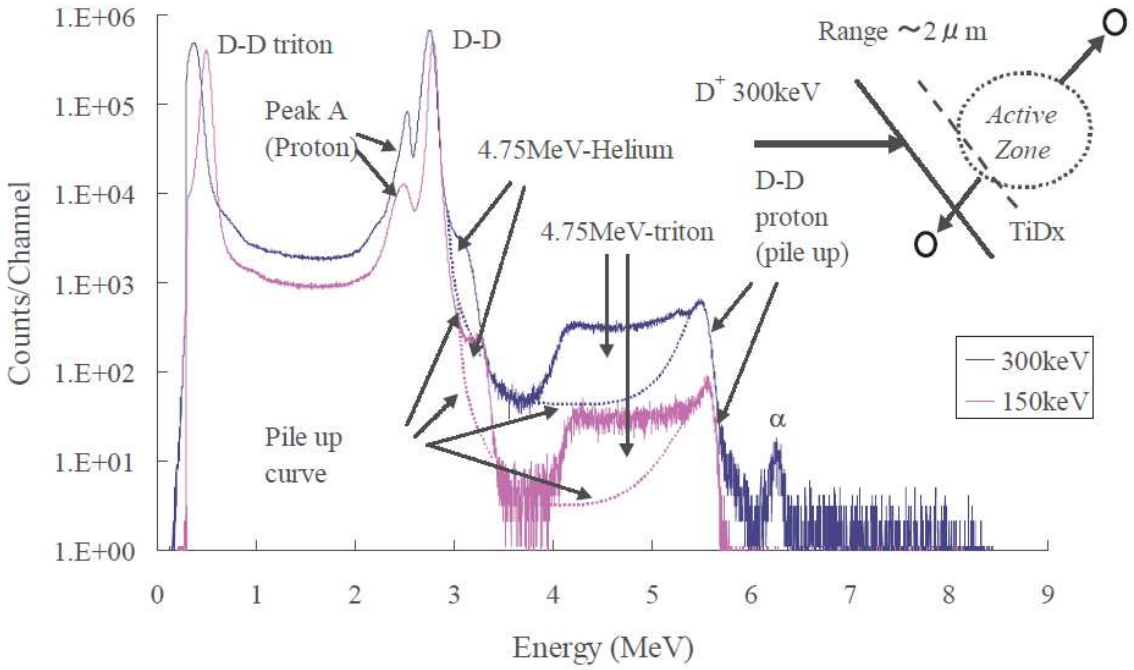

Fig.22 Charged-particles spectra emitted from TiDx sample implanted with 300keV-deuteron beam[11].

Fig.22 [11] [16] is the charged-particles spectra at 300KeV and 150keV deuteron beam irradiation for Au-coated TiDx. Since I think that the deuterium concentration is constant as it is coated with Au, I believe here 4.7MeV-Helium, 4.7MeV-triton is considered to represent ^{3}He (4.7MeV or less) and ^{3}H (4.7MeV or less) of 3D nuclear fusion according to the formula (h).

I think that the peak written as α of 6.2MeV is a beam emitted from a thin member because the width is narrow so that this is α (11.2MeV or less) of the equation (m), due to the nuclear fusion chain reaction derived from the thin D concentration Au coating part.

6) Combustion part of transmutation sample

The portion of the 1t pure Pd plate under the vacuum of the transmutation sample in Fig.8 becomes the α phase with a low D concentration. Although the lower part is a vacuum, since D permeations through the laminated structure part of Pd - CaO from the upper part, CaO acts as a flat orifice to suppress and equalize the D concentration. At the temperature of 80°C at which the transmutation becomes active, Pd becomes the α phase under the pressure of about 10^3 to 10^4Pa in the state diagram of Fig.9.

Since the distance that various ion beams emitted from the ignition portion can pass through Pd is about 10μm in consideration of stopping power, it is considered that the portion

of the Pd plate close to the laminated structure portion around the upper 10μm has an appropriate D concentration in the combustion portion and actively undergoes a chain reaction. This is because if an α ion beam is generated around this portion, it passes through Pd and the laminated portion of a thickness of 100 nm, and the α ion beam having energy of still 1MeV or more reaches the conversion nucleus of the surface layer.

Although the transmutation sample itself is small Pd plate 1cm^2 of 1t, the combustion part is only a part of it. From this, even if the portion satisfying the conditions of the chain reaction is small, it is possible to maintain the nuclear fusion chain reaction in metal crystal if at least continuous supply of the ion beam can be received.

The channeling phenomenon is more likely to occur in the crystal structure of the combustion part if there is no distortion, and the accuracy of centering also increases. The microstructure of the triangular groove formed on the surface has an effect of making it difficult for the combustion part to inflate and shrink due to phase transformation of Pd in the laminated portion, I think.

4. Transmutation

1) Transmutation when deuterium is introduced using D_2 gas

The Cs nucleus and the D-D binary nucleus have 55 times and twice the charge of hydrogen respectively. Therefore, in order for the D-D binary ion beam to approach the Cs atomic nucleus, it must exceed the 1100keV Coulomb barrier of 110 times the Coulomb barrier that it overcame during the D-D binary nucleus formation. The D ion beam having such high energy cannot be captured by the D nucleus, and the D-D binary ion beam is never formed. Therefore, I believe that D-D binary ion beams are not involved in transmutation.

The ion beam generated by the chain reaction is only α, and if α in the vicinity of 6.2MeV in Fig. 20 is regarded as an α ion generated by a chain reaction, it has sufficient energy to generate a conversion nucleus. Therefore, nuclear fusion with this α ion beam must explain the transmutation.

The surface layer of 40nm in which the nucleus that will undergo transmutation is implanted is in the α' phase with high D concentration, but the high energy α ion beam is subjected to the channeling phenomenon in the crystal lattice of Pd having heavy specific gravity, it goes through the road where the nucleus exists. The energy of the α ion beam that passed through the laminated part with a thickness of 100nm from the combustion part is still so large. It cannot be captured by the nuclear force of the D nucleus, but enters the Coulomb barrier of the nucleus that will undergo transmutation, represented by the Cs nucleus of atomic number 58 and is suitable for forming a binary nucleus. The Coulomb barrier of the

nucleus that will undergo transmutation becomes a larger sphere than the D nucleus, and the valley of the potential due to its nuclear power is deep. Therefore, it captures the α ion beam passes near a wider range, to form a binary nucleus.

In this way, mild nuclear fusion occurs via the binary nucleus with the α beam and transmutation occurs. Since the α nucleus is light to the nucleus that will undergo transmutation, the binary beam hardly moves, and this nucleus remains in a position susceptible to next α beam. As a result, mild nuclear fusion with the α beam occurs continuously, resulting in transmutation in which the nucleon at integer multiples of α nucleus increases.

The transmutation experiment[1] shows the following results.

133Cs→141Pr(+8)

138Ba→150Sm(+12)

137Ba→149Sm(+12)

182W→190Pt(+8)

186W→190Os(+4)

These transmutations can be thought to be due to the following continuous reaction.

$^{133}Cs + \alpha \rightarrow {}^{137}La$, $^{137}La + \alpha \rightarrow 141Pr$

$^{138}Ba + \alpha \rightarrow {}^{142}Ce$, $^{142}Ce + \alpha \rightarrow {}^{146}Nd$, $^{146}Nd + \alpha \rightarrow {}^{150}Sm$

$^{137}Ba + \alpha \rightarrow {}^{141}Ce$, $^{141}Ce + \alpha \rightarrow {}^{145}Nd$, $^{145}Nd + \alpha \rightarrow {}^{149}Sm$

$^{182}W + \alpha \rightarrow {}^{186}Os$, $^{186}Os + \alpha \rightarrow {}^{190}Pt$

$^{186}W + \alpha \rightarrow {}^{190}Os$

The reason why the transmutation from ^{133}Cs stops at ^{141}Pr is because ^{145}Pm is an unstable nucleus, and nuclear fusion does not occur because the weight increases as it changes to this nucleus.

Fig.23 shows the transmutation rate when experimental temperature and pressure are changed[1]. The reaction rate of 180 to 230kPa at 80°C is as large as 62% on average, indicating that extremely actively transmutation occurs.

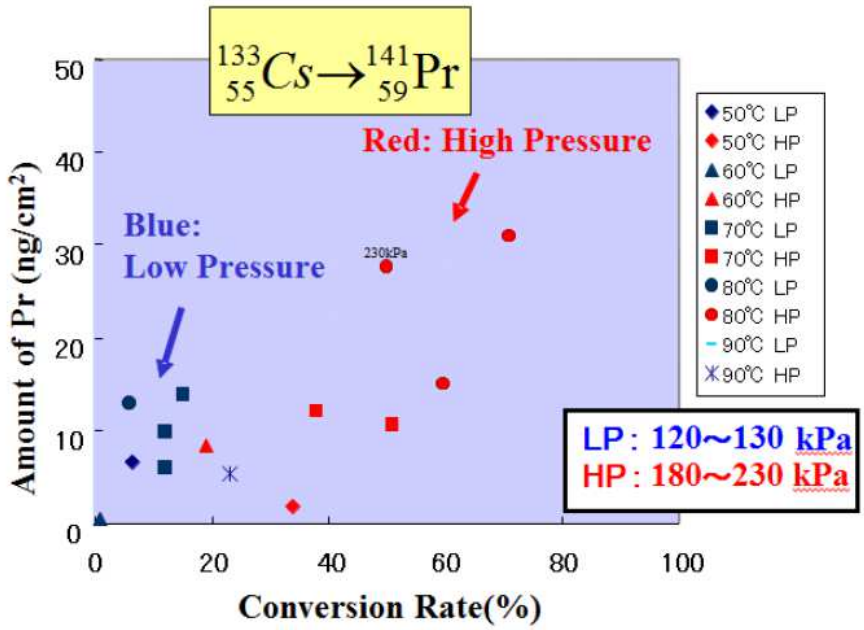

Fig.23 Dependence on D2 gas pressure in Pr production[1].

2) Transmutation when deuterium is introduced by electrolysis of heavy water

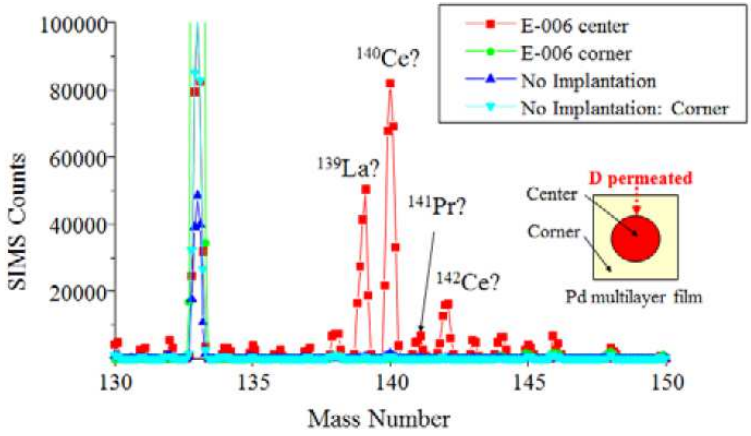

Magnified SIMS Spectra from mass 130 to mass 150 in a linear scale.

Fig.24 Comparison of SIMS Mass Spectra between E0006
and No Cs Impression sample[1].

Fig.24 shows the result of SIMS mass spectrometry of a sample into which deuterium was introduced by electrolysis of heavy water[1]. Transformed nuclei are confirmed at the center of the sample in which Cs is implanted, but the amount of conversion nuclei is very small. In addition, there are particularly few Pr, and various nuclides have been confirmed. In this experiment, perhaps trying to increase permeation D, the concentration of D was raised too

much, and the combustion part causing the chain reaction became far from the nucleus that will undergo transmutation, and it seems that α rays by chain reaction did not reach.

Although there is no directly comparable numerical value, it is considered that the number of converted nuclei is several orders of magnitude smaller than the conversion rate of 62% when D_2 gas is used. This difference indicates that the supply amount of the ion beam to the nucleus that will undergo transmutation is small. It is thought that the D concentration in the portion where the ion beam can reach is excessive, and there is no chain reaction occurring there.

However, it is still thought that D-D fusion of the equations (a) to (c) and triple nucleus fusion of the equations (h) to (j) occurred, receiving the supply of the ion beam from the ignition part. Then, the ion beam to be generated is 5 kinds of ^{3}He, ^{3}H, α, D plus a trace amount of p generated in the secondary reaction. It corresponds exactly to the measurement particle in Fig.20.

An example of a reaction for producing the nuclide described in Fig.24 from ^{133}Cs in 4 species except p is as follows.

(1) $\alpha + {}^{133}_{55}\mathrm{Cs} \rightarrow {}^{137}_{57}\mathrm{La}$

$\mathrm{D} + {}^{137}_{57}\mathrm{La} \rightarrow {}^{139}_{58}\mathrm{Ce} \rightarrow {}^{139}_{57}\mathrm{La} + e^+$

(2) $^3\mathrm{H} + {}^{133}_{55}\mathrm{Cs} \rightarrow {}^{136}_{56}\mathrm{Ba}$

$\alpha + {}^{136}_{56}\mathrm{Ba} \rightarrow {}^{140}_{58}\mathrm{Ce}$

(3) $2\alpha + {}^{133}_{55}\mathrm{Cs} \rightarrow {}^{141}_{59}\mathrm{Pr}$

(4) $\mathrm{D} + {}^{140}_{58}\mathrm{Ce} \rightarrow {}^{142}_{59}\mathrm{Pr} \rightarrow {}^{142}_{59}\mathrm{Ce} + e^+$

The reason why $^{141}_{59}$Pr is small in Fig. 24 seems to be that nuclear transformation to Nd occurs because the supply ratio of ion beams of ^{3}H, D and p is high unlike the chain reaction.

Fig.25 is a γ-ray spectrum at this time[1]. The γ ray at 511.5keV has a difference of 0.5KeV from γ ray 511.0KeV when electron-positron pair annihilation, but it agrees with that at the time when positron having kinetic energy annihilate. It is thought that there are some positrons in the generation reaction of various nuclides. For example, positrons are released by the reactions of (1) and (3) below.

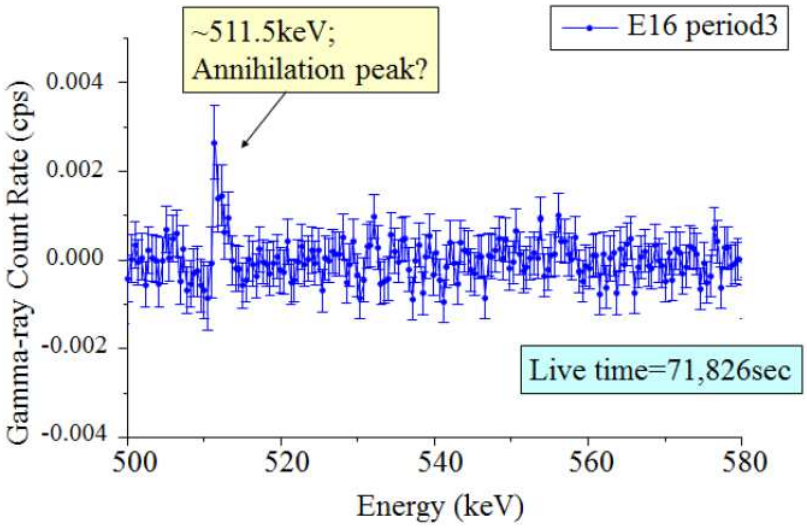

Gamma-ray Energy Spectrum emitted during Period 3

Fig.25 Gamma-ray Emissions during an electrochemically
D permission experiment E16[1].

3) Transmutation in the case where deuterium is introduced by electrolysis to a sample without Cs implanted

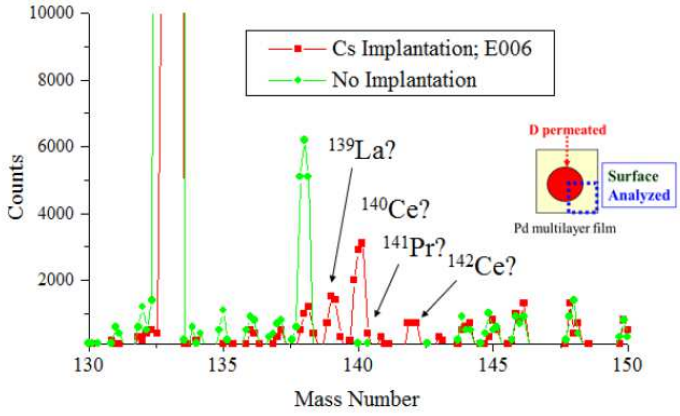

Fig.26 Comparison of ICP-MS Spectra between E006
and No Cs Implantation sample[1].

Fig.26 shows ICP-MS mass spectrometric analysis results of a sample planted with ^{133}Cs and a sample not planted when deuterium was introduced by electrolysis[1]. Although transmutation nucleus has been confirmed, the amount is one order of magnitude less than that of Fig.24 in the sample planted with ^{133}Cs. In the sample not planted with ^{133}Cs, almost

no nucleus with a mass number of 138 was detected in Fig.24, whereas in Fig.26 many of it were detected. Below, I will try to explain this result.

In the ICP-MS mass spectrometry, the surface layer of the sample is dissolved with nitric acid, and it is converted into a plasma and subjected to mass spectrometry. On the other hand, in SIMS mass spectrometry, mass spectrometry is performed by tapping out elements in a deeper position from the surface by argon sputtering on a narrow region. Therefore, ICP-MS mass spectrometry is analyzing the extreme surface portion of the sample, and SIMS mass spectrometry analyzes locally deeper points.

Even samples not planted with ^{133}Cs, since $CsNO_3$ is present in the electrolytic solution, ^{133}Cs adheres to the surface, which becomes nucleus that will undergo transmutation. Since these are only attached to the surface, if a He ion beam with two charges is taken in to form a binary nucleus, it moves away from the surface due to its momentum. If ^{3}H, D or p is taken in to form a binary nucleus, the nuclear fusion energy is large, so the magnetic lines of the binary nucleus strongly work, and since the momentum is small, it remains on the surface. In addition, Cs, Ba, La with high ionization tendency dissolves in the electrolyte from the surface when the electrolytic potential is lowered at the end of the experiment. However, since Cs is large in quantity, it remains on the surface. From these ideas, I think that the nuclide with mass number 138 is Ce and is generated by the following reaction.

(1) $^{3}H + {}^{133}_{55}Cs \rightarrow {}^{136}_{56}Ba$

$D + {}^{136}_{56}Ba \rightarrow {}^{138}_{57}La \rightarrow {}^{138}_{58}Ce + e^{-}$

5. Conclusion

The author was able to explain the excessive heat generation and all the results of transmutation experiments by this Nuclear Fusion Mechanism in Metal Crystals. This suggests that the nuclear fusion mechanism in metal crystals is correct. Below is a summary of the main points of this mechanism.

A) The α 'phase is the ignition part and the α phase is the combustion part.
Internal deformation such as phase transformation moves edge dislocation inside α' phase, causing abnormal accumulation of D, causing D-D fusion by tunnel effect. These ion beams enter the α phase part, and a chain reaction occurs. Therefore, it is necessary for the combustion part to be present in the range where the ion beams can reach.

B) The ion beams entering the α phase part lead to the D nucleus of the interstitial atoms by the channeling phenomenon and generate many D ion beams.

C) The D ion beam form a binary nucleus with the interstitial atom D, causing mild nuclear fusion and 4He is produced. This 4He takes in the D ion beam and becomes a

binary nucleus, and 6Li is generated. Furthermore, this 6Li takes in the D ion beam and becomes a binary nucleus, causing a 2α reaction, and a powerful α ion beams are generated. This α ion beams are again guided to the D nucleus of the interstitial atom, and many D ion beams are generated. These reactions constitute a nuclear fusion chain reaction in metal crystal.

D) The powerful α beam forms a binary nucleus with the nuclear that will undergo transmutation, and transmutation occurs by mild nuclear fusion.

E) In order for the fusion chain reaction to occur, it is necessary to have an appropriate D concentration.

F) When the D concentration is excessive, channeling phenomenon hardly occurs and it is difficult for a binary nucleus to be formed. And the binary ion beam just formed collides the other D nucleus, causing a normal D-D fusion reaction, and no chain reaction occurs. When a D ion beam of about 120keV or more is irradiated, the formed binary ion beam captures the D nucleus of interstitial atoms, and a triple nucleus fusion occurs. The fact that the particles generated in this case have already been confirmed is evidence of the existence of binary nuclei and binary ion beam.

References

[1] S. Tsuruga, T. Itoh, Y. Iwamura "Recent advances in transmutation experiments induced by deuterium permeation using Nano-Structured Pd/CaO/Pd Multilayer Thin Film" Proceedings JCF14-2, pp14-25(2013)

[2] Fleischmann, M., S. Pons, and M. Hawkins, "Electrochemically induced nuclear fusion of deuterium" J. Electroanal. Chem., 1989. 261: p. 301 and errata in Vol. 263.

[3] Naoko Takahashi, Satoru Kosaka, Tatsumi Hioki and Tomoyoshi Motohiro, Abstracts JCF13-7, December 8-9, 2012

[4] E. Wicke and H. Brodowsky "Hydrogen in metal II, G. Alefeld and J. Volkl, eds. (Springer, 1978), p.81

[5] Nelson Jarmie, “Low-Energy Nuclear Fusion Data and Their Relation to Magnetic and Laser Fusion” LA-8087 UC-34c Issued: April 1980.

[6] J.U. Andersen et al. "Kgl. Dausk Videnskab. Selskab, Mat.-Fys. Medd., 36(1967), No. 7

[7] T. Mizuno, “Cold fusion, Researchers' sufferings and achievements” Kohgaku-Sha Co., Ltd, Japan, 25/march/2005 P107-P113

[8] J. Kasagi, H. Yuki, T. Baba, T. Noda, T. Ohtsuki, A. G. Lipson, J. Phys. soc. Jpn. 71, 2881 (2002)

[9] F. Raiola et al, Eur. Phys. J. A 19, 283(2004)

[10] T. Mizuno, “Cold fusion, Researchers' sufferings and achievements” Kohgaku-Sha Co.,

Ltd, Japan, 25/march/2005 P117
[11] Sigeo Uneme, JCF2-20 OHP, October 21-22, 2000
[12] Naoto Takahashi et al. Nuclear Data News No.75(2003) - JAEA Nuclear Data Center
Original: M. Miyamoto, Y. Awa, N. Kubota, A. Taniike, Y. Furuyama, A. Kitamura: "Reaction yield enhancement under deuteron ion irradiation of deuterated Au/Pd sample" Proc. JCF4, pp.37-41, 2002
[13] J. Kasagi, H. Yuki, T. Baba, T. Noda, T. Ohtsuki, A. G. Lipson, J. Phys. soc. Jpn. 71, 2881 (2002)
[14] J. Kasagi, H. Yuki, T. Baba, T. Noda, J. Taguchi, M. Shimokawa, W. Galster, J. Phys. soc. Jpn. 73, 608 (2004)
[15] Jirohta Kasagi et al. "Energetic protons and α particles emitted in150- keV deuteron bombardment on deuterated Ti " J. Phys. Soc. Japan, 1995. 64(3): p. 777-783.
[16] Y. Isobe, Sigeo Uneme et al, JJAP 41 (2002) 1546.

Water Clusters Related to OHMASA-GAS

Hidemi Miura
Izumi-ku, Sendai. 981-3109, Japan

Abstract: One of the hydrogen-including oxy-hydrogen gases called OHMASA-GAS is obtained through the electrolysis of water under vibratory agitation by vibration blades. This gas has many useful properties such as being stored as the hydrogen (H) and oxygen (O) mixture gas. Furthermore, some noticeable phenomena have been reported that various elements seem to be generated under vibratory agitation of pure water or aqueous chloride solutions related to the generation of this gas. In order to investigate these properties and phenomena by computer simulations, OHMASA-GAS was supposed to be composed of water cage clusters which encapsulated H^+ ion, H_2 molecule and H atoms, and the generation of various elements under vibratory agitation was supposed to be caused by the collapse of spherical bubbles with nuclei of water cage clusters. While in the last study calculations have been carried out by only the computer simulation program MOPAC, in the present study almost all of the results of MOPAC were confirmed by another computer simulation program Quantum ESPRESSO.

Keywords: computer simulation, water cluster, OHMASA-GAS, generation of various elements

1. Introduction

OHMASA-GAS (Oxygen-Hydrogen Mixing Atomic Symmetrized Aeration-Gas) is one of the hydrogen-including oxy-hydrogen gases, which is obtained through the electrolysis of water under vibratory agitation by vibration blades. This gas can be stored as the hydrogen (H) and oxygen (O) mixture gas and has many other useful properties that some metals or glassy carbon melts instantly as if it vaporizes at high temperatures when it comes into contact with the flame of burning gas, and some new combustible compounds are formed when carbon dioxide (CO_2) is mixed with, and so on. Furthermore, related to the generation of this gas some phenomena have been reported that various elements seem to be generated under vibratory agitation of pure water or aqueous chloride solutions. These properties and phenomena related to OHMASA-GAS, which are described in Appendix-1, have been investigated through the view point of “water clusters” by computer simulations [1, 2]. Suppositions of generation processes of OHMASA-GAS and related phenomena for computer simulations, which are described in Appendix-2, are so difficult to solve that even in this study only some water clusters which occur on these supposed processes, such as water tube clusters, water cage clusters, water cage clusters which encapsulated H^+ ion, H_2 molecule and

H atoms, and high density water cage cluster, were considered.

While in the last study calculations have been carried out by the computer simulation program MOPAC (Molecular Orbital Program Package) of semi-empirical molecular orbital method, adding to it in the present study calculations were carried out by another computer simulation program Quantum ESPRESSO of the first principle molecular dynamics. Almost all of the simulation results of MOPAC were confirmed by Quantum ESPRESSO. The bonding energy per water molecule of water cage clusters ranging from about decamer to icosamer, which encapsulated H^+ ion, H_2 molecule and H atoms, became near to that of icosamer water cage cluster of regular dodecahedron which had been observed in the gas phase. From this point it can be interpreted that the water cage clusters which encapsulate H^+ ion, H_2 molecule and H atoms, the model of OHMASA-GAS, would stably exist in gas phase. Furthermore, high density water cage clusters, which were supposed to be made of pressurized water cage clusters in the collapsing bubbles, were simulated. As for the generation of various elements, collisions of the high density water cage clusters against the surface of palladium plating vibration blade would be investigated comparing to the other experiments of heavy water electrolysis, deuterium gas permeation, and so on.

2. Calculations

2.1 Hardware and Software Used for Calculation

Calculations were carried out on a personal computer which had 4 cores / 8 ways CPU with 32 GB main memory by using the computer simulation program MOPAC (Ver.6) based on the MP3 of semi-empirical molecular orbital method [3, 4] and Quantum ESPRESSO (Ver.5) based on the density functional theory of the first principle molecular dynamics [5]. These programs are working on the molecular computation support system program Winmostar™ [6] which assists in directly passing the optimized atomic coordinates calculated by MOPAC to Quantum ESPRESSO, in exchanging atomic kinds and changing atomic coordinates, and in immediately showing structures of water clusters and outputting graphics of calculated spectra, and so on.

2.2 Calculated Water Clusters

OHMASA-GAS and the neutral aqueous electrolyte would be generated when the spherical bubbles with the nuclei of small water cage clusters flow to electrodes of electrolysis [Appendix-2 a) and b)]. Various elements would be generated when the spherical bubble with a nucleus of small water cage cluster on the surface of vibration blade collapses and when this small water cage cluster collides on the surface of vibration blade and is pressed to form high density water cage cluster [Appendix-2 c)]. In order to check the structural optimization and

infrared absorption spectra calculated by MOPAC, infrared absorption and Raman scattering spectra were calculated by Quantum ESPRESSO. Calculated water tube clusters and water cage clusters, which were classified by shape of cross section or surface pattern, are shown in Appendix-3. Examples of the optimized structures of water tube clusters and water cage clusters calculated by MOPAC are shown in Appendix-4.

a) Water Tube Clusters

Water sheet clusters would be formed on the pressurized surfaces of vibration blades under vibratory agitation. When the vibration blade moves in the opposite direction, large water tube clusters would be made of the water sheet clusters which are partly peeled off by water streams under vibration agitation. The water tube clusters, which were formed by bonding several cross sections of pentamer and hexamer, were calculated.

In the case of vibratory agitation of the aqueous electrolyte solutions with alkali or alkaline-earth metal or other metal, the metal atom would bond to the surface of water tube clusters. Calculations were carried out for aqueous $MgCl_2$ solution.

b) Water Cage Clusters

When the large water tube clusters are divided into the decamer, pentadecamer or icosamer base small water cage clusters, spherical bubbles with the nuclei of these water cage clusters would be formed. Adding to the decamer of cubic ice structure (Ⅰc phase ice) and the icosamer of regular dodecahedron, the water cage clusters formed by bonding a few cross sections of trimer, tetramer, pentamer and hexamer were calculated.

OHMASA-GAS would be generated when the spherical bubbles with the nuclei of water cage clusters flow to electrodes of electrolysis and when H^+ ion, H_2 molecule and H atoms are encapsulated in the water cage clusters or O atom bond to them as hydrogen peroxide (H_2O_2), and the neutral aqueous electrolyte would be generated when chlorine (Cl) atom is bonded to them as hypochlorous acid (HClO). As for the states of encapsulated H^+ ion, H_2 molecule and H atoms the overall water cage clusters were calculated, and as for the states of bonding O or Cl atom the decamer water cage clusters of cubic ice structure were calculated.

c) High Density Water Cage Clusters

When the vibration blade moves in the opposite direction again, some spherical bubbles collapse near the pressurized surface of the vibration blade. The impacts of collapsing bubbles propagate to the other spherical bubbles staying on the surface of the vibration blades and cause them to violently collapse. The water cage cluster of nucleus in the collapsing spherical bubble would be pressed by water molecules which flow into the collapsing spherical bubble to become high-temperature and high-pressure. The water state of a high-pressure of several giga-pascals at normal temperature is Ⅶ phase ice formed by inserting the cubic ice of Ⅰc phase into the cubic ice. The pentadecamer water cage cluster, the structure of which was this

mutually inserting cubic ice, was calculated.

In the case of vibratory agitation of aqueous chloride solutions with alkali or alkaline-earth metal or other metal, the metal atom would bond to the surface of water tube clusters which would be divided into the water cage clusters. Calculations were carried out for the case of aqueous $MgCl_2$ solution.

3. Results and Discussion

Calculations of almost all of the water clusters using MOPAC were carried out by Quantum ESPRESSO. In those cases, SCF (Self Consistent Field) calculations in Quantum ESPRESSO were converged with the optimized atomic coordinates calculated by MOPAC, and infrared absorption and Raman scattering spectra were calculated by Quantum ESPRESSO.

All of the infrared absorption wavenumbers of water clusters, which are calculated by MOPAC after the structural optimization of water clusters, were positive. However, the peaks of wavenumbers ranging from about 0 to 800 /cm calculated by MOPAC became negative in the infrared absorption and Raman scattering spectra calculated by Quantum ESPRESSO, which used the same optimized atomic coordinates of water clusters calculated by MOPAC. Although it would be partly recognized that the structural optimization of water clusters by using MOPAC were not perfectly calculated, it would be also recognized that the vibrations of small wavenumbers ran off the harmonic oscillations due to the non-harmonic terms of the pseudopotentials used by Quantum ESPRESSO for the vibration analysis.

Hydrogen bonds for the formation of water clusters have each H atom between tow O atoms, and H atoms of Hydrogen bonds are thought to change positions in about 10-20 psec. These times correspond to the spectral wavenumbers of about 300-150 /cm, so that the vibrations of wavenumbers ranging from about 0 to 800 /cm of water clusters would be considered to lose the restoring forces by hydrogen bonds.

Furthermore, the sharp peaks of bending modes of water (H_2O) molecules appear at wavenumbers of about 1700 /cm and the sharp peaks of stretching modes of H_2O molecules appear at wavenumbers of about 3800-4000 /cm in the infrared absorption spectra calculated by MOPAC respectively, but those peaks spread out in the infrared absorption and Raman scattering spectra calculated by Quantum ESPRESSO due to the coupling between the bending and stretching vibrations each other.

3.1 Water Cage Clusters

Infrared absorption and Raman scattering spectra of decamer and icosamer water cage clusters which capsulate H^+ ion, H_2 molecule and $H3^+$ ion (H^+ ion and H_2 molecule or two H atoms) are shown for examples as follows.

a) Decamer Water Cage Cluster which Encapsulates H^+ Ion

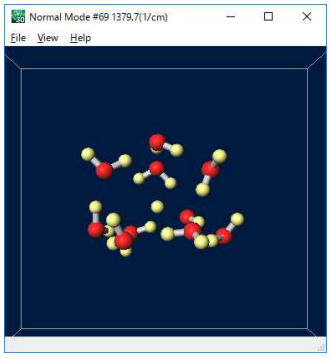

Fig. 1-a: $H^+@(H_2O)_{10}$
The red and yellow spheres represent the O and H atoms, respectively.

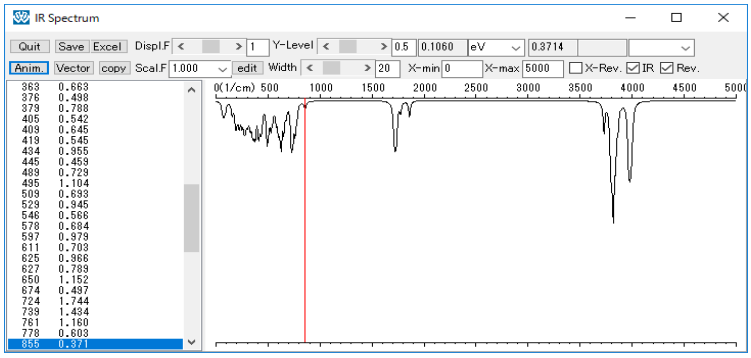

Fig. 1-b: Spectrum of $H^+@(H_2O)_{10}$ by MOPAC
Infrared absorption
Red vertical line indicates the oscillation of H+ ion.

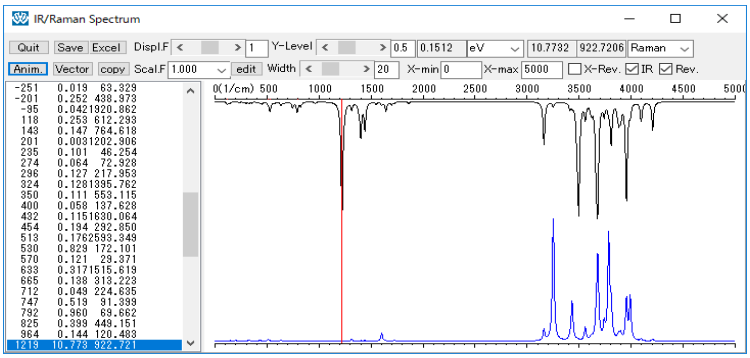

Fig. 1-c: Spectra of $H^+@(H_2O)_{10}$ by Quantum ESPRESSO
Upper: Infrared absorption, Lower: Raman scattering
Red vertical line indicates the oscillation of H+ ion.
Large peak appears in the infrared absorption due to the coupling of oscillation of H^+ and bending vibrations of H_2O molecules.

When one H^+ ion is encapsulated in the decamer water cage cluster, the oscillation of it appears at a wavenumber of about 1000 /cm [Fig. 1-b, c]. In the infrared absorption spectra calculated by Quantum ESPRESSO [upper on Fig. 1-c], the large sharp peak of oscillation of one H^+ ion appears due to the coupling to the bending vibrations of H_2O molecules.

b) Decamer Water Cage Cluster which Encapsulates H_2 Molecule

When two H atoms are encapsulated in the decamer water cage cluster as one H_2 molecule, the weak vibration of the H_2 molecule, two H atoms move against one another, appears at a wavenumber of about 4500 /cm, which is originally infrared inactive [Fig. 2-b, c].

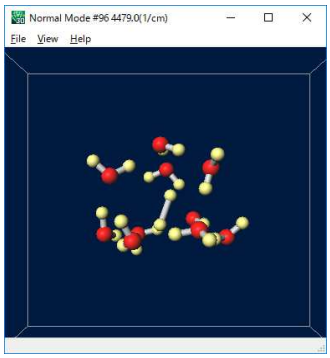

Fig. 2-a: $H_2@(H2O)_{10}$
The red and yellow spheres represent the O and H atoms, respectively. The H_2 molecule expands in its vibration.

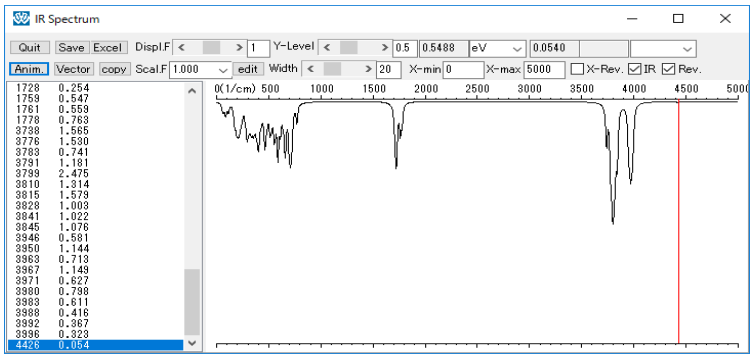

Fig. 2-b: Spectrum of $H_2@(H_2O)_{10}$ by MOPAC
Infrared absorption
Red vertical line indicates the vibration of H_2 molecule, two H atoms move weakly against one another.

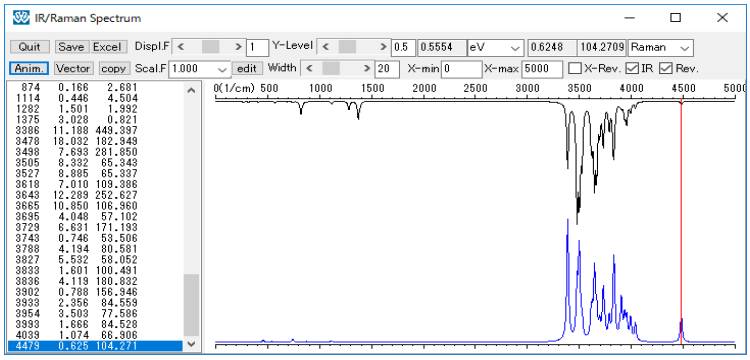

Fig. 2-c: Spectra of $H_2@(H_2O)_{10}$ by Quantum ESPRESSO
Upper: Infrared absorption, Lower: Raman scattering
Red vertical line indicates the vibration of H_2 molecule, two H atoms move against one another.

c) Decamer Water Cage Cluster which Encapsulate H^+ Ion and Two H Atoms in a Slightly Curved Line Structure

When one H^+ ion and two H atoms are encapsulated as H_3^+ ion in a slightly curved line structure in the decamer water cage cluster, the stretching vibration of the both ends of H atoms or H^+ ion appears at a wavenumber of about 2500-3000 /cm, which is originally infrared inactive [Fig. 3-b, c]. The vibration of the center H atom or H^+ ion against the both ends of H atoms or H^+ ion which appears strongly at a wavenumber of about 2500 /cm as a sharp peak in the infrared absorption spectrum calculated by MOPAC spreads out in the infrared absorption and Raman scattering spectrum calculated by Quantum ESPRESSO [Fig. 3-c].

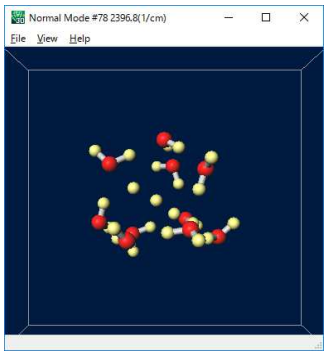

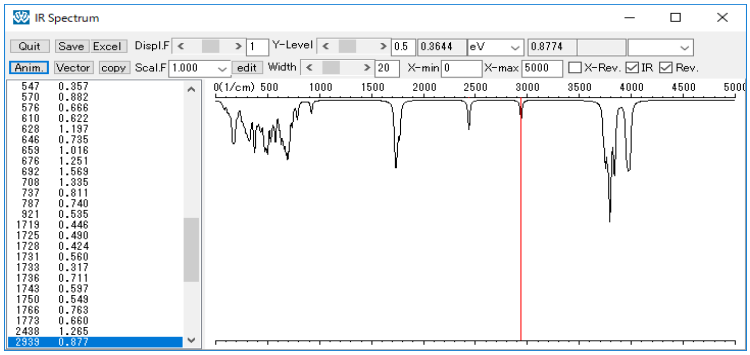

Fig. 3-a: H_3^+l@(H2O)10
The red and yellow spheres represent the O and H atoms, respectively. The H_3^+ ion expands in its vibration.

Fig. 3-b: Spectrum of H_3^+l@$(H_2O)_{10}$ by MOPAC
Infrared absorption
Red vertical line indicates the stretching vibration of the both ends of H atoms or H^+ ion.

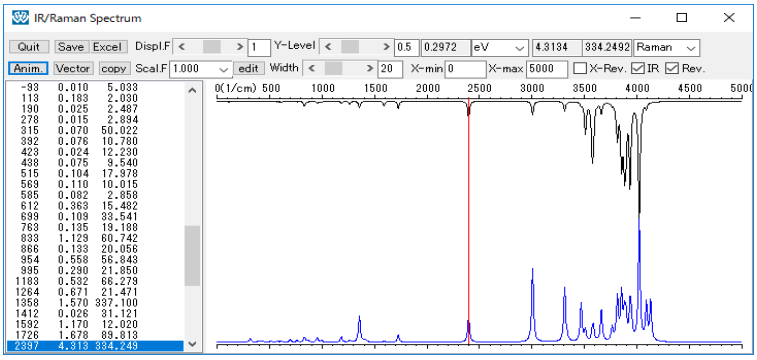

Fig. 3-c: Spectra of H_3^+l@$(H_2O)_{10}$ by Quantum ESPRESSO
Upper: Infrared absorption, Lower: Raman scattering
Red vertical line indicates the stretching vibration of the both ends of H atoms or H^+ ion.

d) Decamer Water Cage Cluster which Encapsulates H^+ Ion and H_2 Molecule in a Triangle Structure

When one H^+ ion and one H_2 molecule are encapsulated as H_3^+ ion in a triangle structure in the decamer water cage cluster, an oscillation of the whole H_2 molecule appears at a wavenumber of about 1000 /cm and another oscillation of the H^+ atom appears at a wavenumber of about 1200 /cm [Fig. 4-b], both of which separate to a few of peaks in the infrared absorption and Raman scattering spectrum calculated by Quantum ESPRESSO [Fig. 4-c]. Furthermore, a weak vibration of H_2 molecule, two H atoms move against one another, appears at a wavenumber of about 4400-4900 /cm, which is originally infrared inactive [Fig. 4-b, c].

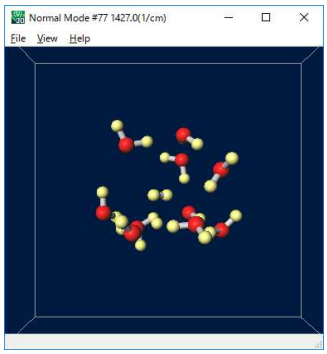

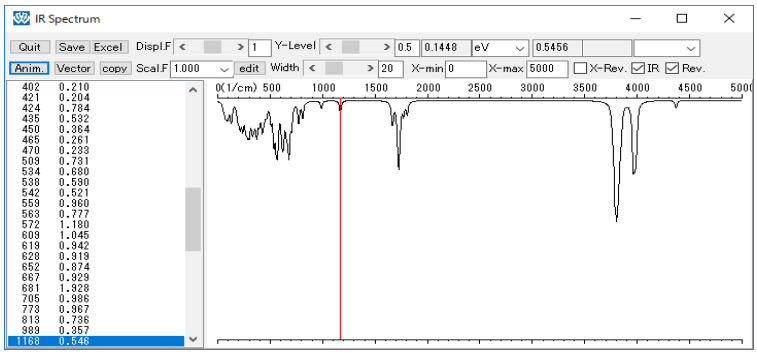

Fig. 4-a: $H_3^+t@(H2O)10$
The red and yellow spheres represent the O and H atoms, respectively.

Fig. 4-b: Spectrum of $H_3^+t@(H_2O)_{10}$ by MOPAC
Infrared absorption
Red vertical line indicates the oscillation of the H^+ atom.

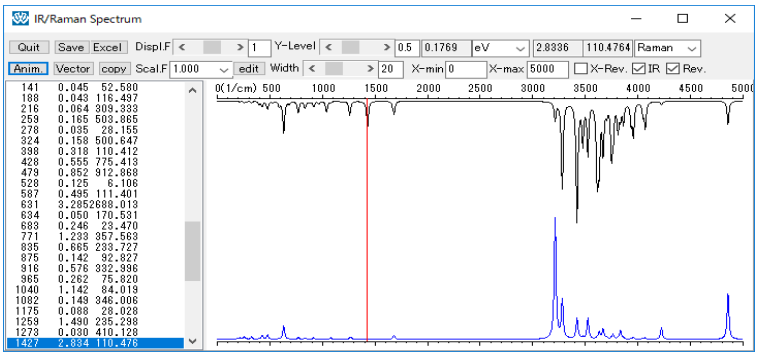

Fig. 4-c: Spectra of $H_3^+t@(H_2O)_{10}$ by Quantum ESPRESSO
Upper: Infrared absorption, Lower: Raman scattering
Red vertical line indicates the oscillation of the H^+ atom.

e) Icosamer Water Cage Cluster which Encapsulates H_2 Molecule

When two H atoms are encapsulated in the icosamer water cage cluster as one H_2 molecule, the weak vibration of the H_2 molecule, two H atoms move against one another, appears at a wavenumber of about 4500-4800 /cm, which is originally infrared inactive [Fig. 5-b, c]. Similar calculations on the henicosamer water cage cluster were carried out, which encapsulated one H_2O molecule in the icosamer water cage cluster. However, SCF calculations converge on both icosamer and henicosamer water cage clusters which encapsulate only one H_2 molecule.

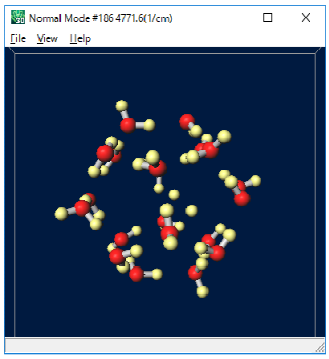

Fig. 5-a: $H_2@(H2O)_{20}$
The red and yellow spheres represent the O and H atoms, respectively.

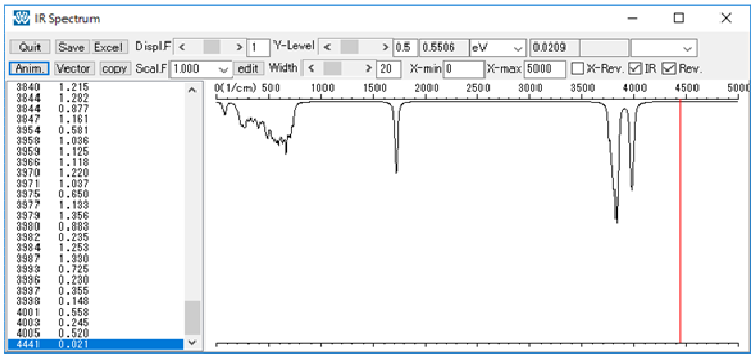

Fig. 5-b: Spectrum of $H_2@(H_2O)_{20}$ by MOPAC
Infrared absorption
Red vertical line indicates the vibration of H_2 molecule, two H atoms move against one another.

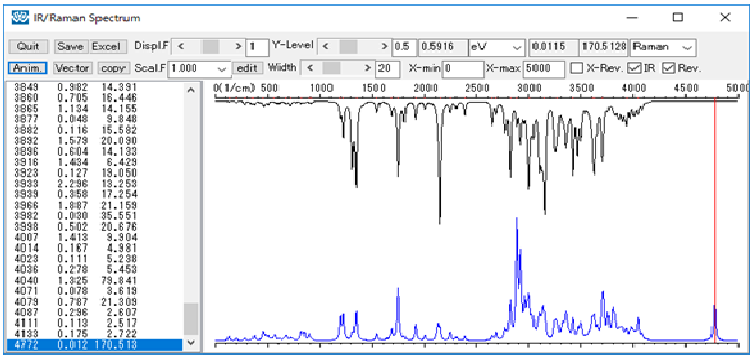

Fig. 5-c: Spectra of $H_2@(H_2O)_{20}$ by Quantum ESPRESSO
Upper: Infrared absorption, Lower: Raman scattering
Red vertical line indicates the vibration of H_2 molecule, two H atoms move against one another.

3.2 Bonding Energy per Water Molecule of Water Cluster

The bonding energy per water molecule of the water tube clusters is larger (negative absolute value is smaller) than -25kJ/mol [Fig. 6], which is nearly same value of those of the water cage clusters of no encapsulated H^+ ion or H_2 molecule and H atoms reported last time [2]. On the other hand, when H^+ ion or H_2 molecule and H atoms are encapsulated in the water cage clusters, some bonding energy per water molecule of them decreases (negative absolute value increases) smaller (negative absolute value is larger) than -25kJ/mol [Fig. 7]. Since the bonding energy per water molecule of the icosamer water cage cluster of regular dodecahedron, which has observed in gas phase, is -26.5kJ/mol by calculation, some water cage clusters which encapsulate one H^+ ion or H_2 molecule and H atoms (especially one H^+

ion and two H atoms in the slightly curved line), bonding energy per water molecule of which becomes smaller (negative absolute value is larger) than -25kJ/mol, would be presumed to stably exist in gas phase.

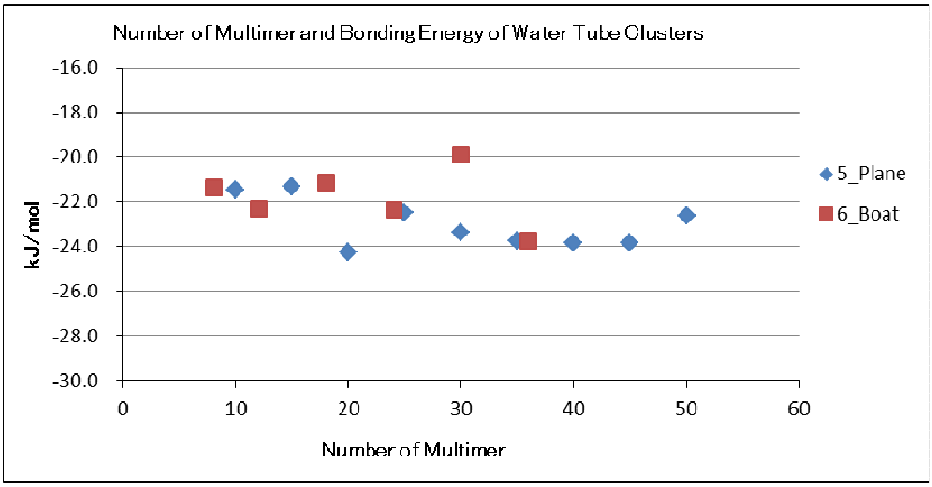

Fig. 6 Number of Multimer and Bonding Energy per Water Molecule of Water Tube Clusters

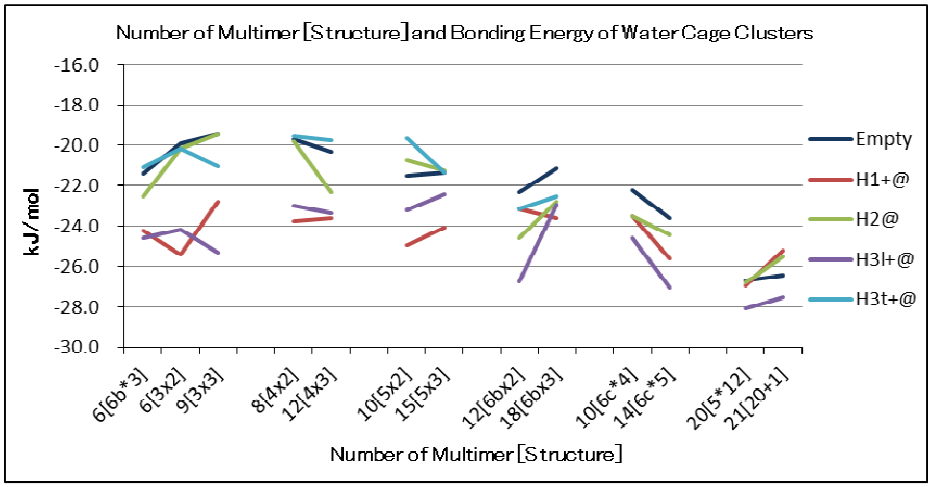

Fig. 7 Number of Multimer [Structure] and Bonding Energy per Water Molecule of Water Cage Clusters which encapsulate H^+ ion or H_2 molecule and/or H atom

3.3 Generation of Elements under Vibratory Agitation

It has been reported that various elements are generated under vibratory agitation of the pure water or the aqueous electrolyte solutions like magnesium chloride ($MgCl_2$) by palladium (Pd) plating vibration blades with a frequency of about 160 Hz. Some elements which have been analyzed by ICP (Inductively Coupled Plasma) atomic emission spectrometer are shown in Appendix-5. It would be recognized that many elements are generated in some mechanisms

under vibratory agitation with respect to each element of aqueous chloride solutions because the amount of generation elements increases while the remaining amount of solute elements decreases, the kind or the amount of generation elements changes as the kind of solute elements changes, and the amount of generation elements increases as the additive tritiated water replaces heavy water.

However, almost all of these generation elements are included in the materials of such as used instruments, experimental apparatuses or surrounding objects, so the aqueous electrolyte solutions might be possibly contaminated by some elements through the top of opened vibratory agitation tank. Furthermore, since these generation of elements under vibratory agitation are supposed to be caused by collapses of bubbles with nuclei of water cage clusters [Appendix-2], it would be possible that the impacts of collapsing bubbles propagate in the aqueous electrolyte solutions to clean up or shave off the surface of used instruments or experimental apparatuses, then some materials of them dissolve in the aqueous electrolyte solutions.

Nevertheless, the amount of generation elements under vibratory agitation of the aqueous magnesium chloride ($MgCl_2$) solution seems to be much larger than that of the other aqueous electrolyte solutions. Especially, phosphorus (P) is considered to be significantly much generated even if some amount of it is contaminated as much as whole amount of the other generation element copper (Cu) or silver (Ag) is contaminated. Since nuclear transmutations which increase atomic number four or so have been reported in some experiments or theories, this generation of P from Mg, which does not increase atomic number four but three, would have to be investigated.

a) Formation of High Density Water Cage Cluster

When some spherical bubbles collapse near the surface of the vibration blade, the impacts of collapsing bubbles would propagate to the other spherical bubbles staying on the surface of the vibration blade and cause them to violently collapse. Then the nucleus of collapsing bubble would be pressed by water molecules which flow into the bubble to form the high density water cage cluster. As for the high density water cage cluster, the water of structure of Ⅶ phase ice, that is, the cubic ice of Ⅰc phase mutually inserts into the cubic ice, is considered. Calculations were carried out on the pentadecamer water cage cluster composed by the decamer and inserting pentamer.

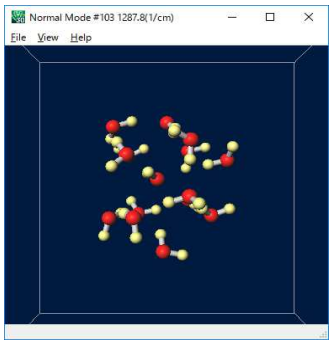

Fig. 8-a: $(H2O)_{15}$
The red and yellow spheres represent the O and H atoms, respectively.

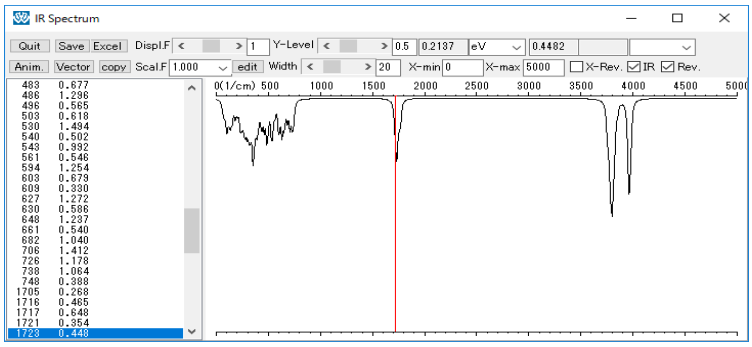

Fig. 8-b: Spectrum of $(H_2O)_{15}$ by MOPAC
Infrared absorption
Red vertical line indicates the bending vibration of H_2O molecules.

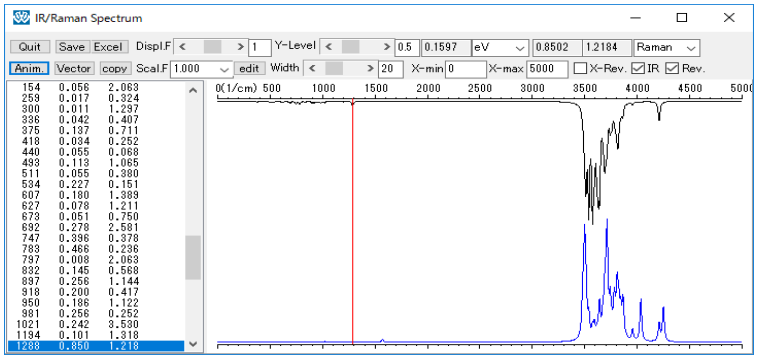

Fig. 8-c: Spectra of $(H_2O)_{15}$ by Quantum ESPRESSO
Upper: Infrared absorption, Lower: Raman scattering
Red vertical line indicates the bending vibration of H_2O molecules.

In the case of vibratory agitation of the aqueous $MgCl_2$ solution, Mg atom would bond to the surface of high density water cage cluster as MgO molecule. Infrared absorption and Raman scattering spectra of pentadecamer high density water cage cluster without or with MgO molecule on the surface of it calculated by MOPAC and Quantum ESPRESSO are shown as follows.

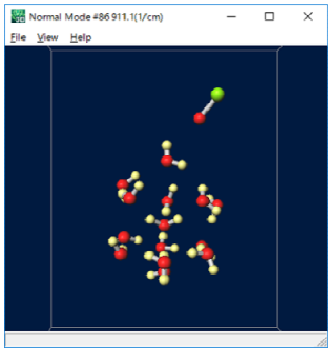

Fig. 9-a: $(H2O)_{14}$+MgO
The red, yellow and green spheres represent the O, H and Mg atoms, respectively.

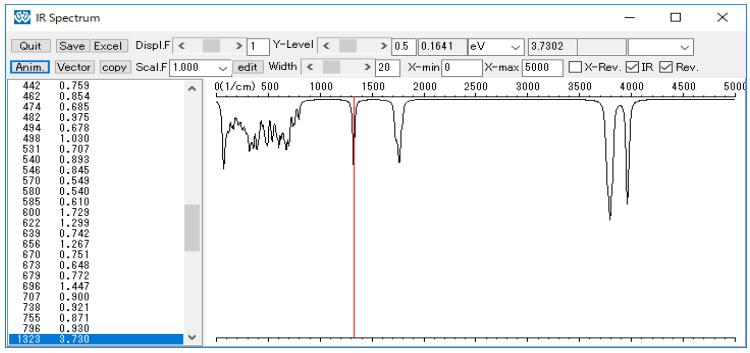

Fig. 9-b: Spectrum of $(H_2O)_{14}$+MgO by MOPAC
Infrared absorption
Red vertical line indicates the stretching vibration of MgO molecules.

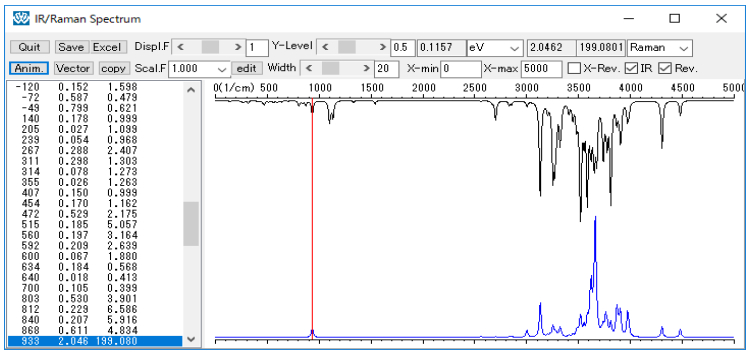

Fig. 9-c: Spectra of $(H_2O)_{14}$+MgO by Quantum ESPRESSO
Upper: Infrared absorption, Lower: Raman scattering
Red vertical line indicates the stretching vibration of MgO molecules.

b) Collision of High Density Water Cage Cluster against the Surface of Vibration Blade

It would be considered that the high density water cage cluster formed by the collapse of spherical bubble staying on the Pd plating surface of vibration blade collide against it at high speed.

When the high density water cage cluster collide against the surface of vibration blade in a vacuum, some of H atoms and O atoms which compose the high density water cage cluster or the metal atom which bonds to it would be diffused on or scattered from the surface of vibration blade due to the forces acting on them to different directions. However, when it collide against the surface of vibration blade in the aqueous electrolyte solutions, H atoms and O atoms which compose it or metal atom which bonds to it would collide against the surface

of the vibration blade almost perpendicularly due to the forces cancelled out each other to different directions by surrounding water molecules which flow into the collapsing bubble.
Since a jet stream of water through the collapsing bubble is recognized to flow at high speed of the order of 100 m/s, the high density water cage cluster would be simulated to collide perpendicularly on the Pd plating vibration blade at about the same speed in the imaging model shown as follows. In the same computer simulation methods, when the speed of collision is changed, the other experiments such as heavy water electrolysis, deuterium gas permeation, and so on would be similarly simulated.

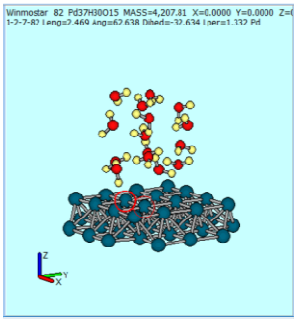

Fig. 10-a: $(H2O)_{15} \rightarrow Pd_{37}$

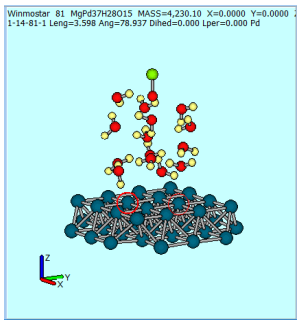

Fig. 10-b: $(H2O)_{14}+MgO \rightarrow Pd_{37}$

The red, yellow, blue and green represent the O, H, Pd and Mg atoms, respectively.

4. Summary

While in the last study calculations have been carried out by the computer simulation program MOPAC of semi-empirical molecular orbital method, adding to it in the present study calculations were carried out by another computer simulation program Quantum ESPRESSO of the first principle molecular dynamics. Almost all of the simulation results of MOPAC were confirmed by Quantum ESPRESSO. In those confirmable cases, SCF calculations in Quantum ESPRESSO were converged with the optimized atomic coordinates calculated by MOPAC, and infrared absorption and Raman scattering spectra were calculated.
The bonding energy per water molecule of water cage clusters ranging from about decamer to icosamer, which encapsulated H^+ ion, H_2 molecule and H atoms, became near to that of icosamer water cage cluster of regular dodecahedron which had been observed in the gas phase. From this point it can be interpreted that the water cage clusters which encapsulate H^+ ion, H_2 molecule and H atoms, the model of OHMASA-GAS, would stably exist in gas phase.
The amount of generation elements under vibratory agitation of the aqueous magnesium chloride ($MgCl_2$) solution seems to be much larger than that of the other aqueous electrolyte solutions. Especially, P is considered to be significantly much generated even if some amount

of it is contaminated as much as whole amount of the other generation element Cu or Ag is contaminated. As for the generation of elements, collisions of the high density water cage clusters, which are supposed to be made of pressurized water cage clusters in the collapsing bubbles, against the surface of palladium plating vibration blade would be investigated comparing to the other experiments of heavy water electrolysis, deuterium gas permeation, and so on.

Acknowledgements

The author wishes to thank Japan Techno Co., Ltd. for providing many valuable data about OHMASA-GAS and related phenomena.

References

1) H. Miura, States of Hydrogen, Oxygen or Magnesium Atom in or with Cubic Ice Crystal-like Water Clusters, Proc. of ICCF20, 327 (2016).
2) H. Miura, Model Mechanism of OHMASA-GAS Related to Water Clusters, Proc. of JCF17, 68 (2017).
3) J. J. P. Stewart, Frank J. Seiler Research Laboratory, U.S. Air Force Academy, Colorado Springs, Colorado 80840-6528, USA.
4) J. J. P. Stewart, J. Compt. Chem. 10, **209**, 221 (1989).
5) P. Giannozzi, S. Baroni, N. Bonini, M. Calandra, R. Car, C. Cavazzoni, D. Ceresoli, G. L. Chiarotti, M. Cococcioni, I. Dabo, A. Dal Corso, S. de Gironcoli, S. Fabris, G. Fratesi, R. Gebauer, U. Gerstmann, C. Gougoussis, A. Kokalj, M. Lazzeri, L. Martin-Samos, N. Marzari, F. Mauri, R. Mazzarello, S. Paolini, A. Pasquarello, L. Paulatto, C. Sbraccia, S. Scandolo, G. Sclauzero, A. P Seitsonen, A. Smogunov, P. Umari, R. M Wentzcovitch, Quantum ESPRESSO: a modular and open-source software project for quantum simulations of materials, Journal of Physics: Condensed Matter, **21** (39), 395502 (2009).
6) N. Chida, Development of molecular computation support system Winmostar, Idemitsu technical report, **49**, 106 (2006).

Appendix-1 Properties and Phenomena

Properties of OHMASA-GAS and neutral aqueous electrolyte, and phenomena related to the generation of OHMASA-GAS are as follows:

a) Properties of OHMASA-GAS

・ OHMASA-GAS is obtained through electrolyzing of water added like potassium hydroxide (KOH) under vibratory agitation by vibration blades with a frequency of about 40Hz.

・ This gas is made of mixing the gas including hydrogen (H) from cathodes and oxygen (O) from anodes as bubbles of sizes ranging from about 5 to 700 nm without separators, respectively, and can be stored at high pressure.

・ This gas is stored in stainless bottles without hydrogen embrittlement.

・ This gas is liquefied at a temperature of -178.7°C (oxygen: -183°C, hydrogen: -252.6°C), but it is not solidified at a temperature of -255°C (oxygen: -218.4°C, hydrogen: -259°C) even at a pressure of 25 MPa.

・ This gas does not show H_2 peak of a wavenumber of about 4200 /cm in Raman spectrum, while it shows O_2 peak of a wavenumber of about 1600 /cm.

・ This gas is composed of the multimer water clusters of number ranging from about 10 (decamer) to 20 (icosamer), the mode of which is around 14 or 15 and the maximum is 27 according to the analyzation by a liquid-ionization tandem mass spectrometry.

・ This gas burns in the same way as H gas, but it is safety, for example, without explosion inhaling the flame.

・ Titanium (Ti), tantalum (Ta), tungsten (W) metal or glassy carbon (C) melts and vaporizes instantly at a temperature of about 3000°C or over when it comes into contact with the flame of burning this gas of a temperature of 600-700°C. Aluminum (Al) metal of high thermal conductivity only melts down.

・ Carbon dioxide (CO_2) forms new combustible compounds by mixing with this gas.

・ Hydrocarbon such as LNG (liquefied natural gas; mainly methane CH_4) and propane (C_3H_8) improves combustion efficiency by mixing with this gas.

・ An early voltage of fuel cell with this gas is about 5% higher than that with only H gas, however it descend at a temperature higher than 60°C.

・ When H gas is added to this gas, the liquefaction temperature becomes higher than that of H gas, and then H can be stored safely. Although this H added gas raises the total heat quantity, it needs to supply oxygen or air for the perfect combustion of it, and Ti, Ta, W metal or glassy C cannot melt and vaporize with burning of it, and the voltage of fuel cell with it becomes that with H gas.

b) Properties of Neutral Aqueous Electrolyte

・ Neutral aqueous electrolyte is obtained through electrolysis of water added very small amount of salt (NaCl) under vibratory agitation by vibration blades with a frequency of about 40 Hz.

・ This electrolyte has the mild and continuous sterilizing properties.

c) Phenomena of Generation of Various Elements under Vibratory Agitation

・ Light elements like magnesium (Mg) and heavy elements like zinc (Zn) are generated under vibratory agitation of pure water by palladium (Pd) plating vibration blades with a frequency of about 160 Hz.

・ Slightly heavy elements like phosphorus (P) are generated under vibratory agitation of aqueous magnesium chloride ($MgCl_2$) solution by vibration blades with a frequency of about 160 Hz.

・ Heavy elements such as nickel (Ni), copper (Cu), silver (Ag), platinum (Pt) and gold (Au) are generated under vibratory agitation of aqueous chloride solution such as calcium chloride or cesium chloride ($CaCl_2$ or CsCl) by vibration blades with a frequency of about 160 Hz. In regard to radioactive cesium (Cs), there is a possibility that the radioactively contaminated water, which is leaked from Fukushima Daiichi Nuclear Power Plant, is treated to reduce the radioactivity.

・ Some elements which have been analyzed by ICP (Inductively Coupled Plasma) atomic emission spectrometer are shown in Appendix-5.

References

United States Patent US 7,459,071 B2 (Dec. 2, 2008).

Japan Patent Kokai 2015-55527 (2015.03.23).

H. Oyama, Y. Ueno, K. Kitagawa and R. Ohmasa, Two-dimensional Visualization of Premixed Hydrogen-Oxygen High Temperature Flame, Proc. of IECEC2, (2004).

R. Ohmasa and A. Tanioka, Effect of Low Frequency Vibration on Water Electrolytsis, **56**, 207 (2005).

Appendix-2 Supposition of Generation Processes

OHMASA-GAS and the neutral aqueous electrolyte would be generated by stable cavitation, that is, the spherical bubbles with the nuclei of small water cage clusters which encapsulate hydrogen (H) atoms or bond oxygen (O) atoms or chlorine (Cl) atoms produced by the electrolysis, respectively. The generation of various elements under vibratory agitation related to the generation of OHMASA-GAS would be caused by transient cavitation, that is, when the spherical bubbles with nuclei of small water cage clusters which stay on the surface of vibration blade collapse, the small water cage cluster is pressed by water molecules which flow into the collapsing bubble to form the high density water cluster and collide on the surface of vibration blade.

Therefore, the following unified processes are supposed:

a) Generation of OHMASA-GAS

・ Water sheet clusters are formed on the pressurized surfaces of vibration blades under vibratory agitation of the aqueous electrolyte solutions like potassium hydroxide (KOH) with a frequency of about 40 Hz.

・ When the vibration blade moves in the opposite direction, large water tube clusters are made of the water sheet clusters which are partly peeled off by water stream under vibration agitation.

・ When the large water tube clusters separate from the depressurized surfaces of the vibration blades, they are divided into small decamer, pentadecamer or icosamer base water cage clusters of sizes ranging from about 0.5 to 1.0 nm.

・ Spherical bubbles with the nuclei of those water cage clusters are formed near the depressurized surfaces of the vibration blades.

・ The similar phenomena occur on another surface of the vibration blade in the opposite vibration phase.

・ The spherical bubbles flow to electrodes of electrolysis and finally some of them diffuse to disappear.

・ Through electrolysis of the aqueous electrolyte solution, H atoms are produced from cathodes and O atoms are produced from anodes.

・ The H and O atoms enter into the spherical bubbles with nuclei of water cage clusters when the spherical bubbles touch on cathodes or anodes, respectively.

・ The H atoms are encapsulated in the water cage cluster of the nucleus of spherical bubble, and O atom combines with H_2O molecule of the water cage cluster of nucleus of the other spherical bubble to form hydrogen peroxide (H_2O_2).

b) Generation of Neutral Aqueous Electrolyte

・ Spherical bubbles with nuclei of water cage clusters are formed near the depressurized surfaces of the vibration blades under vibratory agitation of very thin aqueous salt (NaCl) solution replaced to the aqueous electrolyte solutions like potassium hydroxide (KOH) in the case of above-mentioned “a) Generation of OHMASA-GAS” with a frequency of about 40 Hz, and flow to electrodes of electrolysis and finally some of them diffuse to disappear.

・ Through electrolysis of the aqueous salt (NaCl) solution Cl atoms are produced from anodes, which enter into the spherical bubbles with nuclei of water cage clusters when the spherical bubbles touch on the anodes.

・ The Cl atom combines with OH radical of the water cage cluster of nucleus of the spherical bubble to form hypochlorous acid (HClO).

c) Generation of Elements under Vibratory Agitation

・ Water sheet clusters are formed on the pressurized surfaces of normal or palladium plating vibration blades under vibratory agitation of the pure water or the aqueous electrolyte solutions like magnesium chloride ($MgCl_2$) with a frequency of about 160 Hz.
・ When the vibration blade moves in the opposite direction, large water tube clusters are made of the water sheet clusters which are partly peeled off by water stream under vibration agitation, some of which bond metal atoms like magnesium (Mg) .
・ When the large water tube clusters separate from the depressurized surfaces of the vibration blades, they are divided into small decamer, pentadecamer or icosamer base water cage clusters of sizes ranging from about 0.5 to 1.0 nm. Metal atoms like Mg bond to some of these water cage clusters.
・ Spherical bubbles with the nuclei of those water cage clusters are formed near the depressurized surfaces of the vibration blades.
・ When the vibration blade moves in the opposite direction again, some spherical bubbles collapse near the pressurized surface of the vibration blade. The impacts of collapsing bubbles propagate to the other spherical bubbles staying on the surface of the vibration blades and cause them to violently collapse.
・ The water cage cluster of the nucleus of collapsing spherical bubble on the surface of the vibration blades is pressed by water molecules which flow into the collapsing bubble to form the high density water cage cluster.
・ The high density water cage cluster, some of which include metal atoms like Mg, is pushed by water molecules which flow into the collapsing spherical bubble to collide on the surface of vibration blade.
・ The high density water cage cluster colliding on the surface of Pd plating vibration blade causes the reaction of generation of elements on or in it, in some cases metal atoms like Mg would relate to this reaction.
・ The similar phenomena occur on another surface of vibration blade in the opposite vibration phase.

References

C. E. Brennen, Cavitation and Bubble Dynamics (Cambridge University Press).

Appendix-3 Classification of Water Clusters

Water clusters were classified by composing shape of cross section or surface pattern before the structural optimization by MOPAC.

a) Water Tube Clusters

Several joined cross sections of pentamer and hexamer compose the decamer to over tricontamer water tube clusters, while a few joined cross sections of trimer and tetramer could compose them.

・$(H_2O)_{20}$[5x4] - $(H_2O)_{40}$[5x8] / $(H_2O)_{24}$[6x4] - $(H_2O)_{36}$[6x6]

b) Water Cage Clusters

A few joined cross sections of trimer, tetramer pentamer and hexamer were treated as the water cage clusters.

・$(H_2O)_6$[3x2], $(H_2O)_9$[3x3] / $(H_2O)_8$[4x2], $(H_2O)_{12}$[4x3]

・$(H_2O)_{10}$[5x2], $(H_2O)_{15}$[5x3] / $(H_2O)_{12}$[6x2], $(H_2O)_{18}$[6x3]

Four surface trimers compose the plane like tetramer of tetrahedron and eight surface trimers compose the hexamer of octahedron, and six surface tetramers compose the octamer of hexahedron of water cage cluster, respectively. Twelve surface pentamers compose the icosamer water cage cluster of regular dodecahedron, which can encapsulate one more H_2O molecule.

・$(H_2O)_4$[3*4], $(H_2O)_6$[3*8], $(H_2O)_8$[4*6], $(H_2O)_{20}$[5*12], $H_2O@(H_2O)_{20}$[5*12]

Three boat-shaped surface hexamers compose the octamer, and several chair-shaped surface hexamers compose over the icosamer water cage clusters.

・$(H_2O)_8$[6b*3] / $(H_2O)_{10}$[6c*4] - $(H_2O)_{22}$[6c*10]

Number of Cross Sections and Number of Multimer of Water Cage Clusters and Water Tube Clusters

	Water Cage Cluster		Water Tube Cluster								
Cross S. / Shape	2	3	4	5	6	7	8	9	10	11	⋯
Trimer	6	9	⋯								
Plane Tetramer	8	12	⋯								
Plane Pentamer	10	15	20	25	30	35	40	45	15	(50)	
Boat-shaped Hexamer	12	18	24	30	36	(42)	(48)				

( ) : Difficult to Calculate by Quantum ESPRESSO

Number of Faces and Number of Multimer of Water Cage Clusters

Shape \ Faces	2	3	4	5	6	7	8	9	10	11	12	⋯	22	⋯	22	⋯	32	⋯
Trimer			4				6					⋯						
Plane Tetramer					8				12			⋯						
Plane Pentamer											20・21		35		35		(50)	
Boat-shaped Hexamer		8																
Chair-shaped Hexamer			10		14		18		22		(26)							

( ) : Difficult to Calculate by Quantum ESPRESSO

Appendix-4 Examples of Structures of Water Clusters

Examples of the optimized structures of water clusters calculated by MOPAC are as follows.

・Water Tube Cluster

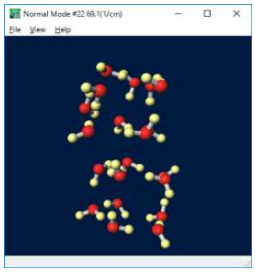

(H2O)20[5x4]

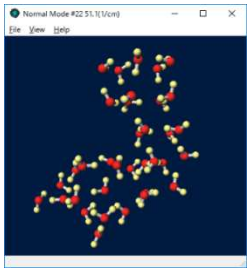

(H2O)35[5x7]

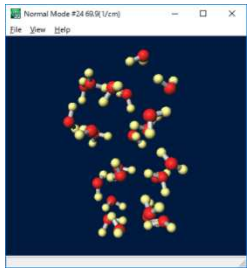

(H2O)24[6x4]

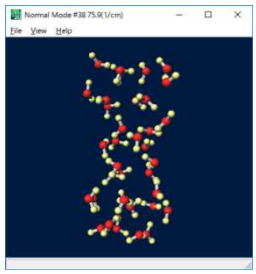

(H2O)36[6x6]

・Water Cage Cluster

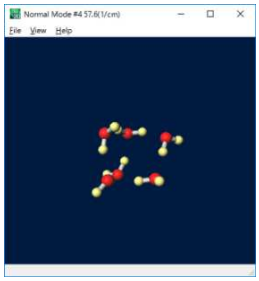

(H2O)6[3x2]

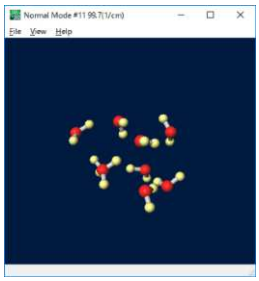

(H2O)9[3x3]

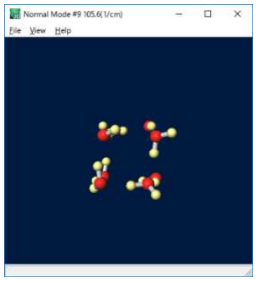

(H2O)8[4x2]

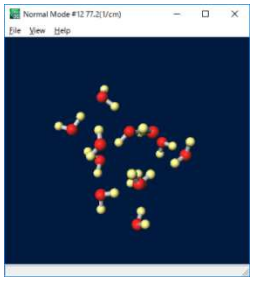

(H2O)12[4x3]

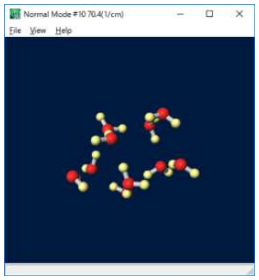

(H2O)10[5x2]

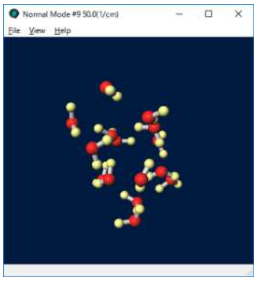

(H2O)15[5x3]

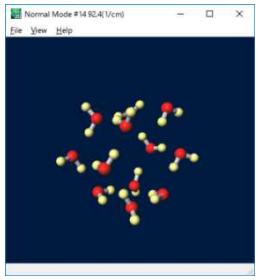

(H2O)12[6x2]

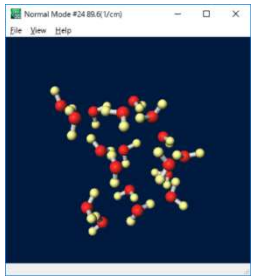

(H2O)18[6x3]

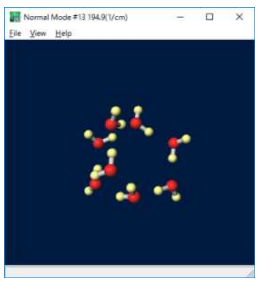
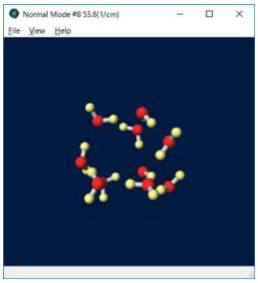
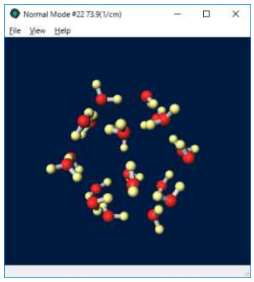
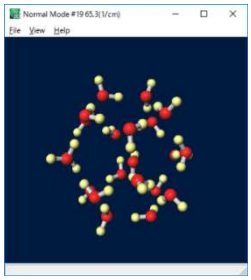

(H2O)8[6b*3] (H2O)10[6c*4] (H2O)20[5*12] H2O@ (H2O)21[5*12]

Appendix-5

Elements generated under vibratory agitation by palladium (Pd) plating vibration blades, which are analyzed by an ICP atomic emission spectrometer at Saitama Industrial Technology Center, are as follows.

Magnesium Chloride (MgCl2) Electrolyte											
Additive		Mg 12	Al 13	P 15	Ni 28	Cu 29	Zn 30	Ag 47	W 74	Pt 78	Au 79
		[mg/l]	[mg/l]	[mg/l]	[mg/l]	[mg/l]	[mg/l]	[mg/l]	[mg/l]	[mg/l]	[mg/l]
Tritiated Water	before processing	3900	< 0.1	< 0.1		< 0.1		< 0.1			< 0.1
	after 6 hour processing	2200	17	1900		150		130			0.23

Cupper Chloride (CuCl) Electrolyte											
Additive		Cu	Al 13	P 15	Ni 28	Cu 29	Zn 30	Ag 47	Ga	Co	Au
		[mg/l]	[mg/l]	[mg/l]	[mg/l]	[mg/l]	[mg/l]	[mg/l]	[mg/l]	[mg/l]	[mg/l]
Heavy Water	before processing	3100			0.3	—	< 0.1	< 0.1	< 0.1	< 0.1	< 0.1
	after 6 hour processing	2800			2.5	—	< 0.1	2.2	< 0.1	< 0.1	2.5
Tritiated Water	before processing	3100			0.3	—	< 0.1	< 0.1	< 0.1	< 0.1	< 0.1
	after 6 hour processing	2500			7.8	—	0.3	170	< 0.1	< 0.1	20

Cesium Chloride (CsCl) Electrolyte											
Additive		Cs	Al 13	P 15	Ni	Cu	Zn	Ag	W	Pt	Au
		[mg/l]	[mg/l]	[mg/l]	[mg/l]	[mg/l]	[mg/l]	[mg/l]	[mg/l]	[mg/l]	[mg/l]
Heavy Water	before processing	6400			< 0.1	< 0.1	< 0.1	< 0.1	< 0.1	< 0.1	< 0.1
	after 6 hour processing	5450			0.9	0.7	< 0.1	11	0.3	0.9	20
Tritiated Water	before processing	6400			< 0.1	< 0.1	< 0.1	< 0.1	< 0.1	< 0.1	< 0.1
	after 6 hour processing	5450			20	2.2	< 0.1	27	2.0	2.5	70